Abstract

Angularly-Resolved Elastic Light Scattering of Micro-Particles

Kevin B. Aptowicz

May 2005

From microbiology to astrophysics, the scientific community has long embraced elastic light scattering from small particles as a diagnostic tool. Elastic light scattering has an extremely large scattering cross-section, allowing for single particle interrogation. This is critical in applications where trace amounts of suspect particles are to be detected in a diverse background of natural aerosols. By angularly-resolving the elastically scattered light, features can be detected in these patterns that are sensitive to a particle's morphology (shape, size, internal structure, and composition).

An apparatus to collect LA TAOS (Large-Angle Two-dimensional Angular Optical Scattering) patterns from single particles *in-situ* and in real-time was designed and constructed. The setup utilizes a cross-beam trigger system to minimize the effects of the aberration coma stemming from the main collection optic, an ellipsoidal mirror. LA TAOS patterns of ambient aerosols were collected and analyzed. Approximately 15% of the ambient aerosol had a sphere-like shape. The refractive index of these spheres was estimated by curve-fitting to Lorenz-Mie theory. In addition, the island features prevalent in the LA TAOS pattern were analyzed. Metrics generated from these were used to get partial discrimination between clusters of *Bacillus subtilits* spores (a simulant for anthrax) and aerosol particles found in the ambient atmosphere. A novel experimental setup for collecting simultaneously LA TAOS patterns at two wavelengths in the mid-

infrared was also implemented. With this setup, the relative strength of single-particle absorption could be discerned at the two illuminating wavelengths.

Angularly-Resolved Elastic Light Scattering of Micro-Particles

A Prospectus
Presented to the Faculty of the Graduate School
of
Yale University
in Candidacy for the Degree of
Doctor of Philosophy

By
Kevin B. Aptowicz

Dissertation Director: Richard K. Chang

May 2005

To

Dr. Joel Simon

Physics Teacher
Central High School
Philadelphia, PA

Acknowledgements

I would like to thank the following people for their encouragement and support throughout my graduate career.

- My thesis advisor, Professor Richard Chang for his unending support and guidance. Working with Richard was a wonderful experience that I will always look fondly back upon.
- To the members of my thesis committee who helped shape this work: Professor Michel Devoret, Professor Robert Grober, Dean Paul Fleury, and Professor Christopher Sorensen.
- Dr. Ronald Pinnick and Dr. Steven C. Hill of the Army Research Laboratory for their mentorship and guidance both in and outside the lab. Judy Pinnick and Libby Hill for their hospitality that made week-long experiments taking place three hundred miles from New Haven feel like home.
- Dr. Yongle Pan, whose keen insight and endless energy greatly influenced this work.
- The countless other collaborators who I have learned a great deal from: Dr. Anish Goyal, Dr. Thomas Jeys, and Dr. Antonio Sanchez of the MIT Lincoln Laboratory; Dr. Richard Tober, Dr. Kris Gurton, and Dr. Gordon Videen of the Army Research Laboratory; Dr. Matt Hart and Dr. Jay Eversole of the Naval Research Laboratory; Dr. Jean-Claude Auger of the Comex Paint Company; Dr. Dahv Kliner of Sandia National Laboratory; Dr. Burt Bronk of the Airforce Research Laboratory.
- The other members of Professor Chang's group: Grace Chern, Mario Surbek, Hermes Huang, Dr. Veronique Boutou, Joseph Dudas, Jesse Mohn, Ajay Kishore, and Dr. Robert Wilson.
- The staff of Yale's School of Engineering and Applied Science: Patricia Brodka, Maria Gubitosi, Jayne Miller, Cara Gibilisco, and Dick Bascom for their administrative support, and Edward Jackson and Nicholas Bernardo for their advice and guidance.
- Colleagues from Yale's Physics and Applied Physics Departments: Chad Rigetti, Michael Metcalfe, Aric Sanders, Rona Ramos, Julie Wyatt, John Teufel, Dale Li, Celeste Yang, Aryesh Mukherjee, Dr. Ilona Kretzschmar, Dr. Sebastian Kaiser, Dr. Hakan Tureci, and Dr. Harold Schwefel.
- My family and friends who I'm excited to see again now that I have finished writing my thesis.
- Last but certainly not least, my wife Katie.

Table of Contents

List of Figures

List of Tables

Chapter 1: Introduction

Diagnostic tools to characterize small particles *in-situ* and in real-time are needed in a wide range of fields from microbiology to astrophysics. Most recently, following the anthrax scare of 2001, there has been a demand for a bio/chemical warfare alarm (analogous to a smoke alarm) that would constantly monitor heavily populated areas and give early warning of an attack.[1] Current early-warning systems are based on laser-induced fluorescence (LIF) in which an aerosol particle is excited in the ultraviolet (typically 266 nm or 355 nm) and the fluorescent spectrum of the aerosol is detected.[2] This technique is sensitive to the molecular composition of the aerosol (in particular the relative ratios of four primary fluorophors: tyrosine, tryptophan, NADH, and riboflavin).

In in-the-field equipment (*e.g.* the BAWS system), the LIF technique is primarily used as a biological particle counter. If the device senses a sudden increase in the number of biological particles, it triggers an alarm. However, such a system leads to numerous false alarms that undermine the utility of the device. In particular, diesel exhaust is a known interferent for the LIF technique. Because diesel exhaust is common both in urban areas, and on the battlefield, this may constitute a significant limitation of LIF based detection systems. As a result, the scientific community is currently seeking other early-warning techniques which may improve upon the LIF technique.

Designing an early-warning system presents two primary challenges. First, biological agents can come in a variety of forms such as bacteria, viruses, or nonliving toxins produced by microbes. These forms must be distinguished from the plethora of other airborne particles (dust, pollens, soot aggregates, paper and wood fibers, and animal

dander) that are benign. Thus the early-warning system needs to have a high level of specificity in order to be useful.

Second, even extremely dilute concentrations of biological agents can be deadly. The average healthy individual breathes in six liters of air a minute and each liter of air is composed of approximately 10^4 benign particles. Certain biological agents will lead to death if as few as ten organisms are inhaled.[3] Therefore, to prevent a person from becoming ill when passing through a contaminated area, a detector would need to pick out the existence of a few biological agents in a large background of benign particles. As a result, an effective early-warning system will need to have a high level of sensitivity.

Elastic light scattering from small particles has the potential to meet both of these requirements. As an initial matter, elastic light scattering has an extremely large scattering cross-section. This large scattering cross-section allows for single particle interrogation, which in turn allows for the detection of trace amounts of suspect particles. Elastic light scattering thus fulfills the need for system sensitivity that exists in designing an effective early-warning system.

Elastic light scattering also shows promise as having a high level of specificity to discriminate between different types of particles. As other authors have shown, elastic light scattering can be used in a variety of circumstances to detect the presence of particular substances.[4] By angularly-resolving scattered light from a single particle, features can be detected that are sensitive to a particle's morphology (shape, size, internal structure, composition, etc.).[5-7] These features may, hypothetically, allow a system to identify with particularity what particle is being interrogated.

In this work, I show that the island like features prominent in the patterns of angularly-resolved elastic light scattering can be used to partially discriminate between powder dispersed *Bacillus subtilis* spores (a simulant for anthrax) and the particles found in the ambient environment. However, my findings also show that the specificity with which *Bacillus subtilis* can be distinguished is not high enough to warrant a stand-alone system. The question remains whether elastic light scattering can be used as a complimentary technique to LIF to greatly reduce the rate of false-positives in existing biological agent detection systems. In particular, further inquiry is needed into the question of whether the interferents of elastic light scattering and LIF are different (in which case combining the techniques might allow one to greatly minimize the number of false positives).

In addition to considering the suitability of elastic light scattering as a means of detecting biological agents, this work also addresses elastic light scattering's suitability for detecting chemical agents. An approach to identifying chemical agents is to measure their absorption spectra in the mid-infrared. The profile of these spectra will depend upon the molecular vibrational modes of the aerosol particle, which leads to strong absorption bands in the mid-infrared wavelength range. Therefore, a particle's absorption spectrum could be used to discriminate between particles based upon their molecular composition. However, measuring the absorption of an aerosol even at a single wavelength is a difficult task. In particular, given the short path-lengths of a micron sized particle, the scattering cross-section can overwhelm the absorption cross-section of a particle. Thus, one can not simply measure the amount of light extinguished from an incident beam, even to get a rough estimate of the absorption of the particle.

However, embedded in the angularly-resolved elastic light scattering pattern is information about the particle's absorption at the incident wavelength. A novel experimental setup for collecting elastic scattering patterns simultaneously at two wavelengths was designed and implemented. By choosing the two incident wavelengths to be on and off an absorption band of a suspect particle, it was found that one can discriminate between aerosols based upon their absorption spectrum. This technique could be expanded to allow collection of single-particle absorption spectra over a multitude of wavelengths.

The utility of angularly-resolved elastic light scattering is investigated over the span of six chapters. In Chapter 2, the theoretical framework for the thesis is reviewed. First, the coordinate system utilized throughout the thesis is presented. Then the aerosol features that may effect the angular intensity distribution of elastically scattered light are discussed. The final two sections of Chapter 2 review Lorenz-Mie theory and the T-matrix method, techniques used to analyze the experimental data. Chapter 3 discusses the previous work that has been done in the field of elastic light scattering, emphasizing design breakthroughs, as well as the particle features that have been successfully extracted using elastic scattering from single particles.

The experimental apparatus and engineering concerns of the setup are presented in Chapter 4. Of particular note are subsections: 4.1.2, which discusses the LA TAOS (Large-Angle Two-dimensional Angular Optical Scattering) technique; 4.1.3, where the aberrations in the optical train are estimated; and Section 4.2, which presents the cross-beam trigger system, a critical development that greatly reduces aberration effects in the optical train. Finally in Chapter 5, the results of this work are presented. The first

section of Chapter 5 focuses on extracting absorption information from single aerosol particles. The experiments forming the basis for this section were performed at both visible and mid-infrared wavelengths. The second section analyzes LA TAOS patterns captured from both laboratory-generated and ambient particles. The analysis investigates the island features found in these patterns as well as the possibility of extracting the real part of the refractive index from spherical particles.

Chapter 2: Theoretical Background

The long list of methods and techniques to calculate light scattering from particles (Lorenz-Mie theory, T-matrix method, finite-element method, finite-difference time-domain method, point-matching method, Rayleigh approximation, Rayleigh-Gans approximation, geometrical optics approximation, discrete dipole approximation, to name a few) hints at difficulty of this calculation.[8] Therefore, Section 2.2 discusses the possible sources for light scattering and why scattering patterns, which hold so much information, are so difficult to interpret. In addition, Section 2.1 reviews the coordinate system used throughout this work. The final two sections review Lorenz-Mie theory and the T-matrix method, both of which are used to analyze the experimental data.

2.1 - Coordinate System for a Scattering Event

The spherical coordinate system used throughout this thesis is shown in Figure 2-1. The direction of any scattered ray can be defined by two angles, the polar angle θ and the azimuthal angle ϕ. The angle between the scattered ray and the z-axis is θ. Whereas the angle between the projection of the scattered ray onto the x-y plane and the x-axis is the angle ϕ.

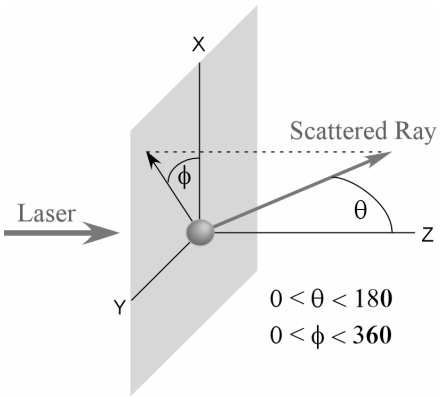

Figure 2-1: Spherical coordinate system for scattering event.

The data collected using this coordinate system is typically plotted as a polar plot as shown in Figure 2-2, where θ extends radially from the center and ϕ is plotted as the polar angle.[i] Note that the center of the plotted scattering data is almost always θ = 180° instead of θ = 0°, since the experimental arrangement collects the backward hemisphere of scattered light as shown later. In addition, the minimum value of θ detected will vary from 90°. For example, in the Section 5.2.3 and 5.2.4, the minimum angle detected is approximately 75°. The scattering pattern shown here was generated using Lorenz-Mie theory. The particle was a 5 μm diameter sphere with refractive index 1.334 illuminated by an incident beam wavelength of 532 nm.

[i] Note the possible confusion here of calling ϕ the polar angle. This is only true in terms of plotting the data. For the scattering event, ϕ is the azimuthal angle and θ is the polar angle. To avoid confusion ϕ will only be regarded as the azimuthal angle for the rest of this Thesis.

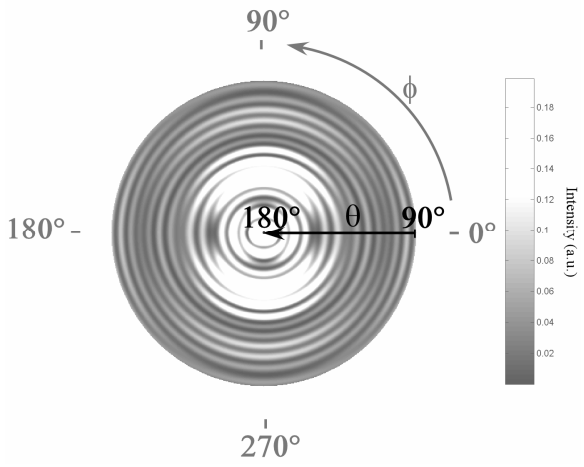

Figure 2-2: Example polar plot of scattering data.

2.2 - Sources of Light Scattering

At the molecular level, light scattering from a particle can be thought of as the excitation and emission of a collection of dipoles (this is the basis for the discrete dipole approximation). A remarkable result is that when an infinite lattice of closely spaced (relative to the wavelength of the incident beam) dipoles are illuminated by a plane wave, only light scattered directly forward will add constructively, as predicted by the Ewald-Oseen extinction theorem.[9] Therefore, to have a nonzero contribution of light at any other angle requires the medium to be optically inhomogeneous. Thus the sources of scattering from particle are found wherever there are fluctuations in the refractive index that are comparable with the wavelength (λ) of light.

Figure 2-3 examines an aggregate particle at different magnification levels to depict what particle characteristics will play a role in the scattering pattern. At the lowest magnification, the particle's shape and size (with respect to λ) are obvious factors. As the magnification is increased, the geometry of the cluster or perhaps more to the point, the fractal dimension of the aggregate effects the scattering pattern.[10] The next prominent

features are the primary particle's size and structure, which includes it shape as will as internal features (e.g. inclusions). Finally, the value of the refractive index, relative to the medium (air), will effect the scattering pattern.

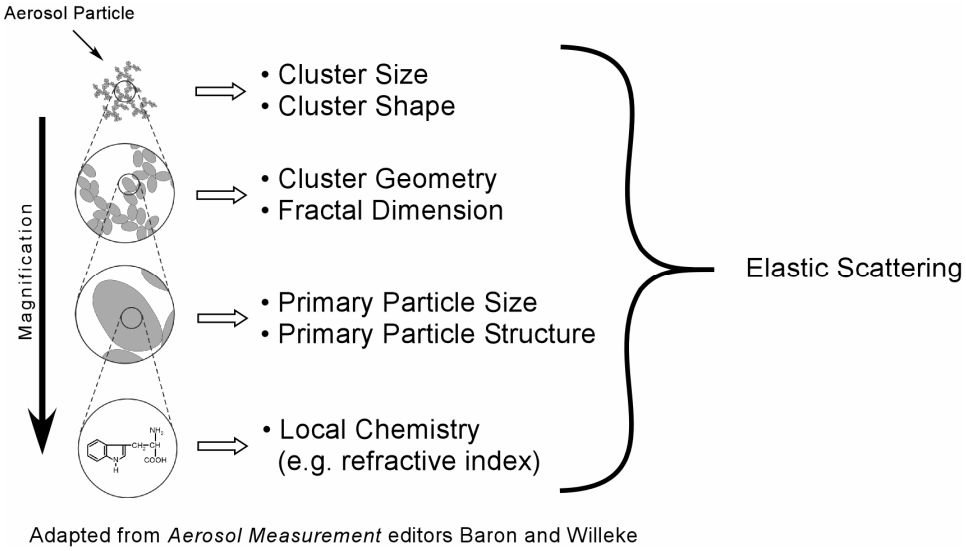

Adapted from *Aerosol Measurement* editors Baron and Willeke

Figure 2-3: Particle features at different magnifications that effect light scattering.

Thus the scattering patterns are information rich, but extremely entangled. It is a difficult task to extract one piece of information without knowing the contribution due to the other features. To see this at a more physical level, the light scattering from a two-sphere aggregate will briefly be investigated at different levels of approximation.

Assuming that you know the scattering matrix for the primary particle, the effect of adding additional primary particles, to first order, will just be an additional interference pattern in the far-field that will modulate the single particle interference pattern. This is depicted in Figure 2-4 for the case of two spheres. In Figure 2-4(a) the orientation of the two spheres is depicted and in Figure 2-4(b) the scattering pattern for a single sphere is shown; see Figure 2-2 for the coordinate system. The plot in Figure

2-4(c) is calculated from the interference of two point sources each located at the center of the two spheres. Finally the image shown in Figure 2-4(d) is the scattering pattern in (b) modulated by the interference pattern in (c). Experiments have shown that this approximation is fairly accurate for the case given.[11] Note that the single particle scattering pattern is still identifiable, although it is now masked beneath the multiple particle interference pattern.

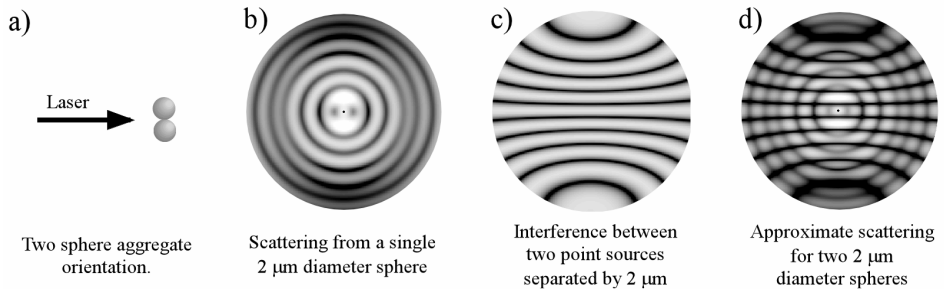

Figure 2-4: Approximate scattering profile for a two-sphere aggregate particle.

Mathematically, this approximation can be depicted by first just considering a single particle where the irradiance in the far-field (I_s) is

$$I_s = \left|E_s(\theta,\phi)\right|^2 \tag{2-1}$$

then if we have N particles, the irradiance in the far-field (I_N) is

$$I_N = \sum_{k=1}^{N} \left|E_k(\theta,\phi)\right|^2 . \tag{2-2}$$

For the far field, the scattering profile from each individual scatterer is the same, accept for an overall phase factor (δ) due to differences in the particle positions. Therefore,

$$I_N = \sum_{k=1}^{N} \left|E_k(\theta,\phi)\right|^2$$

$$= \sum_{k=1}^{N} \left| E_s(\theta,\phi) \times \exp(i\,\delta_k(\theta,\phi)) \right|^2$$

$$= \left| E_s(\theta,\phi) \right|^2 \times \sum_{k=1}^{N} \left| \exp(i\,\delta_k(\theta,\phi)) \right|^2$$

$$= I_S \times \sum_{k=1}^{N} \left| \exp(i\,\delta_k(\theta,\phi)) \right|^2 . \qquad (2\text{-}3)$$

Therefore the total scattering intensity I_N is the product of two parts: (1) the scattering intensity of a primary particle, I_S, and (2) the interference term where each primary particle is treated as a point source.

To improve upon this approximation, the effects of shadowing[i] and multiple-scattering[ii] have to be incorporated into the solution. Assuming the scattering matrix for each primary particle is known, the T-matrix method is able to compute scattering matrix for the aggregate if the particles are not in direct contact.[12] This is rarely true in practice, however, Holler *et al.* have shown that for the case of a cluster of 13 closely packed spheres, the theory appears to support experimental findings even if this stipulation is ignored.[13] The possible error in taking this approach stems from the interaction phenomena that occur if particles are in contact, which will change the scattering matrix for a single particle.

For complex aggregate structures such as a cluster of biological spores, the direct problem of calculating the scattering matrix becomes increasing difficult to the point that no exact solution exists even if the particle is well characterized. Therefore, the inverse

[i] The incident beam can be partially blocked by another particle in the foreground before it illuminates the particle of interest.
[ii] Light scattered from one particle can then act as an incident beam for scattering off of other particles.

problem of fully characterizing a particle based upon the angularly-resolved elastically scattered light is equally, if not more, difficult. In the next two sections, cases where one can calculate the exact solution are presented.

2.3 - Exact Solution for Light Scattered by a Sphere

Using Maxwell's equations and the appropriate boundary conditions, the scattering of a monochromatic plane-wave incident on a homogenous, isotropic sphere of radius *a* can be solved exactly. This solution is commonly referred to as Lorenz-Mie theory, although who precisely is the author of this theory is disputed.[6] Since this present work heavily relies upon Lorenz-Mie theory to support experimental findings as well as the basis function for a curve-fitting routine, a brief summary of the theory is in order. This outline of the theory follows the analysis in the Bohren and Huffman text.[5]

From Maxwell's equations, a time-harmonic electromagnetic field $(\vec{E}, \vec{H})$ in a linear, isotropic, homogenous medium must satisfy the vector wave equation

$$\nabla^2 \vec{E} + k^2 \vec{E} = 0,$$

$$\nabla^2 \vec{H} + k^2 \vec{H} = 0 \tag{2-4}$$

where k is the wave vector and both $\vec{E}$ and $\vec{H}$ are divergence-free. If we now define a scalar function Ψ that is a solution to the scalar wave equation, we can construct two vector functions $(\vec{M}, \vec{N})$ by taking appropriate vector derivatives of the scalar function Ψ that both satisfy the vector wave equation as well as Maxwell's equations. This greatly simplifies the problem where only the scalar wave equation,

$$\nabla^2 \psi + k^2 \psi = 0, \tag{2-5}$$

has to be solved with the given boundary conditions.

Spherical polar coordinates (r,θ,ϕ) can be used to generate a set of complete solutions that match the symmetry of the boundary conditions. A separation of variables leads to even and odd solutions:

$$\psi_{even,m,n} = \cos m\phi \, P_n^m(\cos\theta) z_n(kr),$$

$$\psi_{odd,m,n} = \sin m\phi \, P_n^m(\cos\theta) z_n(kr) \tag{2-6}$$

where $P_n^m(\cos\theta)$ is the associated Legendre functions of the first kind and z_n is any of the three spherical Bessel functions (1st, 2nd, and 3rd kind). These scalar functions are known as the (scalar) spherical harmonics and thus the vector functions generated by them are the vector spherical harmonics, $(\vec{M},\vec{N})$, which are generated by

$$\vec{M}_{even,m,n} = \vec{\nabla}\times(\vec{r}\psi_{even,m,n}),\ \vec{M}_{odd,m,n} = \vec{\nabla}\times(\vec{r}\psi_{odd,m,n}),$$

$$\vec{N}_{even,m,n} = \frac{\vec{\nabla}\times\vec{M}_{even,m,n}}{k}, \text{ and } \vec{N}_{odd,m,n} = \frac{\vec{\nabla}\times\vec{M}_{odd,m,n}}{k}. \tag{2-7}$$

The incident x-polarized plane wave can be expand in vector spherical harmonics to take the form

$$\vec{E}_i = E_0 \sum_{n=1}^{\infty} i^n \frac{2n+1}{n(n+1)} (\vec{M}^{(1)}_{odd,1,n} - i\vec{N}^{(1)}_{even,1,n}),$$

$$\vec{H}_i = \frac{-k}{\omega\mu} E_0 \sum_{n=1}^{\infty} i^n \frac{2n+1}{n(n+1)} (\vec{M}^{(1)}_{odd,1,n} + i\vec{N}^{(1)}_{even,1,n}), \tag{2-8}$$

where the superscript (1) is appended to vector spherical harmonics for which the radial dependence of the generating function is specified by spherical Bessel functions of the

first kind, ω is the frequency of the monochromatic incident wave, and μ is the permeability.

We may also expand the scattered electromagnetic fields $(\vec{E}_s, \vec{H}_s)$ and the field inside the sphere $(\vec{E}_l, \vec{H}_l)$ in vector spherical harmonics. Of course, the fields must satisfy the boundary condition between the sphere and the surrounding medium:

$$(\vec{E}_i + \vec{E}_s - \vec{E}_l) \times \hat{e}_r = (\vec{H}_i + \vec{H}_s + \vec{H}_l) \times \hat{e}_r = 0. \tag{2-9}$$

This in conjugation with both the orthogonality of the vector harmonics and the form of the expansion of the incident field dictate that the coefficients in the expansions vanish for all m≠1 for the scattered field and the field inside the sphere. Using the physical knowledge that the scattered wave must be an outgoing wave, the expansion of the scattered field is

$$\vec{E}_s = \sum_{n=1}^{\infty} E_n (i a_n \vec{N}^{(3)}_{even,1,n} - b_n \vec{M}^{(3)}_{odd,1,n}),$$

$$\vec{H}_s = \frac{k}{\omega\mu} \sum_{n=1}^{\infty} E_n (i b_n \vec{N}^{(3)}_{odd,1,n} + a_n \vec{M}^{(3)}_{even,1,n}), \tag{2-10}$$

where the superscript (3) now stands for the vector spherical harmonics where radial dependence of the generating function is specified by spherical Bessel functions of the third kind, Hankel functions. Using a similar approach for the field inside the sphere and taking into account the finiteness at the origin, which requires us to use the spherical Bessel function of the first kind, we arrive at an analogous solution with the coefficients (c_n, d_n).

If we apply these equations to the boundary conditions Eq. (2.10) after some algebraic manipulation, we arrive at a set of four linear equations in the expansion coefficients. Solving this set of linear equations and making use of the Riccati-Bessel functions

$$\Psi(\rho) = \rho\, j_n(\rho) \qquad \xi(\rho) = \rho\, h_n^{(1)}(\rho), \tag{2-11}$$

where ρ = kr, we find that the scattering coefficients may be written as

$$a_n = \frac{m\Psi_n(mx)\,\Psi_n'(x) - \Psi_n(x)\,\Psi_n'(mx)}{m\Psi_n(mx)\,\xi_n'(x) - \xi_n(x)\Psi_n'(mx)},$$

$$b_n = \frac{\Psi_n(mx)\,\Psi_n'(x) - m\Psi_n(x)\,\Psi_n'(mx)}{\Psi_n(mx)\,\xi_n'(x) - m\xi_n(x)\Psi_n'(mx)} \tag{2-12}$$

where $x = \frac{2\pi r n_0}{\lambda}$ is the size parameter, r is the radius, λ is the wavelength, and $m = \frac{n_1}{n_0}$ is the relative refractive index. The code used to calculate these coefficients and compute the angular intensity of the scattered light is from the text *Light Scattering by Particles: Computational Methods* by P.W. Barber and S.C. Hill.[14]

2.4 - Exact Solution for Light Scattered by a Nonspherical Particles

Unfortunately, the separation of variables technique that was successfully applied to the scattering of spheres may only be extended to a few additional simple cases, such as a radially inhomogeneous sphere,[15] an infinite elliptical cylinder,[16] and core-mantle spheroids.[17,18,19] Exact solutions from a larger field of nonspherical particles have been calculated using the T-matrix method, initially introduced by Waterman.[20,21] We utilize

the T-matrix method to calculate the scattering pattern from a pill-shaped particle, which approximates the shape of a BG spore.

The T-matrix technique is based upon Huygens principle as well as the linearity of the Maxwell equations and the constitutive relations. If the scattered wave and the incident wave are expanded in spherical wave harmonics, where the coefficients of the latter are a_n and b_n (see 2-12) and the coefficients of the former are labeled c_n and d_n, then a transition matrix relates them

$$\begin{bmatrix} \bar{\mathbf{c}} \\ \bar{\mathbf{d}} \end{bmatrix} = \bar{\bar{\mathbf{T}}} \begin{bmatrix} \bar{\mathbf{a}} \\ \bar{\mathbf{b}} \end{bmatrix} \tag{2-13}$$

from linearity considerations. However, the derivation of (2.13) requires the external field to lie outside of a circumscribing sphere. This limitation is of little importance for single scatterers but is of great concern when calculating the scattering matrix for aggregates, particularly when the wavelength of the incident beam is on the order of or less than the primary particle's dimensions. Thus to calculate the scattering matrix for a cluster of oblong primary particles, the circumscribing sphere for each particle must not overlap thereby requiring the cluster structure to have large gaps (on the order of the particles themselves) of air between some of the particles. In addition, Eq. (2-13) is of little use without knowing the T-matrix. The extended boundary condition method (ECBM) is the usual path to obtain the desired matrix. The formulas that come out of the EBCM calculation are greatly simplified if the particle is rotationally symmetric and thus a majority of the numerical results computed with EBCM pertain to bodies of revolution.[12] The calculations in this Thesis using the T-matrix method were performed by Dr. Jean-Claude Auger.

Chapter 3: Experimental Background

In the first section, the past and present apparatuses used to detect multi-angle elastic light scattering from single particles are briefly reviewed. The emphasis is on when a major improvement in instrument design occurred, rather than a complete survey of all the different variations of instruments that were published. This is followed up with a short discussion of what parameters have been successfully extracted (e.g. shape, refractive index) using these devices.

3.1 - Review of Light Scattering Instrumentation

In the late 1940s and early 1950s, Frank T. Gucker led the development of optical particle sizers.[22,23] In this device, a fine stream of aerosol particles traverse an intense beam of light. After a photomultiplier tube detects the flashes of light due to scattering, the resulting electrical pulses are sorted based upon the pulse height, which loosely correlates to particle size.

Realizing that there was more information in resolving the scattered light over different angles, in 1961 Gucker designed and constructed a device to detect multi-angle light scattering which utilizes electro-dynamic levitation and a single photo multiplier tube (PMT) on a motor-driven rotation stage.[24,25] With an angular resolution of 5.2°, light scattered in a fixed scattering plane over an polar angle (θ) range from 40° to 110°. A little under ten years later, Phillip J. Wyatt led a design team that constructed an instrument (the *Differential II)* which had the same basic design, but improved the components (*e.g.* a laser source and solid state electronics) and detected the scattered light over a larger angle range from 10° to 170° with a 2° angular resolution.[26] This

device could extract information about the particle's morphology with some success mainly limited to the optical properties of homogenous spheres or coated spheres (*e.g.* certain bacterial spores).[27]

Recognizing the limited utility for instruments based upon electro-dynamic levitation due to extremely low thru-put capabilities, Gucker set out to develop another instrument, one that could detect angularly-resolved scattering light from aerosols in a laminar flow. The result was an extremely clever design.[28] The key element is a narrow strip of mirror in the form of a prolate ellipsoid as shown in Figure 3-1. The light beam, which enters and exits through holes in the mirror, is scattered by an aerosol in flow at the focal point of the mirror. The light scattered in the plane of the mirror is reflected by the mirror as a circle of light converging to the second focal point of the ellipsoid where the photomultiplier tube is positioned. This converging circle of scattered light is intercepted by a rapidly rotating disc fitted with an aperture so that the photomultiplier tube records a time varying signal which corresponds to a ~360° sweep of the scattering pattern for each cycle of the spinning disc. This set-up was improved upon by Bartholdi *et al.* by intercepting the circle of light with a circular photodiode array made up of 32 elements allowing for higher data collection rates.[29]

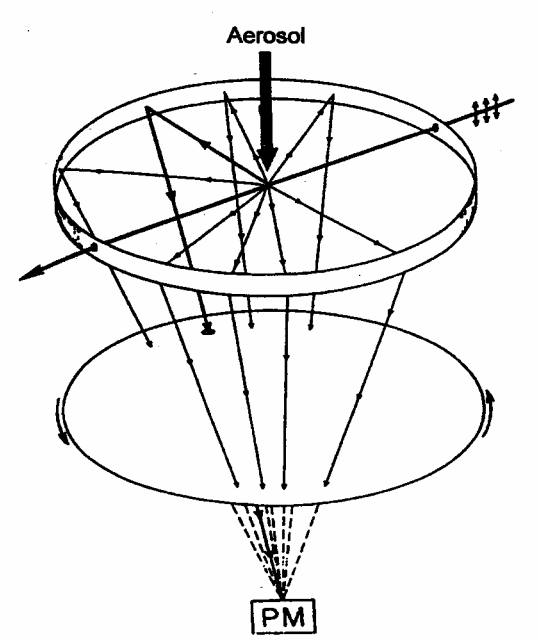

Figure 3-1: Ellipsoidal mirror used by Gucker *et al.* to detect almost 180° of scattered light at two fixed azimuthal angles on a single photo multiplier (PM) tube.

The DAWN-A developed by Wyatt *et al*. in the late eighties could detect angularly-resolved light elastically scattered from particles in a flowing gas stream over different azimuthal angles (ϕ) as well as different polar angles (θ).[30] The geometry of the set-up is quite simple. Fiber bundles coupled to photodiodes are placed at sixteen scattering angles over the surface of a spherical chamber. The peak current from each PMT is then recorded every time a particle flows through the laser beam at the focal volume.

In the early nineties, Kaye *et al.* designed a system that utilized an ellipsoidal mirror similar to Gucker's design, although the laser was now directed down the major axis of the ellipsoid. In this design, light originating from a scattering event at the first focal point of the ellipsoid, reflects off the ellipsoidal mirror and propagates through an iris located at the second focal point. After the iris, a collimating lens directs the light

onto an ICCD detector, thus the light falling on the detector is a two-dimensional transform of the three-dimensional spatial intensity distribution falling onto the ellipsoidal reflector.[11] This design collected scattered light over the polar angular range 30° to 141° and azimuthal angle range 0° to 360° with a 385x288 pixel detector. However, a major limitation of this design is the aberrations associated with collecting such a large numerical aperture which prevented the collected light scattering patterns from being quantitatively compared with theory. The design was then simplified by Kaye *et al.* so that only the forward scattering pattern was detected within a cone of ~30° by using a high f-number lens so that these misalignment effects could be lessened. In addition, the ICCD detector was replaced by a photodiode array chip, similar to the Bartholdi *et al.* design.[i,31]

3.2 - Review of Extracted Particle Features

Solving the inverse scattering problem of backing out a particle's morphology given the angularly-scattering pattern is an extremely difficult problem except for the simplest case: the non-absorbing homogenous isotropic sphere. For this case, matching theory (Lorenz-Mie theory) to experimental findings requires only two parameters to be varied: the refractive index and the radius, whereas for non-spherical particles the particle's orientation also needs to be searched over.

Looking through the literature for scattering by a sphere, there have been some remarkable experimental results. Using a electro-dynamically levitator and a tunable laser, and utilizing the rich optical resonance spectra implicit in Lorenz-Mie theory

[i] It should be noted that the utilization of a lens as a collection optic for single particle light scattering to angularly resolve both polar and azimuthal angles has a long history. For example, see the work done by A. Ashkin and J.M. Dziedzic in the late seventies and early eighties.

solutions, the radius and the refractive index of small spheres (~1 um) have been backed out with relative errors of 5×10^{-5}.[32,33] However, for laminar flow systems, such accuracies have not been realized. The "flow-through" system designed by Gucker (see Figure 3-1) was capable of measuring the refractive index to within 0.7% and the radius to within 0.5%.[34] If the laser's wavelength is close to resonance, the accuracies could be greatly approved upon. In addition to homogenous spheres, experiments have been performed to back out the refractive index from coated spheres with less success.[27,35]

For non-spherical particles, although exact comparison with theory is difficult, general features can be used to discriminate between different particle shapes. For example, Kaye et al. set out to design an APC (Airborne Particle Classifier) that could identify basic particle shapes in an attempt to detect harmful asbestos and mineral fibers.[36,4] If a fiber is illuminated along the broad-side, then the scattering is similar to the diffraction from a single slit. Detecting the light scattering pattern over the full range of azimuthal angles (ϕ = 0°-360°) from a fiber, two intensity peaks should stand out that will be in the scattering plane normal to the major axis of the fiber. Using a set-up described in the previous section in series with a trained neural network, Kaye *et al.* are able to process 10^3 particles a second within a sample volume of 1 L/min with fairly high discrimination ability between fiber and other aerosols. The DAWN-A (Wyatt Technology Corp.) was used in a study to determine the fraction of spherical particles in the ambient aerosols.[37,38] Sampling ambient particles in the 0.2 – 0.8 μm size range, it was determined that <10% of the particles were non-spherical.

In addition to probing the overall shape of the particle, efforts have also been made to extract information about particle internal structure. Holler *et al.* used a camera

lens to collect Two-Dimensional Angular Optical Scattering (TAOS) patterns from clusters of *Bacillus subtilus* var *niger* (BG) spores and found that island structures were observable in the spatial scattering patterns and that the number of islands increased per unit solid angle with an increase in cluster diameter.[39] The work performed for this thesis, to some extent, follows from Holler's results.

Chapter 4: Instrumentation

Several different experimental configurations were used to detect elastic scattering patterns. Each setup could be reduced to four primary subsystems: (1) the light collection scheme to guide the scattered rays onto the detector; (2) a trigger system to determine when a particle was in the scattering volume; (3) aerosol sampling or generation equipment; and (4) a laser source as well as a detector with appropriate wavelength responsitivity. Each subsystem is discussed separately here whereas the results of combining the subsystems are reserved for the next chapter. The first two subsystems go to the heart of the experiments and thus particular attention is paid to them.

4.1 - Light Collection Schemes

The first light collection scheme utilizes a lens in the Abbé sine condition to collect the elastically scattered light. Holler *et al.* called this technique TAOS (Two-dimensional Angular Optical Scattering) to distinguish it from the multitude of instruments that collected either light scattering at a single angle or over a range of polar angles (θ) for a fixed azimuthal angle (ϕ). The second technique is similar in design to the instrument of Kaye *et al.* where an ellipsoidal mirror is used to collect light over a far larger solid angle (greater than 2π steradians) than TAOS. The advantages and disadvantage of each approach are discussed.

4.1.1 - Two-dimensional Angular Optical Scattering (TAOS)

Figure 4-1(a) shows the coordinate system used through-out this work (see also Section 2.1). A simple diagram of the TAOS set-up is shown in Figure 4-1(b), where the

lens is placed a focal length away from the illuminated aerosol particle as prescribed by the Abbé sine condition.[9] The rays scattering off of the particle enter the lens at an angle γ with respect to the optic axis of the lens and emerge parallel with a displacement h given by

$$h = f \sin\gamma \tag{4-1}$$

where f is the focal length of the lens. A detector is placed at the back focal plane of the lens so that it is detecting the far-field image of the scattered light.[40] With the ability to buy off-the-shelf camera lenses that are well corrected for aberrations and have a adequate depth of field, the detected TAOS pattern can be unwrapped so that each pixel is correlated to an exact scattering angle (θ,ϕ). However, this system collects a limited solid angle of the scattered light. For example, given a very fast f/1 lens, the collected solid angle is

$$\int_0^{360°}\int_0^{26.5°} \sin(\theta)d\theta d\phi = 0.66 \text{ steradians.} \tag{4-2}$$

Thus only $\frac{0.66}{4\pi} = 5.2\%$ of the total solid angle is collected.

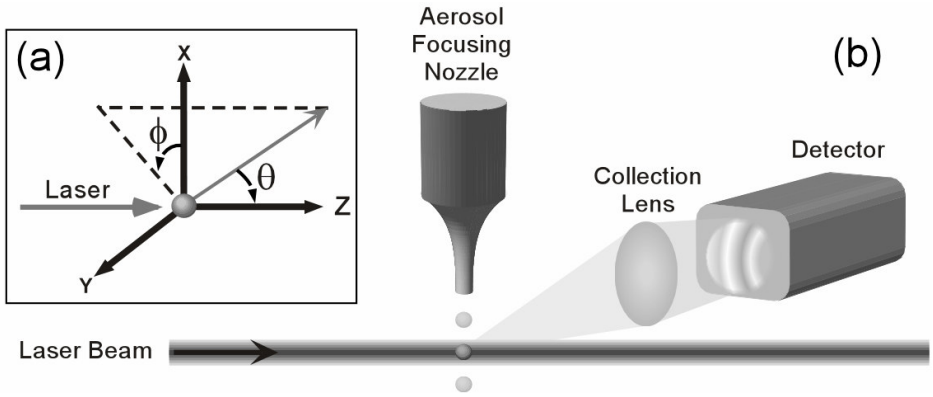

Figure 4-1: (a) Spherical polar coordinates system used to define the direction of a scattered ray. (b) Experimental setup utilized for TAOS measurements.

4.1.2 - Large-Angle Two-dimensional Angular Optical Scattering (LA TAOS)

The key element in the LA TAOS technique is the prolate ellipsoidal mirror (Opti-Forms Inc., Model E64-3) that collects over 2π steradians of scattered light, almost a factor of ten improvement over TAOS. However, the trade-off for this large collection angle is that the system has an extremely small depth of field. It is well known that ellipsoidal reflectors are aberration-free when imaging between the two focal points. However for off-axis imaging the reflector suffers severely from coma, which is a variation of magnification with aperture. This will distort the LA TAOS image leading to a mislabeling of the scattering angle (θ,ϕ) associated with each pixel. A further discussion of this topic in more detail occurs later in the chapter (Subsection 4.1.2.1).

A simple diagram of the LA TAOS setup is shown in Figure 4-2. Ideally, the scattering event occurs at the first focal point of the ellipsoid. The scattered rays that reflect off of the ellipsoidal mirror are focused through an iris that is located at the second focal point. The rays from this 'virtual' particle located at the iris are then detected by an ICCD or CCD. The mapping of these scattered rays from the three-dimensional space of

the scattering volume to the two-dimensional detector plane is nonlinear. However, taking into account the geometry of the system, every pixel of the detector can be matched with a unique scattering angle (θ and ϕ). Note the direction of the laser beam can be reversed by replacing the beam block with a right angle prism or small steering mirror and placing the laser source off to the side of the setup. Then, the forward hemisphere of scattered light can be collected as is shown in a later chapter, see Figure 5-8.

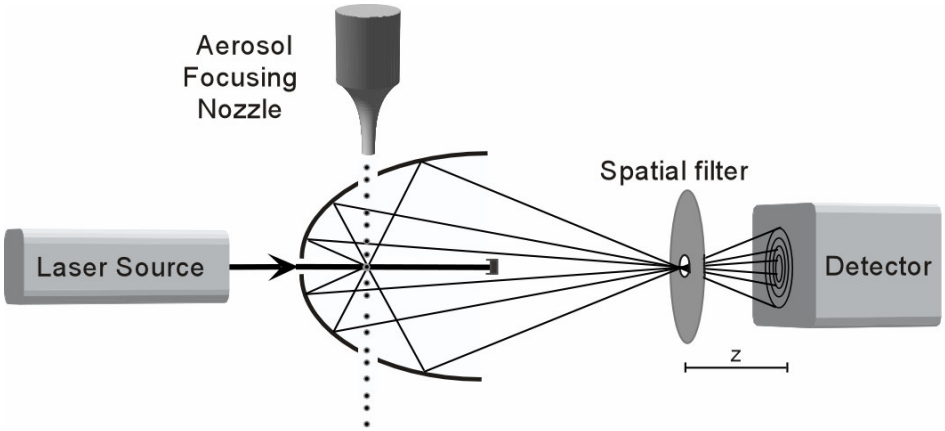

Figure 4-2: Experimental setup utilized for LA TAOS measurements.

Unlike the TAOS setup, in the LA TAOS design there is no lens used to detect the far-field intensity pattern. Rather, by placing the detector at a sufficient distance behind the spatial filter (a distance *z*), the Fraunhofer approximation can be invoked and the detector is considered to be in the far-field. The Fraunhofer approximation is

$$z > \frac{k * D^2}{2}, \tag{4-3}$$

where k is the wavevector and D is the particle's diameter.[40] If the particle's diameter is 10 microns (diameter = 10^{-3} mm) and it is illuminated from a frequency doubled Nd:YAG (k = 11810 mm^{-1}) the detector needs to be greater than 0.6 mm behind the

spatial filter, which is satisfied for the LA TAOS experiments. Figure 4-3 shows a picture of the ellipsoidal mirror used in the setup and is accompanied by an illustration noting the dimensions of the mirror.

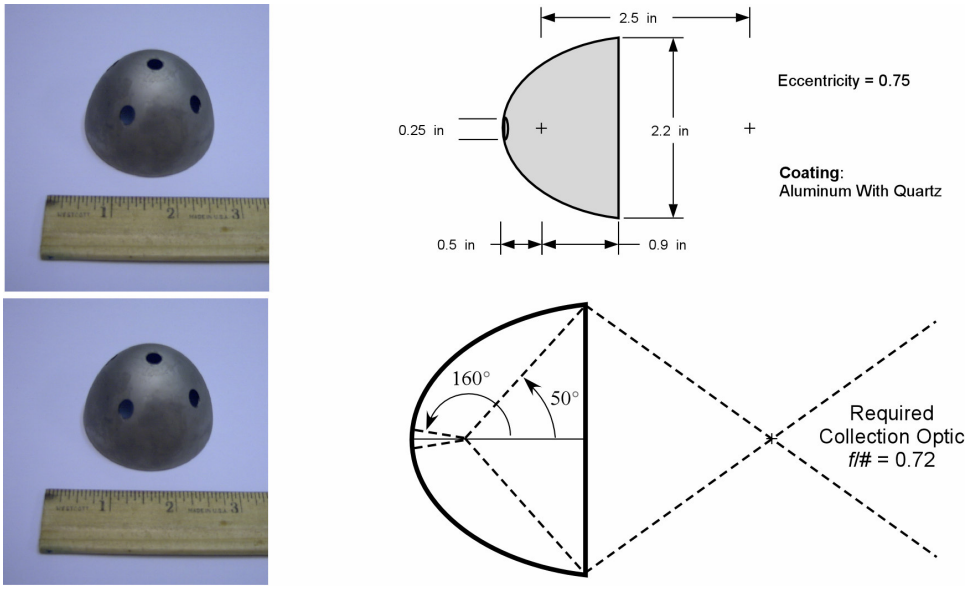

Figure 4-3: Ellipsoidal mirror used to capture the LA TAOS patterns.

This design is not new to the field of aerosol studies. Indeed, in the early seventies, Frank Gucker designed an extremely clever instrument around an ellipsoidal mirror (see Section 3.1). Paul Kaye and Edwin Hirst had a setup very similar to the one shown in Figure 4-2.[41] However, the work performed for this Thesis has a couple of key improvements. A cross-beam trigger system (to be discussed in the next section) was utilized to minimize the aberration due to the ellipsoidal reflector. This drastically reduced the error in properly labeling each pixel with a scattering angle, θ and ϕ. In addition, the cross-beam trigger system triggered a high-power pulsed laser source, rather than using a CW source as has been previously done. This greatly increased the number of photons detected as well as minimized the rotation and translation of the particle during the scattering event giving a crisper image.

4.1.3 - Aberrations in Ellipsoidal Reflectors

As will be discussed in the next chapter, the limiting element for most of the data analysis was the ellipsoidal reflector. Particles that were not perfectly centered to within a couple of microns of the focal point lead to visibly distorted images. In addition, the fabricated ellipsoidal mirror may deviate from the geometric shape. This can either be a gross deviation leading to a distorted image or a slight fluctuation around the ideal shape, which would blur the image. Any distortion in the image will lead to a mislabeling of the scattering angle (θ, ϕ) associated with each pixel. In what follows, these distortions are quantified by allowing the sources of error mentioned above to propagate through the system.

In this analysis, we consider three possible sources of error, as shown in Figure 4-4. First, the particle could be slightly misaligned along the mirror's major axis. This longitudinal error is labeled Δ_{lon} and has units of microns. Second, the particle could be slightly misaligned normal to the mirror's major axis. This lateral error is labeled Δ_{lat} and also will have units of microns. Finally, the mirror surface could be distorted from the ideal geometric shape leading to angular deviation of the reflected ray from the ideal path. The angular deviation of surface slope of the mirror is labeled Δ_{dev}, which has units of arc minutes. This will result in a deviation of $2\Delta_{dev}$ in the reflected scattered ray.

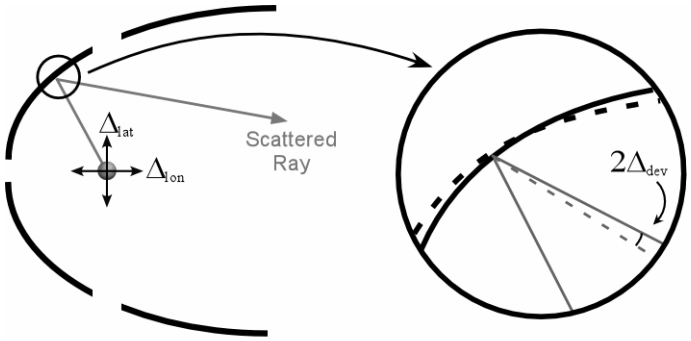

Figure 4-4: Depiction of experimental errors leading to a distorted LA TAOS pattern. Dotted line represents ideal geometric shape of the mirror.

The overall translation associated with Δ_{lon} and Δ_{lat} is less important than their effect on the reflected angle. To a first approximation, this effect is proportional to the curvature of the ellipsoid. A section of the ellipsoid that has a higher degree of curvature would lead to a greater deviation in the angle of the reflected rays if the particle is slightly shifted. Therefore, all three errors (Δ_{lon}, Δ_{lat}, and Δ_{dev}) lead to an angular deviation with respect to the ray's ideal path after specular reflection occurs at the mirror's surface. This is compounded by the distance the ray travels before it reaches the detector plane. The longer the distance to the detector plane, the farther the ray will propagate off course due to these angular deviations.

The effects of these aberrations on labeling the scattering angles can be estimated by analyzing the geometry of the setup. The cross-beam triggering system, discussed in the next section, will only trigger the laser source if particles are within 12.5 microns of the focal volume. Thus, for a worse case scenario, we can set Δ_{lon} and Δ_{lat} to 12.5 microns. In addition, we need to account for Δ_{dev} by taking into account how the ellipsoidal reflectors are fabricated using the electroforming process. First a master of the ellipsoid is machined where the master geometry will not deviate from the specified

theoretical geometry by more than ±2 arc minutes of surface slope. Next, a metal, typically nickel, is electrodeposited over the master. This process introduces another ±30 arc seconds of error resulting in a mirror with a Δ_{dev} of 2.5 arc minutes.[i]

Using Mathematica® a relationship between the initial scattering angle, the sources of deviation (Δ_{lon}, Δ_{lat}, and Δ_{dev}), and the ray's intersect point on the detector was derived. This result is then used to determine to what accuracy the detector's pixels could be labeled with a polar scattering angles (θ). A plot of these accuracies over the polar angular range of 90° and 175° are shown in Figure 4-5. The dotted black curve represents the quadrature sum of each error component, and gives a rough estimate of the overall accuracy of the labeling technique. As is quite evident in the plot, the error increases with polar angle, therefore the mislabeling of angles will not a simple linear shift. This decrease in accuracy with increasing polar angle is combined effect from the mirror having a higher degree of curvature at these angles and the longer distance between the point of reflection and the detector plane.

[i] Although the two sources of error are uncorrelated and thus should be added in quadrature, the manufacturer's specifications were somewhat vague, and thus the worst case scenario was assumed.

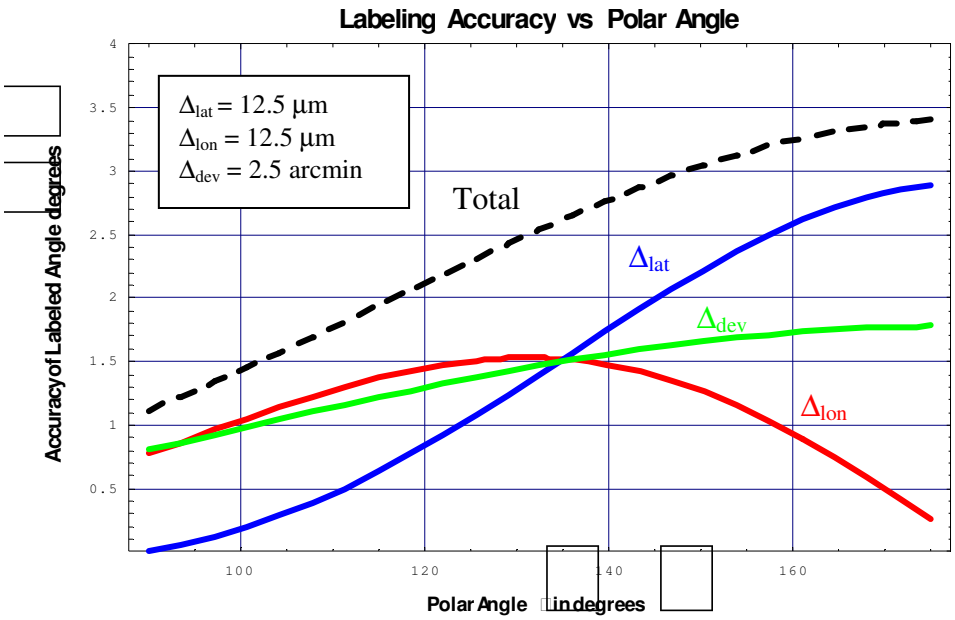

Figure 4-5: Accuracy of labeled angle as a function of initial scattering angle.

In addition, an exact ray-trace program was written in Matlab® to account for skew rays as well as to get a two-dimensional perspective of what these aberrations look like in the detected image. The program traces the path of a discrete number of rays starting from the particle's origin. Distortion in the shape of the ellipsoidal mirror (Δ_{dev}) is ignored. For the following three figures, the rays were uniformly spaced in both their azimuthal angle ($\Delta\phi = 15°$) and their polar angle ($\Delta\theta = 15°$). The output of the program for a perfectly aligned particle is shown in Figure 4-6. The first image on the top row is a spot diagram of the rays in the iris plane. As expected for a perfectly aligned particle, all the rays focus to a single point. The next plot to the right is of the rays' location in the detector plane. Note how the rays are compressed with respect to the polar angle (θ), which is also depicted in the next plot over to the right. In the lower half of the figure is a plot of the rays' path over a single scattering plane.

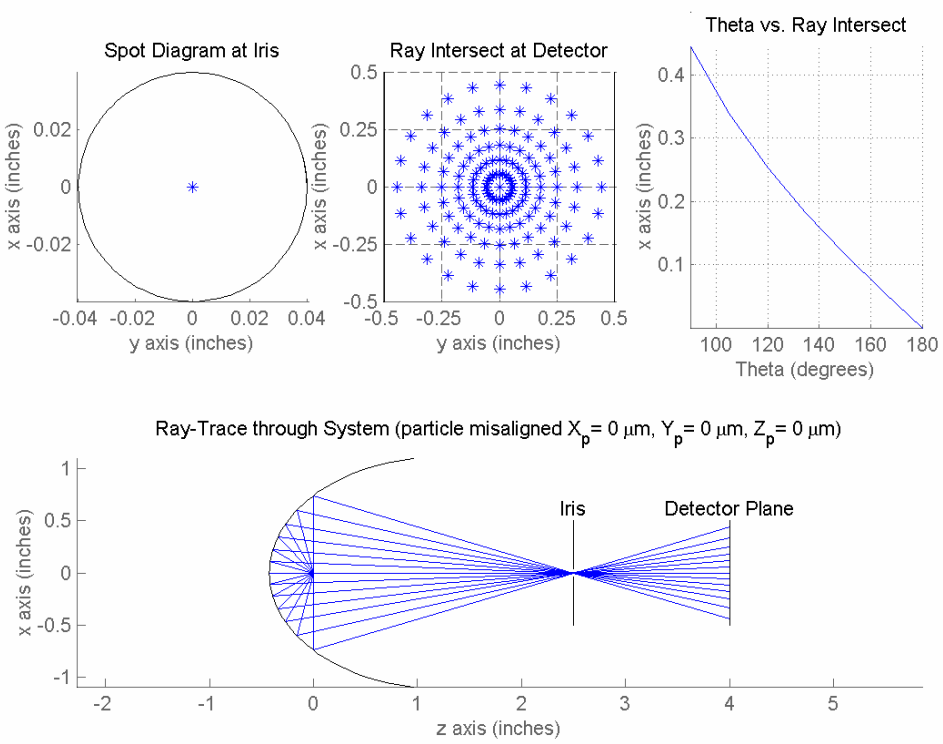

Figure 4-6: Exact ray-trace of ellipsoidal reflector for a particle perfectly aligned at the focal point.

Next, Figure 4-7 depicts the distortions in the pattern if the particle is shifted out of focus by 200 microns normal to the ellipsoid's major axis (Δ_{lat}). The red rays in the spot diagram at the iris and the ray intersect at the detector are the rays that would not have passed through the iris (diameter 2 mm) located at the second focal point of the ellipsoid. Thus, in the detected pattern, those areas represent by the red rays would just be black since no light would reach those pixels. Note that in the actually system, the particle should never be as far out of focus as 200 microns, that number was chosen so that the distortion is easily visible to the eye. The cross-beam trigger system should limit the misalignment shift to ~12.5 microns, in which all the rays will make it through the iris, but the detected pattern will still be distorted (see Figure 4-5).

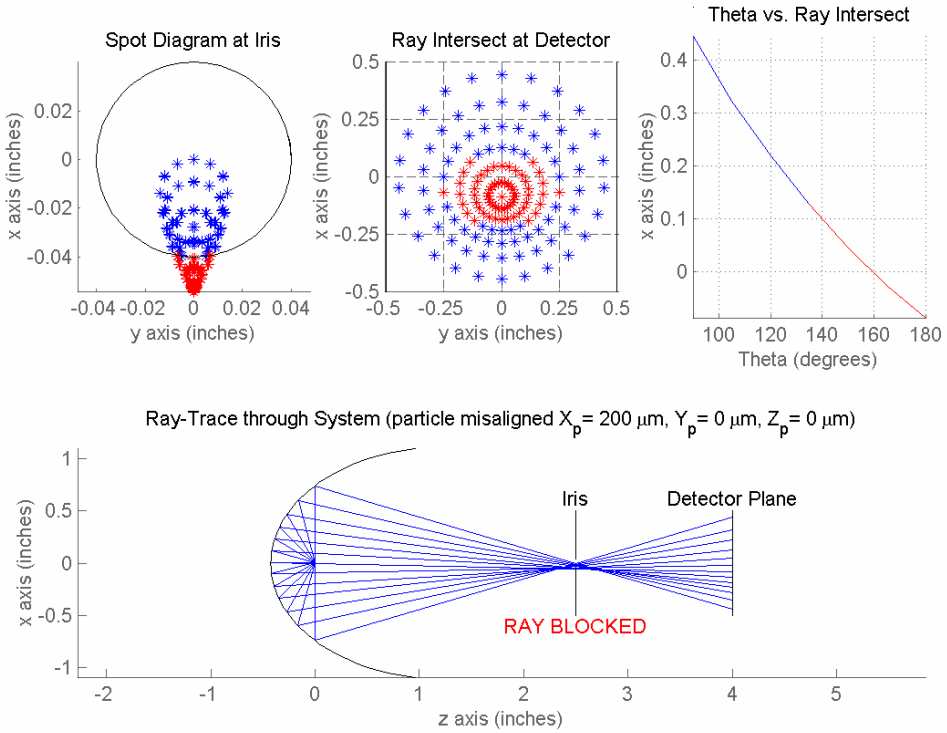

Figure 4-7: Exact ray-trace of ellipsoidal reflector for a particle misaligned by 200 microns parallel to the ellipsoid's minor axis.

Next, Figure 4-8 illustrates the error due to particle misalignment down the ellipsoid's major axis (Δ_{lon}). As expected the distortions are radially symmetric in the detector plane (no error in the azimuthal angle ϕ), however the polar angles are reasonably shifted from their perfectly aligned positions. It is interesting to point out that with this misalignment the relationship between polar angle (θ) and the ray intersect point at the detector has become slightly more linear. This is evident by looking at the plot labeled 'Theta vs. Ray Intersect' in Figure 4-8 and Figure 4-6.

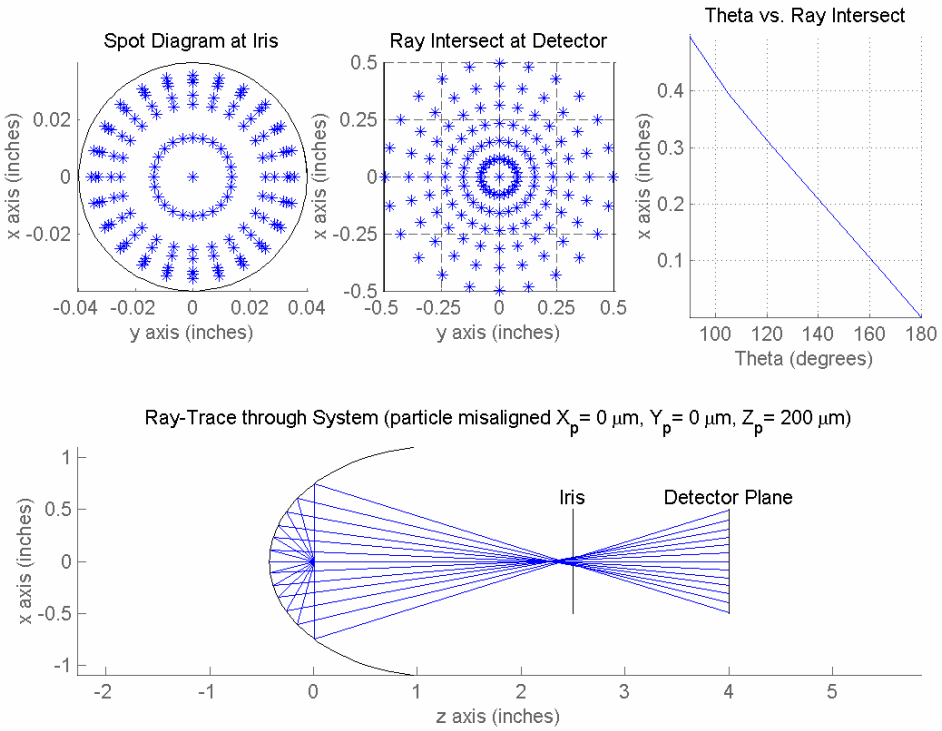

Figure 4-8: Exact ray-trace of ellipsoidal reflector for a particle misaligned by 200 microns down the ellipsoid's major axis.

Thus, from this analysis, it is quite evident that during the scattering event the particle has to be well localized so that the detected pattern is not severely distorted. To accomplish this task, a cross-beam trigger system is incorporated into the system, which can limit the particle's misalignment to 12.5 microns. The system is described in the next section.

4.2 - Optical Triggering for Particle Localization

The large collection angle of the LA TAOS system comes at a price: an extremely short depth of field. Other researchers have used an ellipsoidal mirror to collect elastic scatter from a single particle without having the particles well localized. In the device

designed by Gucker *et al.,* the aerosol particles where confined to an air-flow stream with a diameter of 1 mm. The data collected with this system could be post-filtered by looking for symmetry over the two azimuthal angles collected (ϕ = 90° and 270°) since only spheres were being investigated.[28] In the system designed by Kaye *et al.* the aerosol particles where confined to an 800 micron air-flow stream. In their studies, only gross features in the scattering pattern where being analyzed, so moderate distortions were not a concern.[11]

For this Thesis work, the instrument was developed so that the collected scattering patterns of both spherical and nonspherical particles could be compared with theory. With that in mind, the distortion that occurs for an airflow confined to a 400 microns diameter would be too large (see Subsection 4.1.3). The solution was to incorporate an optical trigger into the instrument that would only trigger the incident laser beam if the particle was sufficiently close to the first focal point of the ellipsoid. This technique was first used by Pan Y.L. *et al.* for the detection of single-particle fluorescence with a Schwartzchild objective lens, which has a short depth of field.[2]

The cross-beam trigger system is shown in Figure 4-9. Only particles that flow through the intersection two orthogonal continuous wave (CW) laser beams result in a trigger signal. The two CW diode lasers (Micro Laser Systems) emit light at 635 nm with a power of 25 mW and 685 nm with a power of 40 mW. The spot sizes of the two lasers are 25 μm and 13 μm respectively. The lasers are focused slightly above the first focal point of the ellipsoid to account for the delay in the pulsed laser source. PMTs (Hamamatsu) detect the scattered light as the particle traverses the two beams. A bandpass filter is placed in front of each PMT so that it is only detecting the scattered

light from a single diode beam. The outputs from the PMTs are feed into amplifiers (EG&G Ortec 570 – not shown), then into a single-channel analyzer (EG&G Ortec 850 – not shown), and finally combined with a logic AND gate (EG&G Ortec CO4020). The output of the AND gate then triggers both the pulsed laser source as well as the detector to capture the LA TAOS pattern. The single-channel analyzer is set to only pass pulses with a peak voltage within a certain window. This can be used to set a rough minimum size of the aerosol particles to be examined.

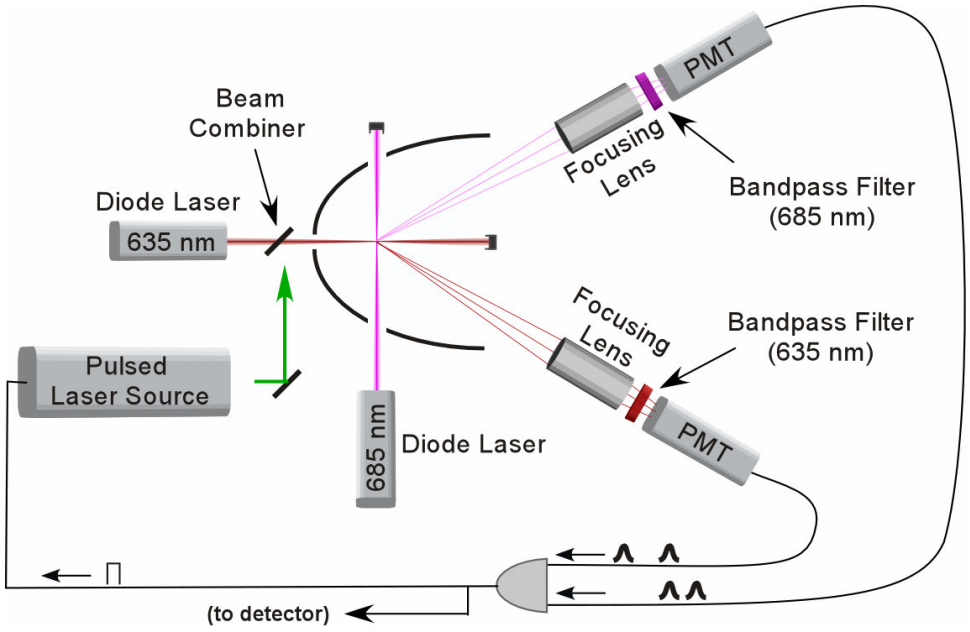

Figure 4-9: Design of the cross-beam trigger system. Only when a particle is traversing the focal volume of the mirror does it scatter light from both diode beams and trigger the pulsed laser source.

Before leaving this section, it should be noted that some experiments did not warrant a cross-beam trigger system. In particular, when using the MicroDrop Generator (see Subsection 4.3.4), the droplets are well localized since they exit the nozzle as a fine stream. In addition, the droplets arrive at the focal volume at a set frequency and thus the

lasers are not needed for timing either. In such situation, the cross-beam trigger system was not used.

4.3 - Aerosol Sampling and Generation

There are numerous instruments for particle sampling and generation, each with its advantages and limitations. Thus, for this work, different particle generators and sampling techniques were used depending upon what experiment was being conducted. In this section, these different instruments and techniques are reviewed.

4.3.1 - Natural Background Sampling

To sample outdoor aerosols from the natural background, a sampling scheme developed by Dr. Ronald G. Pinnick at the U.S. Army Research Labs was utilized.[42] A sketch of the system is shown in Figure 4-10. Since supermicrometer-sized particles have a low concentration in the ambient atmosphere, a virtual impactor (a Dycor model XMX) was used to draw in air off the roof at a rate of 770 L/min. The virtual impactor then concentrates particles within a size range of 2 – 20 microns into an exit air flow of 0.83 L/min. The particle-enriched air is then drawn vertically through a nozzle into an airtight aluminum box (dimensions 18 in × 18 in × 18 in). The nozzle is positioned just above (~1.5 cm) the scattering focal volume. Just below the scattering focal volume is an eduction tube is being driven by a constant-volume DC-motor-driven piston pump (KNF Neuberger, model UN05) that aspirates the box.

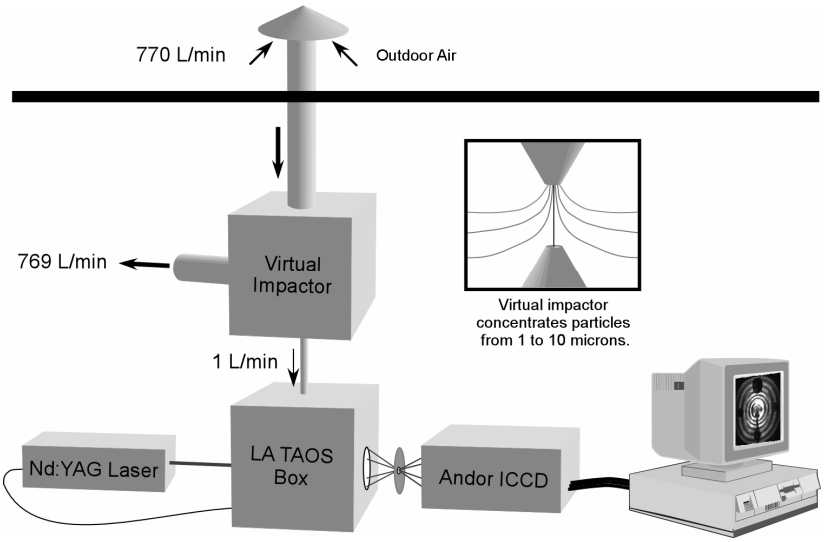

Figure 4-10: Sampling of ambient aerosol particles using a virtual impactor for LA TAOS experiment. Inset shows how particles with enough inertia are concentrated with respect to the carrier volume of air.

A difficulty in reliably sampling aerosol with this system is caused by the virtual impactor pump (used to aspirate the impactor) and the piston pump (used to aspirate the nozzle). These pumps cause pressure fluctuations and non-laminar flow through the focusing nozzle, which in turn cause particle trajectories to be unstable. To achieve laminar-flow of the aerosol through the nozzle a relatively large ballast tank (55 gallon drum with packing foam inserts) was installed between the virtual impactor concentrator and the concentrator pump to attenuate the pressure fluctuations. In addition a two-liter air ballast with suitable foam inserts was installed between the air-tight box and the piston pump. These ballasts reduce pressure fluctuations at the nozzle resulting in straight and uniform particle trajectories through the sample volume.

Using the IJAG system (described in Subsection 4.3.3), the sampling efficiency of an air-flow containing dried tryptophan particles with various diameters was determined. For particles with a diameter of 4 to 10 μm, the cross-beam trigger system of the LA

TAOS box was detecting approximately 1L/min of outside air. Assuming the efficiency of the virtual concentrator for this size range is 30%, the cross-trigger beam are only detecting about 0.4% of the aerosols entering the LA TAOS box. This result is equivalent to having an aerosol flow diameter of 400 μm and a defined trigger volume with a diameter of 25 μm, which correlates well with the experimental setup.

4.3.2 - Diesel Engine Sampling

A crude approach was used to sample a diesel engine. Using a large plastic leaf bag (~0.2 cubic meters) emissions from a Humvee under no-load were collected from the tailpipe. After filling the bag, the samples were quickly transported to the laboratory (the commute took about three minutes) and then slowly released into the inlet hose of the experimental chamber. The Humvee was running for approximately 5 minutes before samples were collected.

4.3.3 - Ink Jet Aerosol Generator (IJAG)

The Ink-Jet Aerosol Generator (IJAG) is used to generate dry aggregates from a suspension of primary particles and water.[43] The particle/water solution is loaded into an ink-jet cartridge (Hewlett Packard 51612A "Blankjet") that is then mounted on the top of a drying column. By applying short current pulses to the ink-jet cartridge's 12 nozzles, droplets with a diameter of approximately 50 um are generated. The number of primary particles within the water droplet follows Poisson statistics, and depends on the concentration of the slurry within the cartridge. By varying the initial concentration of primary particles in the suspension, aggregates of a particular size can be generated.

After being ejected from the ink jet cartridge, the droplets are often accompanied by small satellite droplets. These secondary droplets are removed with a winnow flow while the large primary droplet is entrained within an airflow that carries it through the drying column. The drying column is heated to ~105°C so that as the wet droplets with inclusions traverse the column, the water evaporates, leaving aggregate primary particles. However, these aggregates are not necessarily close-packed structures. Indeed, looking at the particles with a scanning electron microscope (SEM) they can appear as having a hollow core (see Figure 4-11(c)).

A conversation with Dr. Eric Dufresne of Yale's Mechanical Engineering Department shed some light on this effect.[44] Initially, as the droplets flow through the drying column, they shrink isotropically, as shown in Figure 4-11. As water continues to evaporate, crystallization takes place and small crystallized particles form throughout the volume. A shell of these crystallized particles begins to accrue at the air/water interface as particles pile up due to the receding boundary. This is due to the fact that the evaporation rate is much faster than the diffusion rate. The process continues until a thick shell is formed, after which further drying results in the shell either becoming deformed or cracked. Some examples of these shells are shown in Figure 4-11(c). The ammonium sulfate represents a cracked shell. The sodium chloride, which was expected to have a cubic-like structure, looks more similar to an igloo where small cubes form a spherical surface. Finally the tobacco particles look to be buckled spheres with noticeable dimples.

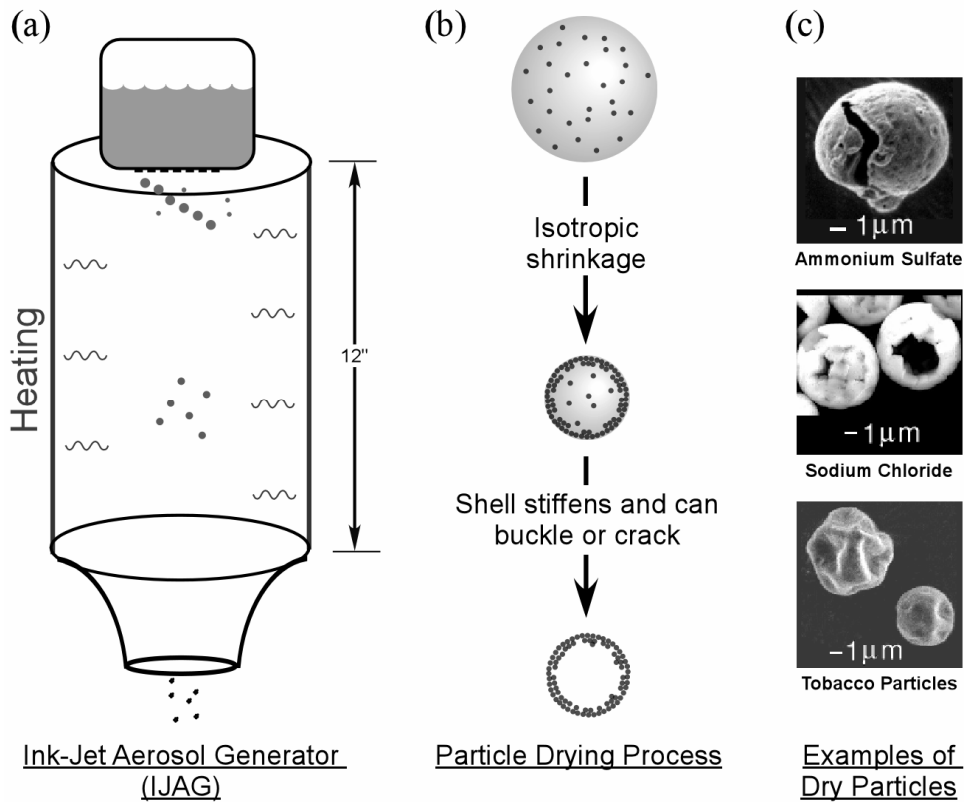

Figure 4-11: Shell formation in drying droplets of colloidal suspensions.

4.3.4 - MicroDrop Generator

The MicroDrop Generator (MicroDrop GmbH) can generate droplets on demand. The diameter of the droplets can range from 30-100 microns depending upon system components and viscosity of the liquid. The droplets generated for a given system are quite repeatable, although the system needed to be run at a set frequency (~500 Hz) to achieve this stability.[i] The generator can aerosolize liquid that have a viscosity between 0.5 mPa•s and 20 mPa•s (*e.g.* H_2O @ 20°C has a viscosity of 1 mPa•s). To reach higher viscosities, an alternate design of the system incorporating a heater can aerosolize liquids up to 10,000 mPa•s.

[i] Although no formal study was conducted, looking at the repeatability of the scattering pattern, the variation in droplet diameter appeared to be less than a micron.

The critical component of this instrument is a tubular piezo actuator that squeezes on a glass capillary, shown in Figure 4-12. While using the capillary tube as a reservoir, activating the piezoelectric transducer for a short duration (~50 microseconds) results in the emission of a droplet out of a nozzle located at the end of the capillary tube. It is the diameter of the orifice at this nozzle that roughly determines the droplet diameter.

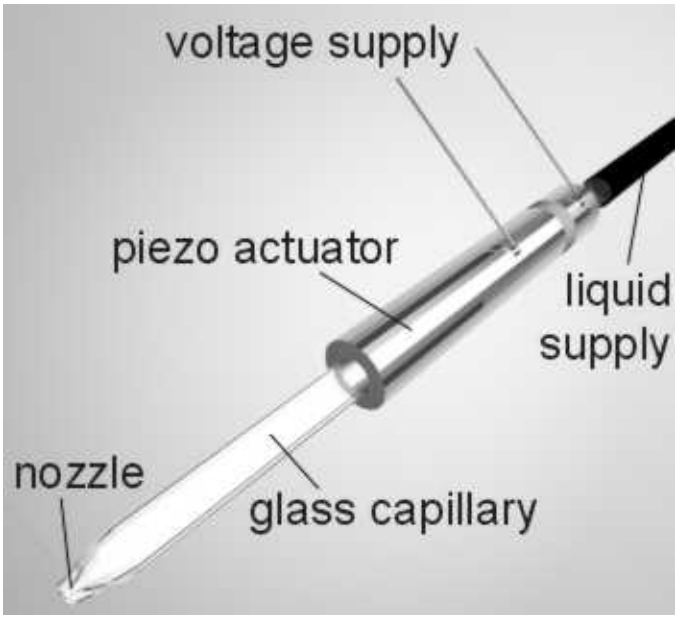

Figure 4-12: Inner-workings of the MicroDrop generator head [image from the website of MicroDrop GmbH].

4.3.5 - Royco Aerosol Generator

The Royco Aerosol Generator (model 256) is a wet dispersion generator that utilizes an atomizer. Air-blast atomizers use compressed air (15 to 50 psig) to draw bulk liquid from a reservoir as a result of Bernoulli's effect, as shown in Figure 4-12.[45] The high-velocity air-flow breaks up the liquid into a mist and carries it to the top of the air chamber where it exits out a gooseneck tube. The inertia of larger particles causes them to impact on the wall and drain back to the liquid reservoir. The airflow then carries the droplets through multiple drying chambers filled with circulating dry nitrogen gas. The

outlet hose is therefore composed of dry particles whose composition is determined by the initial composition of the droplets. This is an excellent way to generate single polystyrene latex spheres or single bacterial spores since the initial droplet sizes are quite small and therefore minimizes the amount of preservative or surfactant from the original solution that coats the particle of interest.

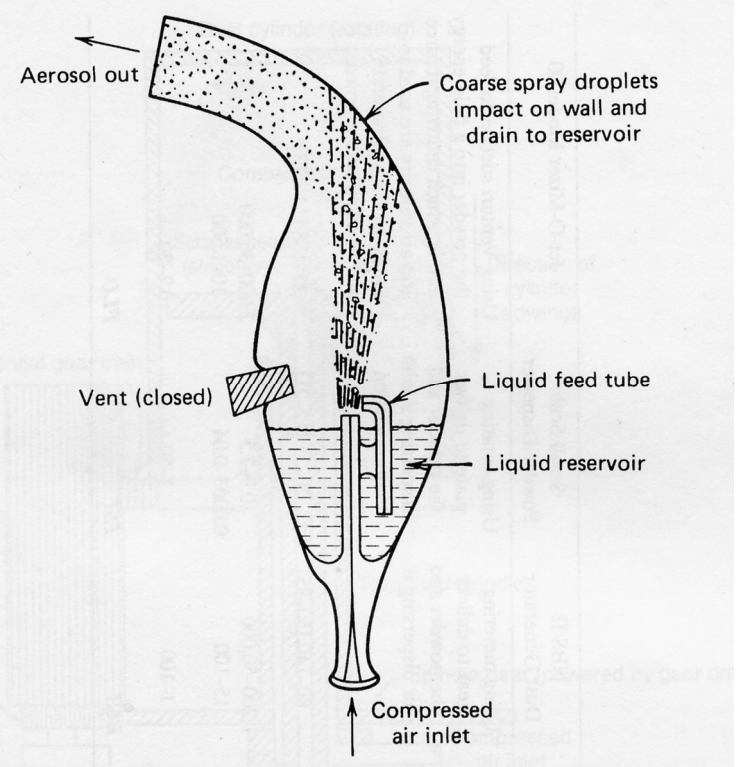

Figure 4-13: Drawing of a DeVilbiss Model 40 Glass Nebulizer. [Image from Hinds, *Aerosol Technology* (1999)]

4.3.6 - Vibrating Orifice Aerosol Generator (VOAG)

The Bergund-Liu vibrating orifice aerosol generator (VOAG) is another piezoelectric-based droplet generator.[46,47] The head of the VOAG consists of a 25 micron diameter orifice in a 3/8" nickel-copper or stainless steel disc, which is placed in the center of a stainless steel cup with a hole in its center. A ceramic piezoelectric ring is

epoxied to the flange of the cup. A liquid reservoir is connected to the VOAG head via a 0.5 Millipore filter and teflon tubing. The reservoir is pressurized at ~17.5 psi by a nitrogen cylinder and generates a liquid column as the liquid is forced through the orifice. The piezoelectric ring is driven with a 5 volt sine wave at a frequency of ~50 kHz using a synthesized function/sweep generator (HP 3324A). The vibration of the piezo electric ring within a certain frequency range causes mechanical perturbation in the liquid column exiting the orifice to form stable spherical droplets. The shape of these droplets initially oscillates between prolate and oblate, but these oscillations damp out at ~2 cm downstream.

4.3.7 - Collision Powder Disperser

The Collision Powder Disperser (CPD) is a converted Collision nebulizer where the main reservoir is filled with a dry powder instead of a liquid. A diagram of the Collision nebulizer is shown in Figure 4-14.[48] The function is similar to an atomizer except the particle laden jets are aimed normal to the side wall of the jar or a baffle. Impaction of the air/particle mixture against the sidewall/baffle leads to further atomization as well as a greater reduction in larger particles. To improve upon the powder generation process, the jets were pulsed on and off to introduce more turbulence inside the jar. The resulting cloud of particle is drawn from the top of the jar.

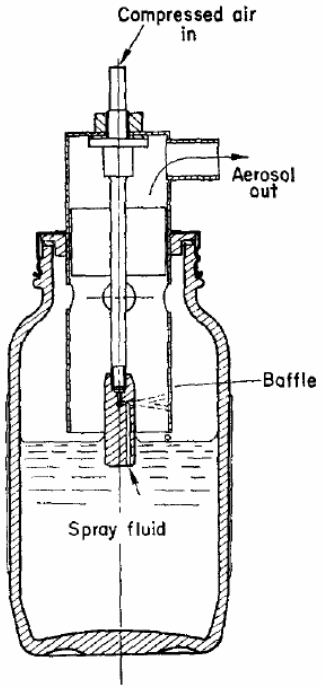

Figure 4-14: A sketch of the Collision nebulizer from May, "The Collision Nebulizer: Description Performance, and Application" (1973).

4.4 - Laser Sources and Detectors

The LA TAOS pattern generated from a scattering event does not only depend upon the morphology of the aerosol particle, but also depend on the wavelength of the incident beam. Indeed, particle features much smaller than the laser wavelength would not effect the LA TAOS pattern. Changing the wavelength of the illuminating laser is equivalent to scaling the aerosol particle, since it is the ratio of the laser's wavelength to the size of the particle's features that dictate the scattering pattern.

Beyond a relative scale factor, changing the wavelength of the illuminating laser can also vary in the complex refractive index $N(\lambda)$. Shifts in the refractive index are most evident when the laser wavelength is tuned on and off an absorption band resulting in large changes in the imaginary part of the refractive index. Strong absorption bands

stemming from molecular vibrational modes can be found in the mid-infrared (mid-IR).[i] To explore the possibility of extracting information about particle absorption using light scattering, a series of experiments were conducted in the mid-IR wavelength range.

Therefore two different wavelength ranges were utilized for this work. A majority of the experiments were done in the visible at 532 nm, particularly during the development phase of the LA TAOS system as well as for experiments relating to particle structure. For single particle absorption experiments, the initial set of experiments was performed in the visible to iron-out the mechanics of the LA TAOS setup. Then a series of experiments were conducted in the mid-IR (3.4 μm, 3.9 μm, and 5.1 μm) where strong absorption bands exist stemming from molecular vibrational modes. The subsections below describe the detector and laser sources used for each wavelength range.

4.4.1 - Visible Wavelengths

For LA TAOS patterns captured at visible wavelengths, two different diode pumped laser (Spectra Physics model X-30 and YHP-70) were used depending upon the experiment location. Both are fiber coupled, diode-pumped, Nd:YAG laser systems which are then frequency doubled using a nonlinear crystal (lithium triborate) to generate light at 532 nm. A critical feature of these lasers is their ability to be triggered on-demand with a delay of only ~1 microsecond and a jitter of 15 nanoseconds. This is critical since the particles can arrive at the focal volume of the setup at random intervals. The main difference between the two laser systems is their pulse-widths. The X-30 has a nominal 30 nsec pulse-width where as the YHP-70 has a 70 nsec pulse-width. This has minimal

[i] The mid-IR wavelength range is roughly from 2.5 microns to 25 microns.

effect on the scattering patterns since on these time scales the particle appears frozen in position.

Three different detectors, two Intensified-CCDs (ICCD) and one CCD, were used through-out the experiments. A full-frame transfer back-thinned CCD with a format-size of 1044×256 (Hamamatsu Corp., HC230-1008) was used for the absorption experiments in the visible (see Subsection 5.1.1). A 512×512 format size ICCD (Princeton Instruments, Model LCI-4) was used for initial LA TAOS experiments (see Subsection 5.2.1) and a 1024×1024 ICCD (Andor Technology, Model DH734-25F-03) was used for the rest of the experiments.

4.4.2 - Mid-Infrared Wavelengths

Sources in the mid-IR are not locally available, so these experiments required scheduling bench time with prototype systems at the Army Research Laboratory (ARL) as well as at the Massachusetts Institute for Technology's Lincoln Labs (MIT-LL). The ARL laser was liquid nitrogen cooled type-II InAs/GaInSb interband cascade laser operating in CW mode. It generates light at a wavelength of 3.41 μm with optical powers approaching 40 milliwatts.[49,50] The MIT-LL lasers were optically pumped GaSb-based semiconductor lasers with type-II InAs/InGaSb quantum well gain regions emitting at 3.9 μm and 5.1 μm with a peak power of ~0.4 watts and pulse duration of 100 μs.[51,52] The mid-IR detector for all the experiments was an InSb 320x256 focal-plane-array (Santa Barbara Focal Plane) and was run at a frame rate of 63.13 Hz with an integration window of 217 μs.

Chapter 5: Results and Discussion

This chapter is divided into two sections. The first section discusses the use of elastic scattering to measure single particle absorption. Experiments were first conducted in the visible and then later in the mid-infrared. The second section concentrates on extracting particle morphology from LA TAOS patterns. In particular, simple metrics were extracted from the LA TAOS patterns to classify different aerosols.

5.1 - Single Particle Absorption Measurements

Infrared (IR) absorption spectra can be thought of as a fingerprint for chemical agents. Thus, by measuring the IR spectra from aerosol particles, one can classify different types of aerosols and discriminate between those that pose a health threat and those that are harmless constituents of the ambient atmosphere. However, measuring absorption at the single particle level is a trying task. Typically, one measures the extinction of an incident beam to determine the absorption in aerosols. However, the scattering cross-section can be equal to if not larger than the absorption cross-section, thus it is difficult to differentiate between the two when making this measurement.

Of course, the scattering and absorption from a single particle are not mutually exclusive events, but are linked. In particular, absorption will effect the angularly-resolved scattering pattern through the imaginary component of the complex refractive index. Therefore, two series of experiments were conducted to explore whether single particle absorption information could be extracted from TAOS and LA TAOS patterns. The first set of experiments was conducted in the visible and showed promising results. The second set of experiments used an incident laser in the mid-IR, where stronger

absorption bands, stemming from molecular vibrations, exist. In particular, an experiment was conducted that captures two LA TAOS patterns simultaneously at two different wavelengths. By comparing the patterns, one can decipher if one of the laser wavelengths is on a strong absorption band.

5.1.1 - Visible Wavelengths

The first set of experiments was performed with the second harmonic from an Nd:YAG laser (532 nm) laser source. Numerical simulations were run based on Lorenz-Mie theory to project the effect of increasing absorption (κ, imaginary part of the refractive index) on the scattering pattern, as shown in Figure 5-1. The sphere's radius for this calculation is 56.22 μm and the real part of the refractive index was set to 1.36, where κ in the inset is the imaginary part of the refractive index. These values were chosen to match the parameters of a future experiment. The slice of data is from the scattering plane perpendicular to the polarization of the incident beam. By increasing absorption, one would expect the overall intensity of the scattering pattern to be reduced; however there is also a change in the profile of the scattering curves. For instance, the peak-to-valley ratio increases with increasing the absorption, although this relationship does not always hold true. Since the profile of the scattering curves changes with absorption, ideally a curve-fitting algorithm could be used to determine the strength of the absorption for a specific curve even if the absolute intensities are unknown.

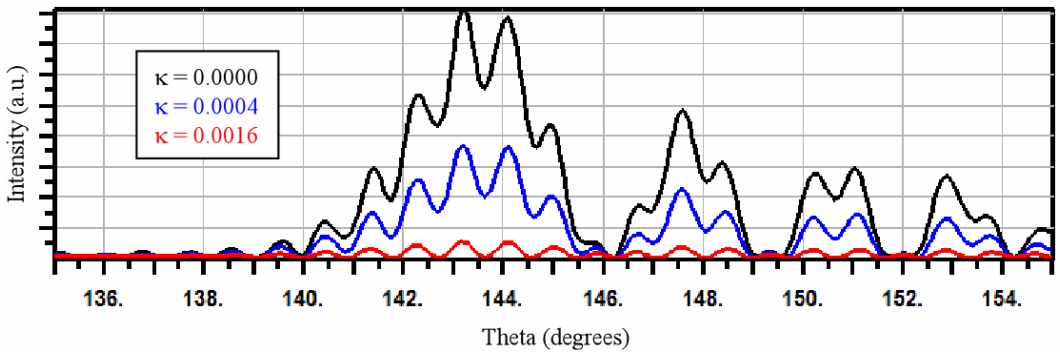

Figure 5-1: Lorenz-Mie theory prediction of the effect of increasing particle absorption on the TAOS pattern.

An experiment was conducted in hopes of reproducing the numerical simulation results. The LA TAOS setup was utilized with a back-thinned CCD as the detector. The CCD was positioned to detect the scattering angle (θ) from 135° to 155°. The pixels spanning the azimuthal angle (ϕ) were binned over to reduce noise. Using the VOAG droplet generator, a stream of ethanol droplets doped with Rhodamine 6G was introduced to the setup. Three different solutions were analyzed with Rhodamine concentrations 0.0 g/L, 0.1872 g/L, and 0.75 g/L to match κ values of 0.0000, 0.0004, and 0.0016 respectively. The frequency generator used to drive the VOAG was downsampled to a rate of 100 Hz to trigger the Nd:YAG laser (70 ns pulse width). This meant that the droplets were being illuminated every 10 msec and thus only a single scattering event would occur during the intergration time of the detector (10 msec). Since the droplet diameter would vary from solution to solution, each solution had to be independently measured by collecting a large quantity of solution over an extended time and then, by knowing the generation rate of the droplets, the droplet diameters could be projected. The error in the process is approximately 0.5 microns.

Figure 5-2 compares our experimental results with theoretical predictions. The peaks are well aligned and the curves are a fairly good fit for the two lower absorption cases. The highest absorption case suffers from signal to noise issues and thus the valleys in particular appear to be offset from theoretical prediction. A similar data set was later collected using an identical setup and processed by Mario Surbek. Surbek found that κ could be determined to within 0.0001 using an least-squares curve matching algorithm.[53] These results suggested that future experiments in the mid-IR could successfully extract single particle absorption from droplets.

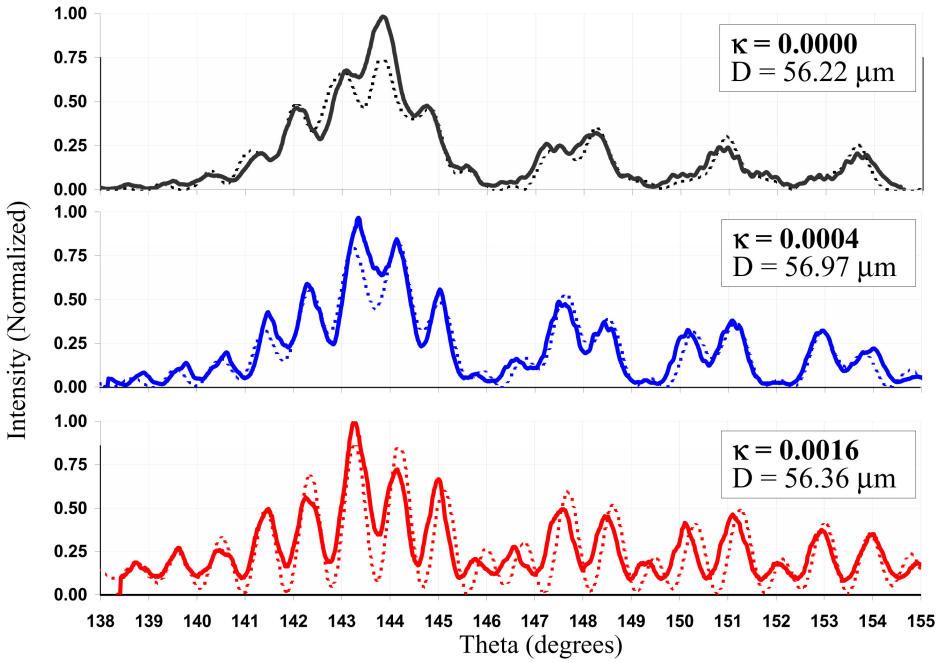

Figure 5-2: Angularly-resolved scattering intensity for different absorption strengths. Solid lines are the experimental results whereas dotted lines are based on Lorenz-Mie theory.

Figure 5-3 gives a physical interpretation of why increasing the absorption of a droplet leads to a larger peak-to-valley ratio. As shown in the figure, κ can be converted to an absorption coefficient α which represents how quickly a ray is extinguished in the

droplet. For example, using α one can calculate the path length for the intensity to drop by e^{-1} (~37%). For $\kappa = 0.0004$, this path length would be 106 μm, thus rays that traveled this distance within the droplet would be significantly absorbed. On a larger scale, increasing absorption reduces the number of rays that interfere in the far field. By reducing the number of components that play a role in the far field interference pattern, the pattern becomes simpler with a larger peak-to-valley ratio.

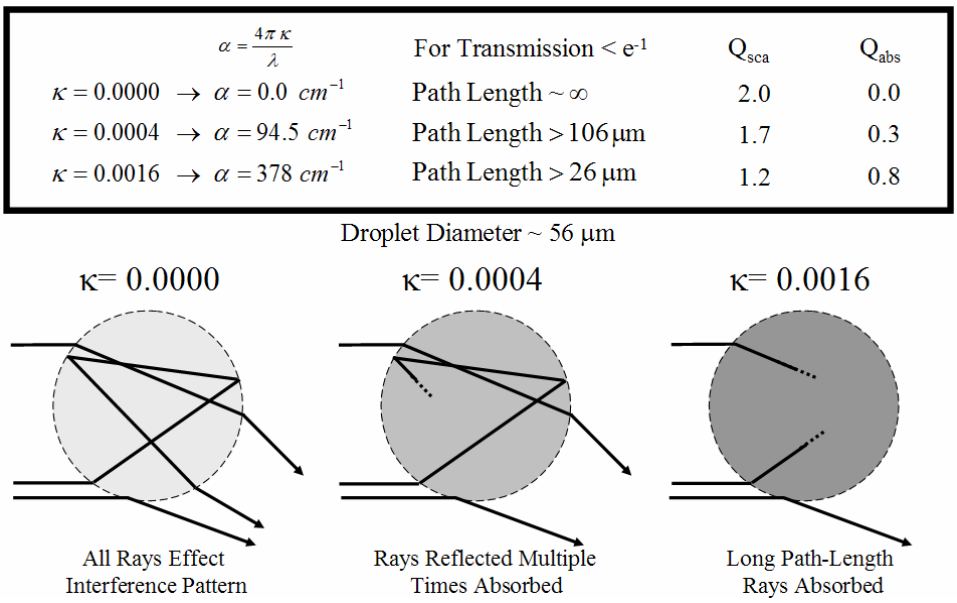

Figure 5-3: The effect of increasing absorption on rays reflected and refracted through a droplet.

5.1.2 - Mid-Infrared Wavelengths

Critical to running experiments in the mid-IR was finding an appropriate laser source. Such lasers existed only as prototypes on optical tables located in a few labs across the country. In particular, there has been a recent surge in research effort to develop quantum cascade laser sources that could operate at room temperature. These lasers would be very compact, approximately the size of a standard laser pointer, ideal for a component in a stand-alone light scattering commercial product. However, currently

the lasers are still quite temperamental and require cooling at liquid nitrogen temperatures. This necessitated the experimental setup to be transported to a lab where a prototype mid-IR lasers could be found.

The initial set of experiments was conducted in collaboration with Dr. Richard L. Tober at the US Army Research Laboratory. The TAOS setup was employed, rather than the LA TAOS setup, since it is simpler in design and therefore easier to transport and construct. After a level of comfort was reached working the mid-IR lasers, a second set of experiments was conducted using the LA TAOS setup. These experiments were performed in collaboration with Anish Goyal and Thomas Jeys at the MIT Lincoln Laboratory using two incident mid-IR lasers. This was the first time that simultaneous angularly-resolved elastic scattering patterns at two wavelengths have been captured.[54]

5.1.2.1 - TAOS Patterns of Droplets

For the first set of TAOS experiments conducted at the US Army Research Laboratory, a MicroDrop generator generated droplets ranging in diameter 54 μm to 57 μm composed of three different solutions: distilled water (H_2O), deuterium oxide (D_2O), and a 50%-50% mixture of H_2O and D_2O. See Subsection 4.1.1 for a discussion of the experimental configuration. The laser source was a type-II InAs/GaInSb interband cascade laser operating in CW mode to generate light at a wavelength of 3.41 μm with optical powers approaching 40 milliwatts. The emission from the facet of the semiconductor cavity was quite divergent, requiring an *f*/1 CaF_2 bi-convex lens to collimate the emitted light. In addition, an *f*/3.75 ZnSe bi-convex lens focused the collimated light onto the droplet to increase signal intensity. An *f*/2 CaF_2 plano-convex

lens collimated the scattered light onto the detecting focal plane array. The lens' optic axis was at $\theta = 35°$ and $\phi = 270°$ while the laser beam was polarized along the x-axis.

The angular range of collected light spanned 23° from $\theta = 23.5°$ to $\theta = 46.5°$. However, because of severe spherical aberration in the outer limits of the angular range the practical collection range was 26° to 42°. These effects were mitigated by performing an exact ray-trace on the system calculated in Matlab®. The detector, an InSb 320x256 focal-plane-array (Santa Barbara Focal Plane), was run at a frame rate of 63.13 Hz with an integration window of 217 μs so that only a single scattering event would be detected in each frame.

A TAOS pattern for each type of solution is shown in Figure 5-4 (a-c). The effects of spherical aberration can be noted by the increase in intensity around the perimeter of the TAOS pattern. There is also read-out noise that manifests itself in the TAOS patterns as horizontal lines. In addition, since the laser intensity fluctuated throughout the experiment, the absolute intensity between TAOS patterns cannot be compared. A vertically binned (45 pixels) horizontal slice from each type of TAOS pattern is plotted in Figure 5-4(d-f) together with analytical data based on Lorenz-Mie theory.

The droplet diameters to calculate the Lorenz-Mie theory curves were estimated by measuring an accumulated volume of droplets generated at the chosen frequency over a fixed time; complex refractive index values were taken from the literature.[55] To calculate the complex refractive index of the H_2O-D_2O mixture, a linear average was taken of the H_2O and D_2O refractive index. There is up to a 1° inaccuracy in the procedure used to measure the scattering angles, thus the angle range was slightly shifted (<1°) from the measured values to fit the data to theory. The experimental data shows a

good match with numerical data based upon Lorenz-Mie theory although the residual effects of spherical aberration can be seen at the edges of the plotted angular range. Because of the spherical aberrations in the TAOS patterns and the inaccuracies in the scattering angles and droplet diameters, the data was not sufficiently accurate for us to determine particle's absorptivity by comparing the experimental angular scattering with theory.

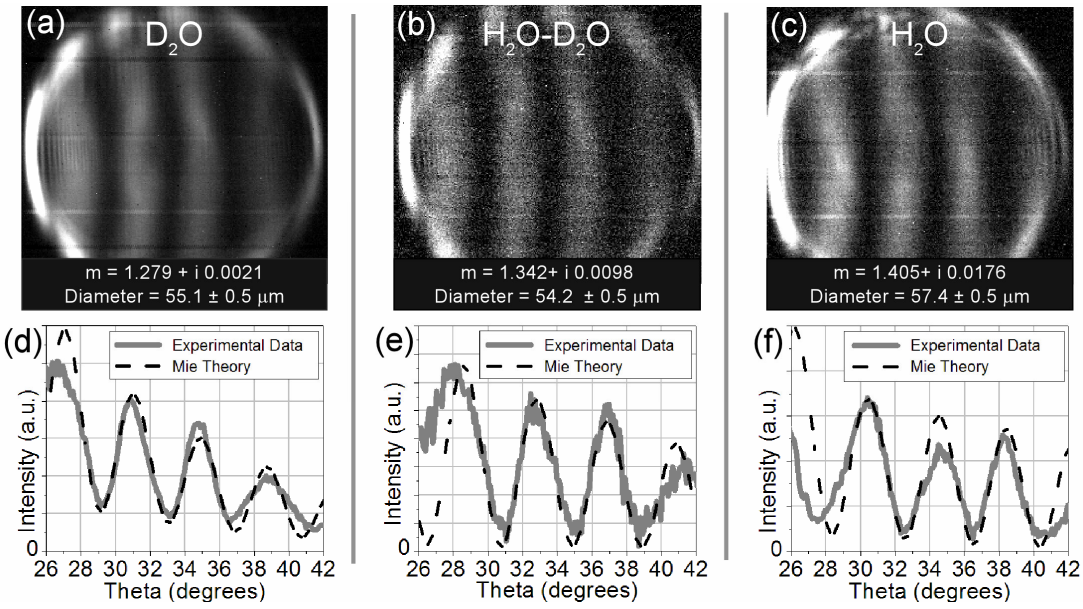

Figure 5-4: (a)-(c) Detected TAOS patterns from droplets composed of D_2O, a 50%-50% mixture of H_2O and D_2O, and H_2O. (d)-(f) Horizontal slices of the collected TAOS patterns compared with Lorenz-Mie theory calculations.

5.1.2.2 - LA TAOS Patterns of Aerosols

The scheme to collect LA TAOS images at two wavelengths simultaneously is shown in Figure 5-5. The two laser sources were optically pumped GaSb-based semiconductor lasers with type-II InAs/InGaSb quantum well gain regions emitting at 3.9 μm and 5.1 μm with a peak power of ~0.4 watts and pulse duration of 100 μs. Both wavelengths are relatively transparent for H_2O, but D_2O has relatively high absorption at

3.9 μm while being transparent at 5.1 μm. For D_2O, the imaginary component of the refractive index (κ) is 0.260 at 3.9 μm in contrast to 0.002 at 5.1 μm. Beam shaping optics (spherical and cylindrical lenses) as well as an F/3.75 CaF_2 focusing lens were utilized to achieve a desired spot size of 50 μm x 500 μm where the major axis is perpendicular to the propagation direction of the droplet. The polarizations of both laser beams were perpendicular to the propagation direction of the droplets. An ellipsoidal mirror collected the backward hemisphere of scattered light ($0° \leq \phi \leq 360°$, $90° \leq \theta \leq 163°$) and focused it through a spatial filter located at the ellipsoid's second focal point. To reduce aberrations effects, an F/1 ZnSe aspheric lens collimated the scattered light, after which the two wavelengths were separated via a dichroic mirror. Finally, a bi-convex F/1 CaF_2 lens coupled the scattered light onto the InSb detectors.

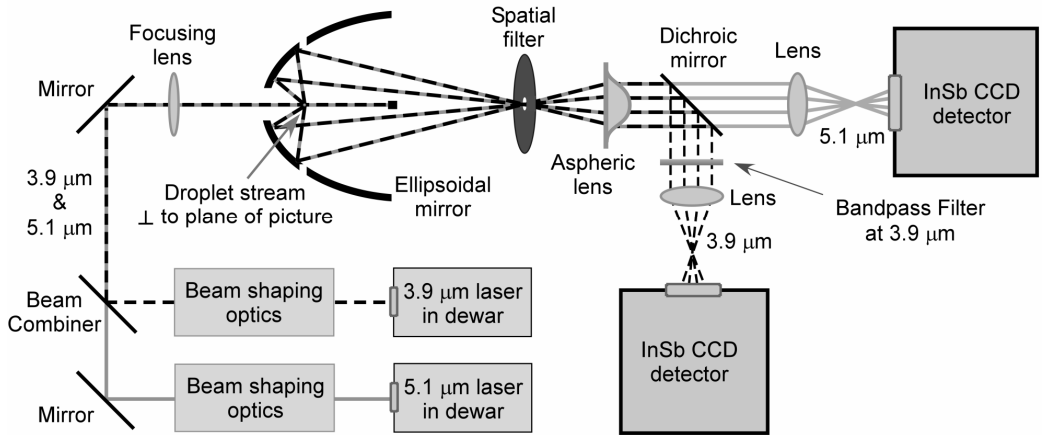

Figure 5-5: Experimental setup for collecting simultaneous LA TAOS patterns at two wavelengths in the mid-IR.

Droplets from three different mixtures of H_2O-D_2O were analyzed: 100%-0%, 75%-25%, and 50%-50%. The experimentally collected data, as well as numerical simulations based on Lorenz-Mie theory, are shown in Figure 5-6. There are several experimental artifacts embedded in the TAOS patterns because of: (1) the shadow of the

droplet generator nozzle protruding into the ellipsoidal mirror; (2) the shadow of the beam block mount; and (3) the diffraction of the illuminating laser beam around the beam block. Note that the patterns were processed to be linear in θ by taking into account the optical arrangement of the system.

The TAOS patterns shown in Figure 5-6 were collected from single droplets illuminated simultaneously by the two collinear 3.9 μm and 5.1 μm laser beams. Each column from left to right indicates a different H_2O-D_2O droplet composition, as labeled. TAOS patterns (row I) collected at 3.9 μm show the effects of increasing the concentration of D_2O that leads to an increase in absorption. These patterns qualitatively match the numerical simulations based on Lorenz-Mie theory (row II), although there appears to be some discrepancy for the 75%-25% case (comparison between (b) and (e)) believed to be due to oversimplification in estimating the absorption by taking a linear interpolation of known absorption values for neat fluids and ignoring effects of isotopes.[56] TAOS patterns (row III) are collected simultaneously at 5.1 μm from the same single droplets. These patterns also agree with predictions from Lorenz-Mie theory in which there was a slight increase in scattering intensity of the central region ($\theta > 135°$) with increasing concentrations of D_2O. For the numerical simulations, the droplet diameter was estimated to be 55 μm and the refractive index was gathered from the literature.[55] By comparing the data in row I with row III, it is clear that one could distinguish between droplets of pure H_2O and droplets that contain a considerable amount of D_2O by comparing the angular scattering patterns.

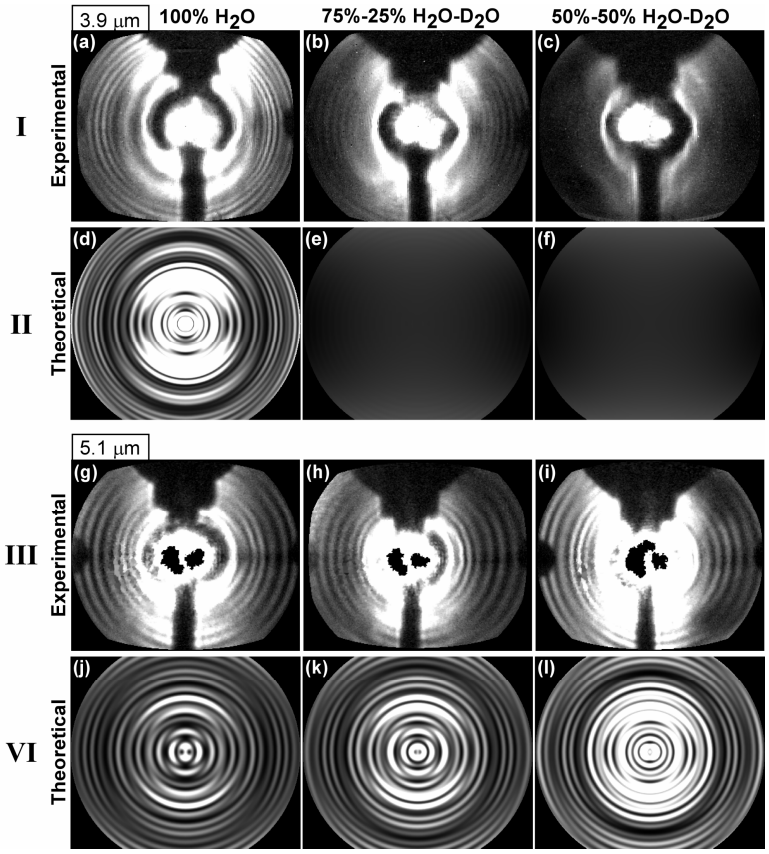

Figure 5-6: (Row I) TAOS pattern at λ = 3.9 μm detected from a single droplet (diameter ~ 55 μm) composed of (a) H_2O, (b) 75%-25% H_2O-D_2O, and (c) 50%-50% H_2O-D_2O. (Row II) Corresponding numerical simulations of row I based upon Lorenz-Mie theory. (Row III) TAOS pattern collected simultaneously at 5.1 μm from the same single droplets as row I. (Row IV) Corresponding numerical simulations of row III based upon Lorenz-Mie theory.

With the same experimental setup as above (see Figure 5-5), LA TAOS patterns were collected from 8 μm aggregate particles and solid particles generated with the IJAG, as shown in Figure 5-7. The LA TAOS patterns from four particles are shown: L-Tryptophan (Sigma, lot# 127H0622), Bovine Albumin (Sigma, lot# 123H0800), cluster of *Bacillus subtilis* var. *niger* spores (Dugway Proving Grounds), and a cluster of polystyrene latex spheres (Duke Scientific, diameter 1.44 μm). The LA TAOS patterns were examined to determine if there is a noticeable difference due to the shift in

wavelength. However, the low pulse energy of the mid-IR lasers (in particular the 5.1 μm source) resulted in a poor signal-to-noise ratio. Since the scattered energy goes as the square of the particle radius, then switching from a 50 μm diameter droplet to an 8 μm diameter particle reduces the scattered energy by approximately a factor of 40. With such low energy, it was difficult to determine what effects absorption played on the scattering.

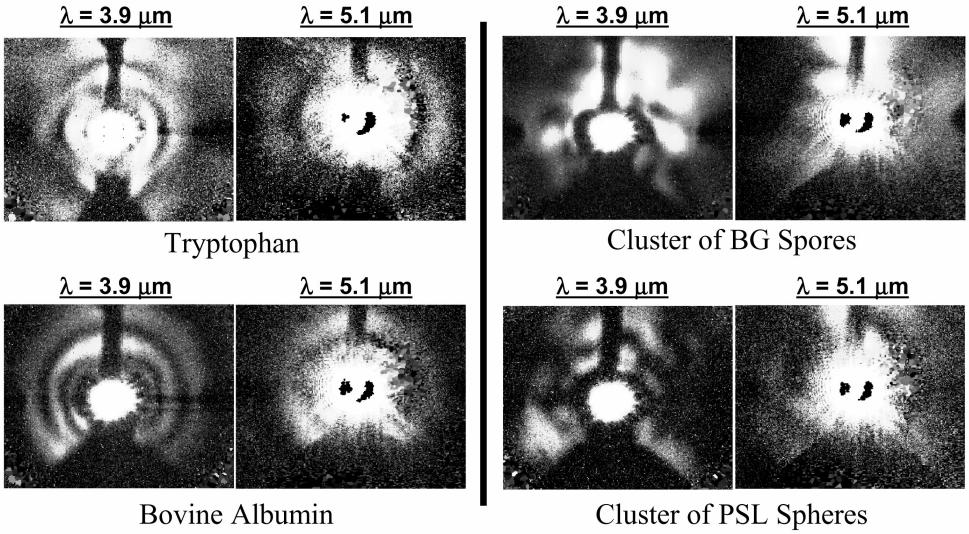

Figure 5-7: LA TAOS patterns of 8 μm aerosol particles captured simultaneously at two wavelengths.

Certain features are distinguishable in the TAOS patterns, although not associated with absorption. In particular, the ring-like patterns for the solid particles Bovine Albumin and Tryophan are quite evident. This suggests that the particle looked spherical with respect to the illuminating wavelength and thus the size of the surface roughness features or internal structure of the aerosol particle is much less that 3.9 μm. The same does not hold true for the aggregate particles where the ring-like features are nowhere near as pronounced. This stems from the aggregate structure that introduces refractive index inhomogeneities that are on the order of the incident wavelength.

5.2 - Aerosol Characterization

A main emphasis of this research is to extract the morphology of single aerosol particles using elastic light scattering. The focus of the preceding section was on determining single particle absorption from LA TAOS and TAOS patterns. In this section, other particle features are characterized using the LA TAOS technique.

5.2.1 - Forward and Backward Scattering Hemispheres

In the first series of experiments, the LA TAOS configuration (see Figure 4-2) was used with a single cw trigger laser perpendicular to the incident beam (pulsed laser source) axis. With this setup, either the forward hemisphere or backward hemisphere of light can be detected depending upon the direction of the pulsed laser source, as shown in Figure 5-8. Using the IJAG, single particles and clusters were generated of polystyrene latex (PSL) spheres and *Bacillus subtilis* spores.

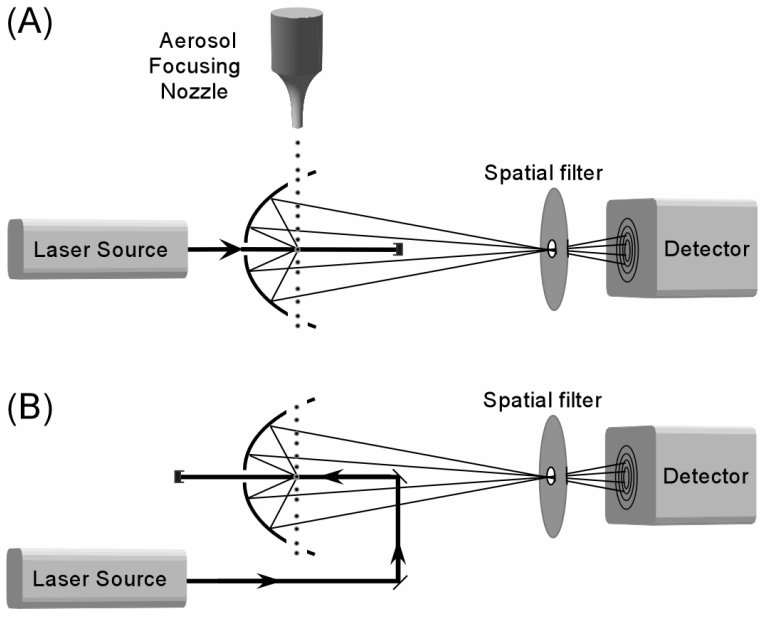

Figure 5-8: Two different arrangements to collect LA TAOS patterns: (A) collects the backward scattering hemisphere and (B) collect the forward scattering hemisphere.

Figure 5-9 shows the collected backward and forward LA TAOS patterns from a single polystyrene latex (PSL) sphere and two clusters. The forward and backward patterns were not collected simultaneously. The center of the forward scattering pictures represents $\theta = 0°$ whereas for the backward scattering patterns this corresponds to $\theta = 180°$. The outer edge of all the pictures is approximately $\theta = 90°$. Just like the images presented in Subsection 5.1, there are artifacts in the patterns dues to the experimental setup. These include the black bar on the center-bottom of the images due to the beam block post as well as the hole in the center of the pattern and the four sections of a hole on the perimeter of the LATAOS pattern these are due to the holes in the ellipsoidal reflector.

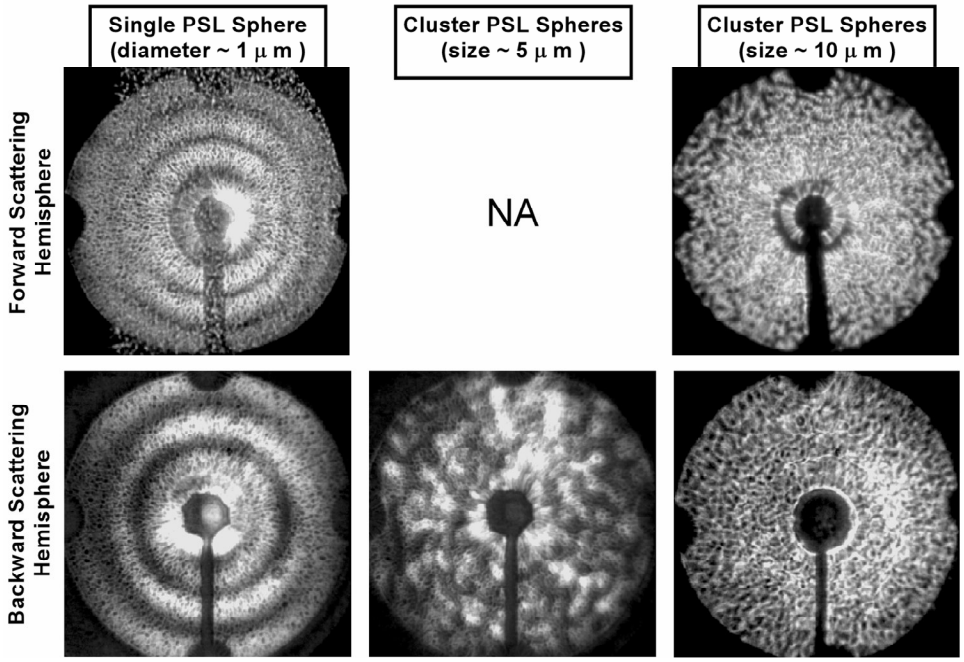

Figure 5-9: Forward (top row) and backward (bottom row) LA TAOS patterns collected from single PSL spheres (diameter = 0.988 μm), 5 μm cluster of PSL spheres, and a 10 μm cluster of PSL spheres.

The LA TAOS patterns from a single PSL sphere (diameter = 0.988 μm) have the expected ring structure. For a single sphere, the number of minima in the scattering plane ($\theta = 0°$ to 180°) is approximately kR, where $k = 2\pi/\lambda$ and R is the sphere radius.[57] For a 1 μm sphere illuminated with a 532 nm laser source, rounding off to the nearest integer, the number of minima is approximately six. This result matches well with the LA TAOS images where five minima are apparent and a sixth minimum is lost in the backward hemisphere LA TAOS pattern since it is too close to the center of the image and is hidden behind the noise due to the incident beam diffracting around the beam block.

The clusters of PSL spheres deviate greatly from the scattering of a single sphere. Scattering from clusters of PSL spheres has been explored by Holler *et al.* who collected TAOS patterns from clusters of 13 PSL sphere with a diameter of 1.33 μm.[13,39] In this work, the number of islands or more precisely the number of peaks and valleys is shown to increase with the diameter of the cluster. The backward LA TAOS patterns of the 5 μm cluster and 10 μm cluster follows trend.

In addition, the LA TAOS patterns from a single *Bacillus subtilis* (BG) spores as well as a cluster of BG spores were collected, as shown in Figure 5-10. The scattering patterns from BG spores are of particular interest since BG is a simulant of Anthrax. Similar to the PSL spheres, there is a trend of increasing island densities in the patterns with increasing cluster size. The LA TAOS patterns from single BG spores have a fair number of islands that appear randomly distributed. This is surprising since BG spores are pill shaped with a length of ~1 μm and a diameter of ~0.5 μm, one would expect to see a higher level of symmetry in the pattern even given the random orientation of the spore. It is suspected that upon generating the single BG spores with the IJAG some

preservative or surfactant coated the spore. To generate a single BG spore, the IJAG generates a 50 μm water droplet containing a single spore. Using a drying column, the water evaporates resulting in a single spore; however residue in the water will also be left to coat the spore.

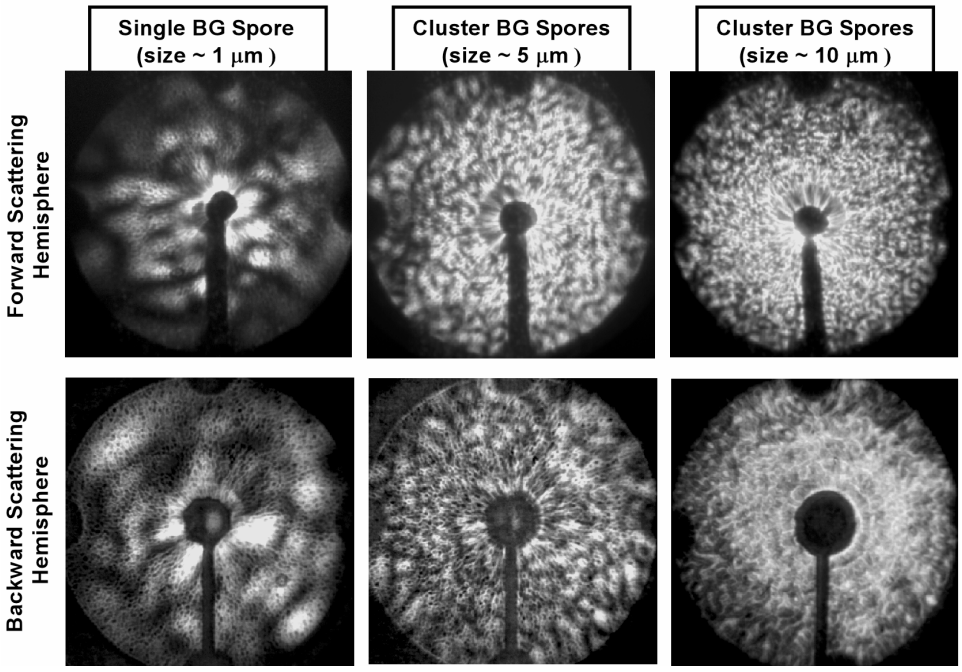

Figure 5-10: Forward (top row) and backward (bottom row) LA TAOS patterns collected from single BG spores, 5 μm clusters of BG spores, and 10 μm clusters of BG spores.

For the rest of the experiments in this chapter, we limited ourselves to a single experimental geometry. We choose to collect the backward hemisphere of scattered light for the following reasons. First, the intensity of the forward lobe of scattered light is proportional to D^4, where D is the particle's diameter.[58] Thus, the forward intensity can be several orders of magnitude stronger than in other directions. This will increase the dynamic range demands on the detector, particular if a range of particle sizes will be examined. Second, initial experiments conducted by Holler *et al.* show a lower density

of islands in the backward than in the forward direction.[39] Detecting a lower density of islands will reduce the resolution requirements of the detector. Finally, Kaye, Hirst, and coworkers have a similar system in which they concentrate on the forward scatter.[4,11] They follow a long tradition of extracting particle shape by examining the forward scatter, since the shape of the forward scattering lobe is well described by the Fraunhofer diffraction theory.[58] Therefore, investigating the features in the backward scattering hemisphere is a road less taken and thus fertile ground.

5.2.2 - LA TAOS Patterns and SEM Images of a Hodge-Podge of Aerosols

What is the source of the island like features in the LA TAOS patterns of Figure 5-9 and Figure 5-10? How do these islands vary with particle type? An experiment conducted with Mario Surbek attempted to answer these questions by collecting LA TAOS patterns on a hodge-podge of aerosols. In addition, some of the aerosols were collected on a microscope slide and viewed with a scanning electron microscope (SEM), so that the patterns could be correlated with a particle's structure. Finally, some simple quantitative features were extracted from the patterns using the Image Processing Toolbox of MATLAB®.

Using the LA TAOS experimental setup, the backward hemisphere of scattered light was collected. The IJAG system was utilized to generate aerosol particles with an approximate particle or cluster diameter of 8 μm. Fourteen different types of particles were examined: L-tryptophan (Sigma, lot# 127H0622), car soot (scraped from tailpipe), crushed tobacco leaves, bovine albumin (Sigma, lot# 44H0166), cluster of 0.2 μm PSL spheres (Duke Scientific, lot# 487475), cluster of 1.0 μm PSL spheres, cluster of 2.9 μm PSL spheres (Duke Scientific, lot# 6600), cigarette ash, kaolin, salt crystals (NaCl),

Arizona Test Dust, ammonium sulfate, riboflavin (Sigma, lot# 123H0800), and a cluster of BG spores.

To display the LA TAOS patterns as well as capture the variability from different particles of the same subset, three LA TAOS patterns of each particle type were selected. The first set of LA TAOS patterns of aggregate particles are shown in Figure 5-11. Refer to Section 2.1 for a discussion of the coordinate system of these patterns. The main features in these patterns appear to be island-like structures. From pattern to pattern, the islands vary in shape, size, density, and orientation. For the three PSL sphere cluster cases, the island density appears to be correlated to primary particle size. As the size of the primary particle increases, the island density increases and island size decreases.

The next set of aerosol particles shown in Figure 5-12 were selected based upon their sphere-like shape, as shown in the SEM images. The particles are not perfect spheres; in fact, most of the spheres are dimpled or cracked.[i] Again the island structures are quite evident in the patterns, where there is a large variability in the island shapes and density. For example, the majority of the islands in the LA TAOS pattern of crushed tobacco leaves are oblong and oriented along the lines of constant θ.

The LATAOS patterns of the remaining particles are shown in Figure 5-13. The LA TAOS patterns of two of the particles stand-out: soot and riboflavin. The pattern of the soot aerosol does not have the contrast ratio seen in the other patterns. This suggests that the soot particle is 'soft' in that its boundaries are not well defined (e.g. a fractal aggregate). The riboflavin particle has a rod-like shape which gives rise to a distinctive TAOS pattern with a bright line along two angles of ϕ separated by 180°. This scattering

[i] For a further discussions of why the IJAG generates cracked or dimpled spheres see subsection 4.3.3.

pattern can be understood with the diffraction theory where a slit give rise to a high intensity line in the plane perpendicular to the slit's direction.

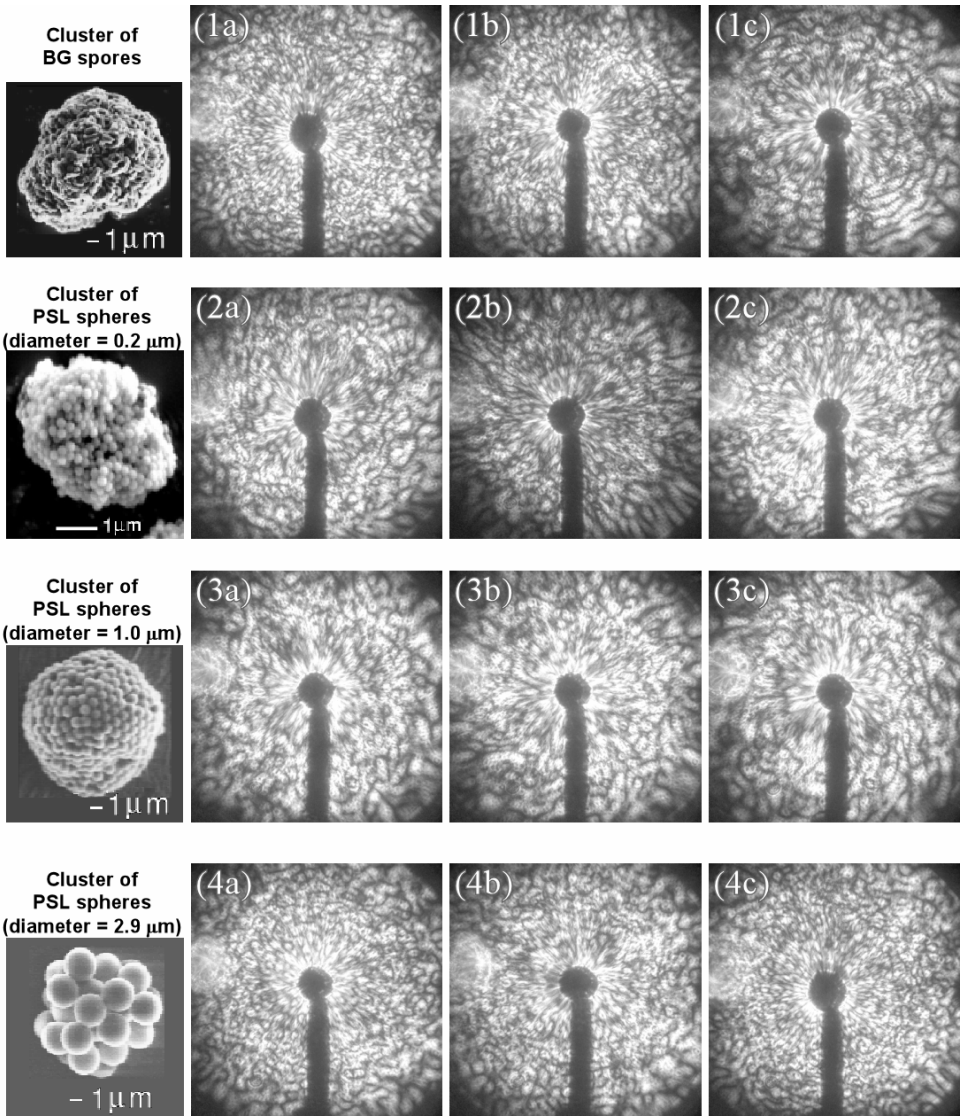

Figure 5-11: Representative LA TAOS patterns of the backward hemisphere of scattered light captured from clusters of BG spores (row 1) and PSL spheres (rows 2-4) as well as a typical SEM image of the generated aerosols.

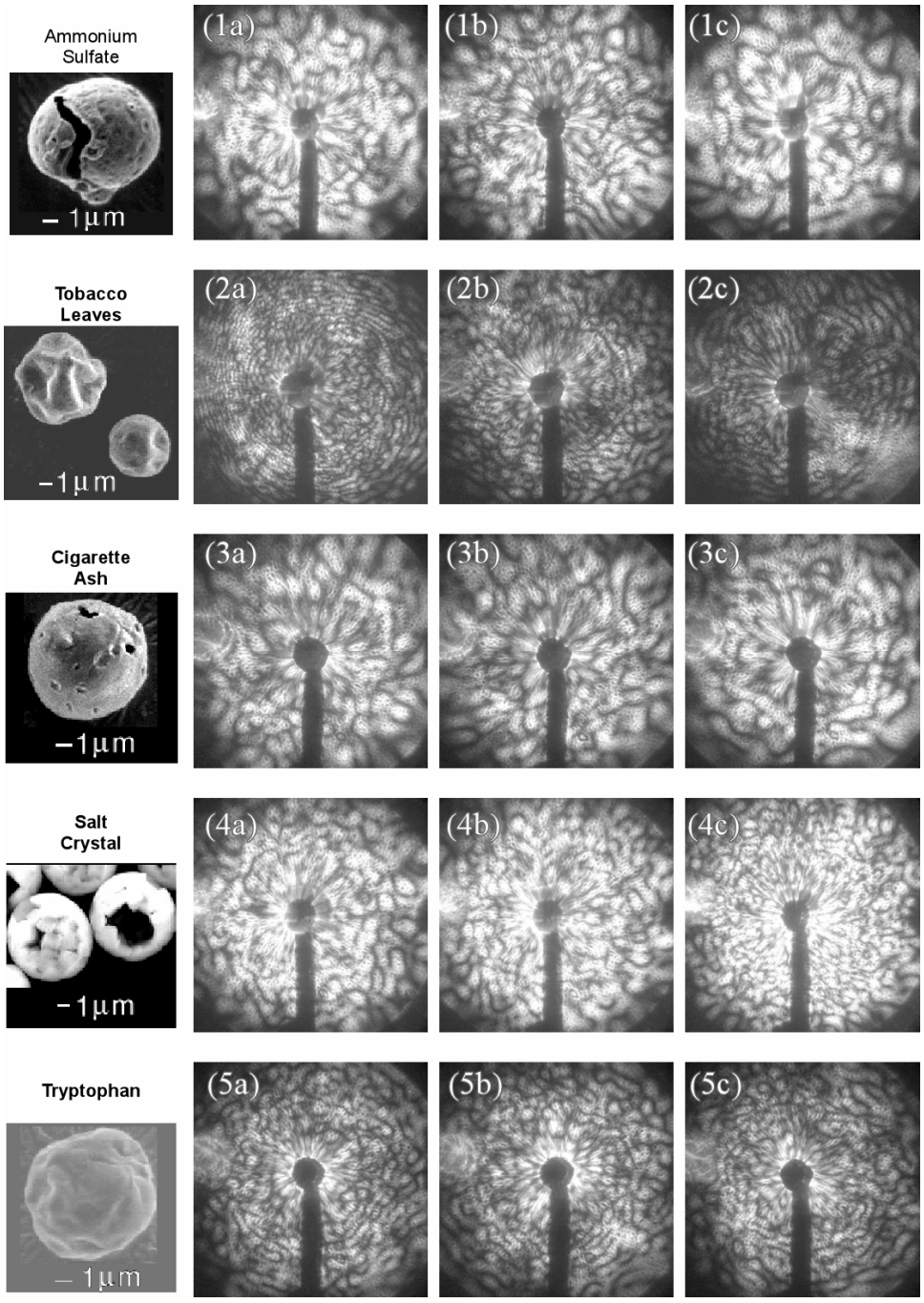

Figure 5-12: Representative LA TAOS patterns of the backward hemisphere of scattered light captured from various sphere-like aerosols as well as a typical SEM image of the generated aerosols.

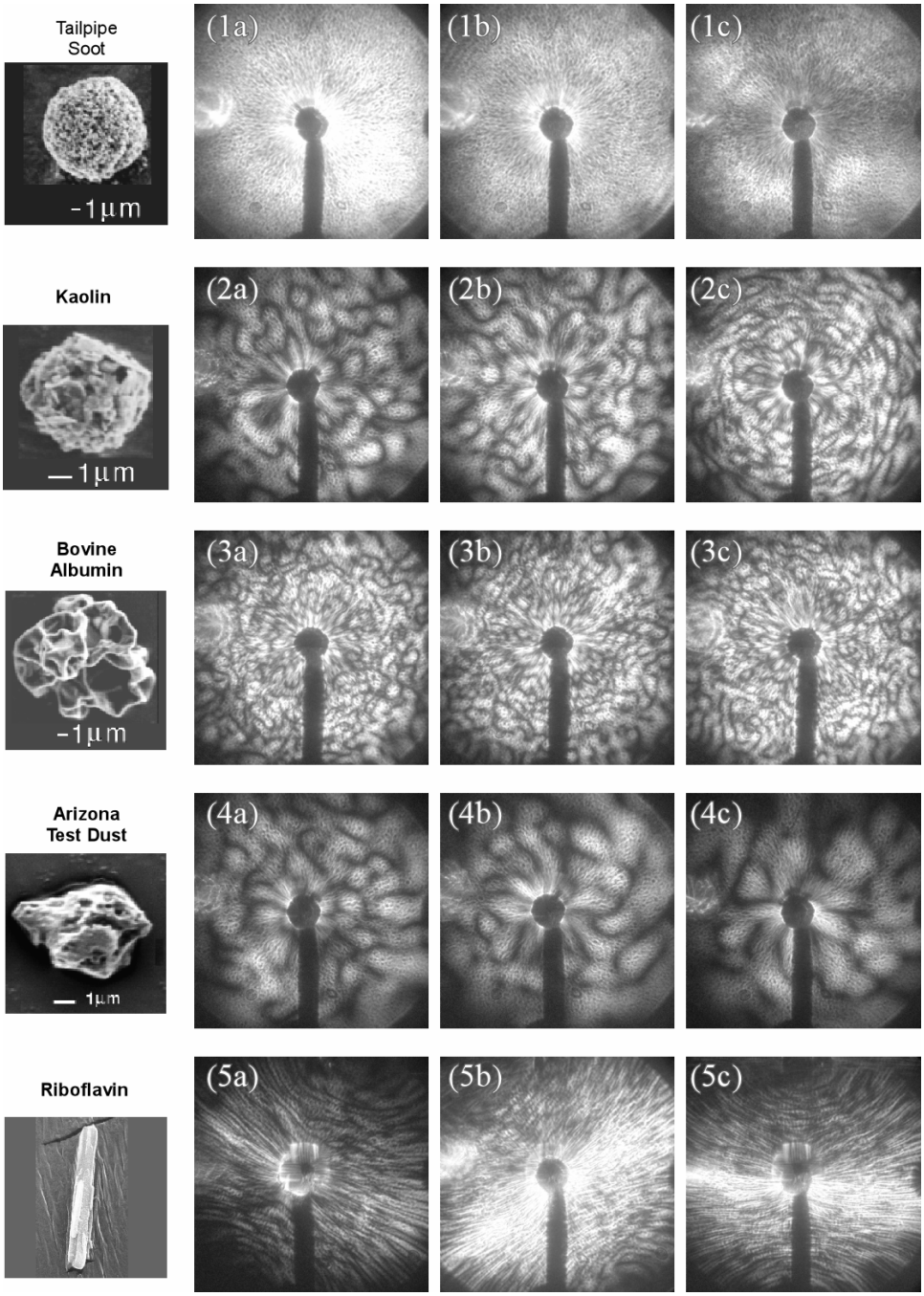

Figure 5-13: Representative LA TAOS patterns of the backward hemisphere of scattered light captured from various aerosols as well as a typical SEM image of the generated aerosols.

To extract quantitative features from the LA TAOS patterns, a program was written in MATLAB® that could trace-out the islands' profile and determine each island's area, orientation, and eccentricity, as well as the total number of islands found per pattern and the total intensity of the pattern.[59,60] The total intensity of the island gives a rough estimation of particle size since the scattering cross-section goes as the square of the radius.[5,6] Of course, this is only a rough approximation in addition it ignores the effects of absorption which would greatly alter the correlation between scattering-cross section and particle size. A flow-diagram of how the islands are found in the pattern is shown in Figure 5-14. There are a couple of key steps in this process that should be elaborated on. First, adjusting the gamma of the picture helps to bring out some of the low-light level features (step 3). Second, using a gradient routine to define the island perimeter mimics the eye since we notice contrast to define boundaries rather than absolute light level (step 6). Finally, islands should be ignored that are too close to a boundary since diffraction effects of the experimental setup could change their shape (step 9). In addition, the center of the image can be distorted, so this region was also ignored. Therefore, the mask generated to pass only the reliable regions extended from θ = 100° to 140°.

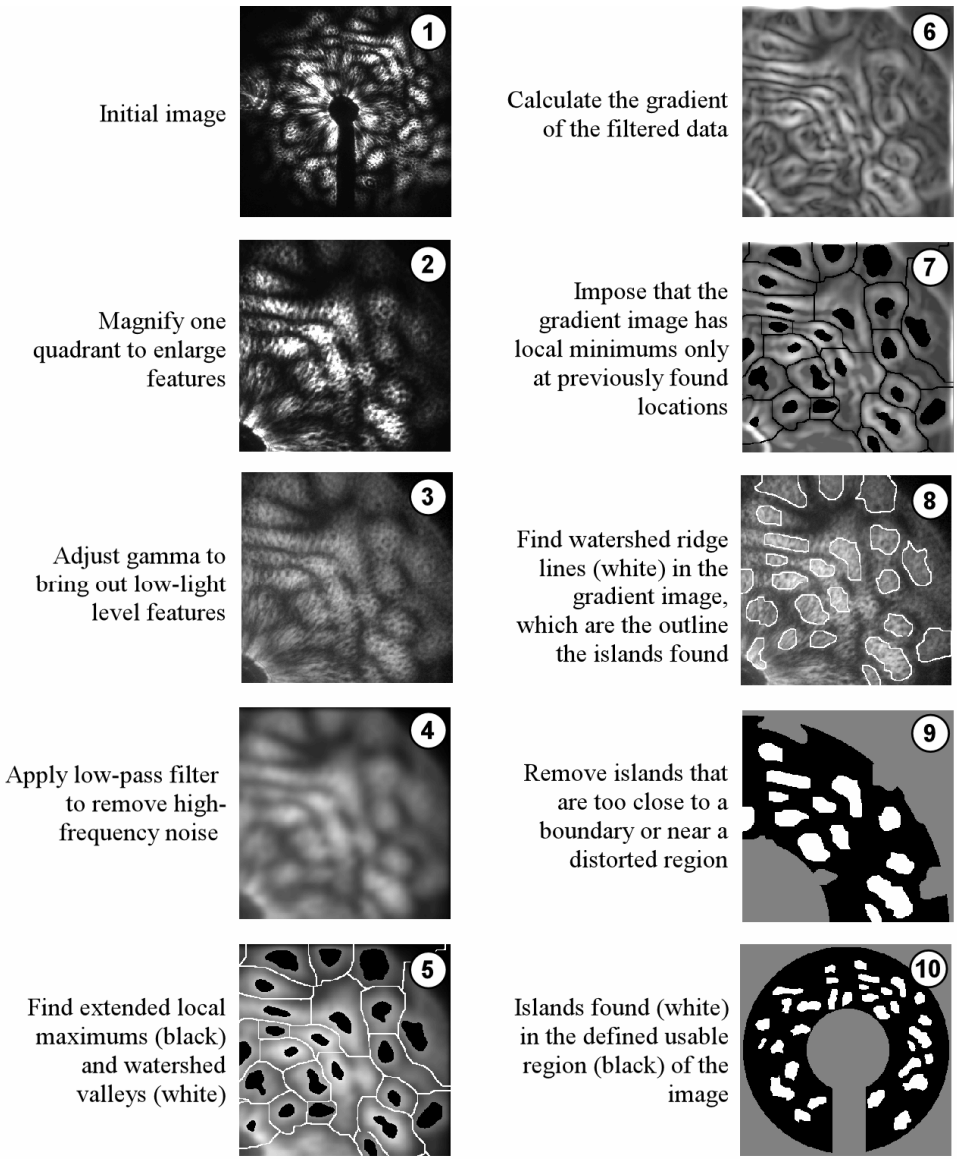

Figure 5-14: Flow-diagram of program to highlight island features in LA TAOS patterns.

For each island, three metrics were calculated: 1) island area, which is the number of pixels the island times the solid angle seen per pixel; 2) island orientation, which is the angle between the major axis of the island with respect to lines of constant ϕ (radial lines); and 3) island eccentricity, which can be calculated from the lengths of the major and minor axis. These are all outputs from the 'regionprops' function of MATLAB®. The metrics calculated are averaged over from each LA TAOS pattern. To average the

island orientation, the values were weighted by the eccentricity value of the island so that the orientation of a circular island is ignored. In addition, the number of islands found per pattern and the intensity summed over the defined usable region are recorded. The output from this program is summarized in Table 5-1.

Table 5-1: LA TAOS island metrics from a hodge-podge of particles.

Particle Type	Patterns Analyzed	Average Pattern		Average Island		
		Total Intensity (a.u.)	Number of Islands	Area (steradians)	Orientation (with respect to lines of constant ϕ)	Eccentricity
Cluster of BG Spores	16	45 ±18	90 ±12	0.019 ±0.002	46° ±5	0.71 ±0.01
PSL Spheres Cluster (d = 0.2 μm)	6	59 ±39	103 ±22	0.018 ±.0.005	45° ±9	0.73 ±0.03
PSL Spheres Cluster (d = 1.0 μm)	46	44 ±22	113 ±22	0.016 ±0.003	43° ±4	0.71 ±0.02
PSL Spheres Cluster (d = 2.9 μm)	34	47 ±35	123 ±28	0.015 ±0.006	46° ±4	0.70 ±0.01
Ammonium Sulfate	8	47 ±22	55 ±9	0.031 ±0.005	48° ±6	0.69 ±0.02
Tobacco Leaves	9	13 ±13	96 ±14	0.014 ±0.001	49° ±8	0.72 ±0.01
Cigarette Ash	12	27 ±15	58 ± 5	0.029 ±0.005	42° ±7	0.72 ±0.02
Salt Crystals	6	68 ±11	100 ±18	0.019 ±0.004	45° ±4	0.70 ±0.01
Tryptophan	46	15 ±10	104 ±12	0.015 ±0.002	53° ±5	0.71 ±0.02
Tailpipe Soot	13	69 ±29	35 ±28	0.043 ±0.019	43° ±15	0.76 ±0.03
Kaolin	9	29 ±16	50 ± 8	0.035 ±0.016	44° ±10	0.74 ±0.03
Bovine Albumin	34	26 ±11	110 ±9	0.015 ±0.002	46° ±5	0.71 ±0.01
Arizona Test Dust	11	9 ±1	33 ±8	0.043 ±0.007	45° ±7	0.71 ±0.02
Riboflavin	26	26 ±19	46 ±8	0.021 ±0.004	34° ±5	0.79 ±0.02

The tabulated data represents a first attempt at quantifying the LA TAOS patterns. Note the small number of patterns analyzed which should be greatly increased to improve upon statistical analysis. Even with the limited number of patterns analyzed, some interesting trends should be highlighted. Examining the number of islands found, there seem to be a correlation for the PSL clusters between the primary particle diameter and the number of islands. However, the standard deviation is too large to validate this correlation. A discriminating feature for riboflavin crystals, which have a rod like shape,

is the island orientation. Glancing at the LA TAOS patterns (Figure 5-13) the islands appear to be oriented radially along lines of constant ϕ unlike the other patterns for the other aerosols where the orientation appears to be more random. The data in Table 5-1 supports this finding where the average island orientation is 34°, which is 8° less than the next lowest value.

One of the key questions of this work is whether one can distinguish a cluster BG spores (a simulant for Anthrax) from other aerosols. Examining the metrics in Table 5-1 for BG clusters from PSL sphere clusters (d = 1 μm), which has a similar cluster size and primary particle size, there does not appear to be a distinguishing feature. The number of islands in the pattern is perhaps the best way to differentiate the two, but note that the standard deviation is quite large. Of course, in the real world, one is not posed with the problem of identifying a cluster of BG spores from a cluster of PSL spheres, but rather discriminating between a cluster of BG spores and the aerosols particles commonly found in the ambient environment. It is this thinking as well as a general curiosity about the LA TAOS patterns of the atmospheric particles that led to the research effort in the next section.

5.2.3 - LA TAOS Patterns of Particles in the Ambient Atmosphere

To detect the LA TAOS patterns of ambient aerosols, a replica LA TAOS setup was built at the U.S. Army Research Labs in Adelphi, MD (Latitude 39° 01' N, Longitude 76° 57' W) to utilize the outdoor sampling equipment that Dr. Ronald G. Pinnick has built into his lab. Further discussion of this setup can be found in Subsection 4.3.1. The ambient data was collected overnight starting at 3 pm on October 6th, 2004 and ending at 9 am on October 7th, 2004. The temperature ranged from a high of 64° (3

pm on the 6th) to a low of 43° (6 am on the 7th).[61] The patterns were collected over an eighteen hour period. The number of patterns detected per hour is displayed in Figure 5-15.

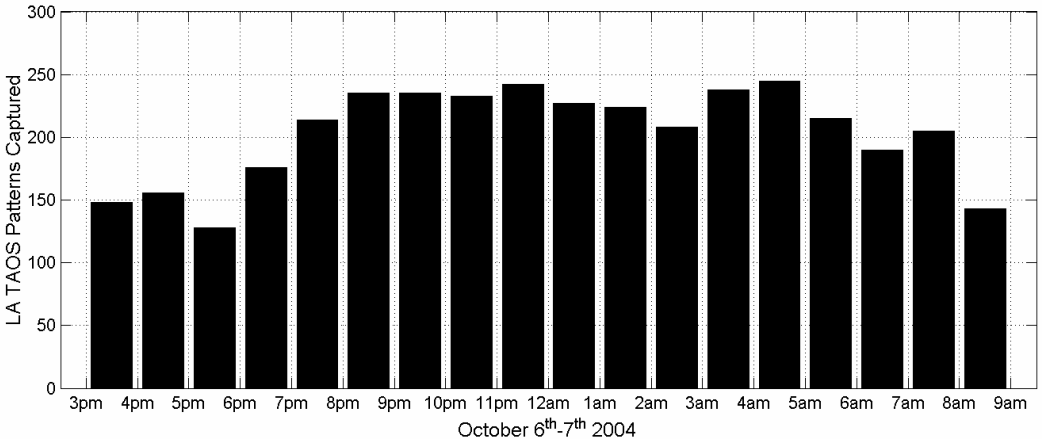

Figure 5-15: Hourly number of LA TAOS patterns detected of ambient aerosols.

The laser source for this experiment was a Spectra Physics X-30 which has a 30 nsec pulse length unlike the 70 nsec pulse width of the Y-70 used in the previous experiments. Both lasers are at a short enough time scale that the scattering pattern should be equivalent. The cross-beam trigger system was used to minimize the aberration coma in the system. Unlike the previous data where only the backward hemisphere of scattered light was detected, in this experiment, some of the forward hemisphere of light is also detected. Thus the holes in the ellipsoidal mirror at θ equals 90° are apparent in the LA TAOS image. The collected angle range is approximately θ from 75° to 130°, with ϕ ranging from 0° to 360°. In addition, the laser polarization was rotated 45° from the previous experiments. Therefore, in the following patterns, the line representing the light scattered in the plane perpendicular to the polarization of the incident beam goes from the southeast corner of the image to the northwest corner of the image. The patterns

shown are not corrected for the nonlinear mapping of a three-dimensional scattering space to the two dimensional detector plane. Thus the images have a slight pincushion distortion.

The LA TAOS patterns collected were quite diverse. To get a sense of the variability of the ambient aerosol LA TAOS patterns, the first 20 patterns capture are displayed in Figure 5-16. There are several experimental artifacts embedded in the TAOS patterns. The dark circles on the four sides of the image are due to the holes in the ellipsoidal mirror. The vertical bar at the bottom of the image is the shadow of the beam block mount. The artifacts seen at the center of the image are due to both the holes in the back of the ellipsoidal mirror as well as some stray light. These regions are ignored for all of the image analysis in this chapter.

From previously captured patterns, one expects spherical particles to have ring-like features (see Figure 5-9). This stems from Lorenz-Mie theory where it is shown that the scattering intensity is

$$I(\theta,\phi) = I_{para}(\theta)\sin^2(\phi) \quad + \quad I_{perp}(\theta)\cos^2(\phi), \tag{5-1}$$

where is $I_{para}(\theta)$ is the scattering intensity in the plane defined by the polarization and the propagation wavevector of the incident beam, and $I_{perp}(\theta)$ is the scattering plane perpendicular to the incident beam's polarization. Therefore, for a fixed θ, the variation in intensity along ϕ will be a smoothly varying function either monotonically increasing or decreasing from $I_{para}(\theta)$ to $I_{perp}(\theta)$. In Figure 5-16, patterns 3 and 10 have ring like features suggesting a spherical particle shape. Pattern 14 also has a ring-like structure

although not as symmetric. It is the determination of this symmetry (or degree of symmetry, Dsym) that is discussed in the following subsection.

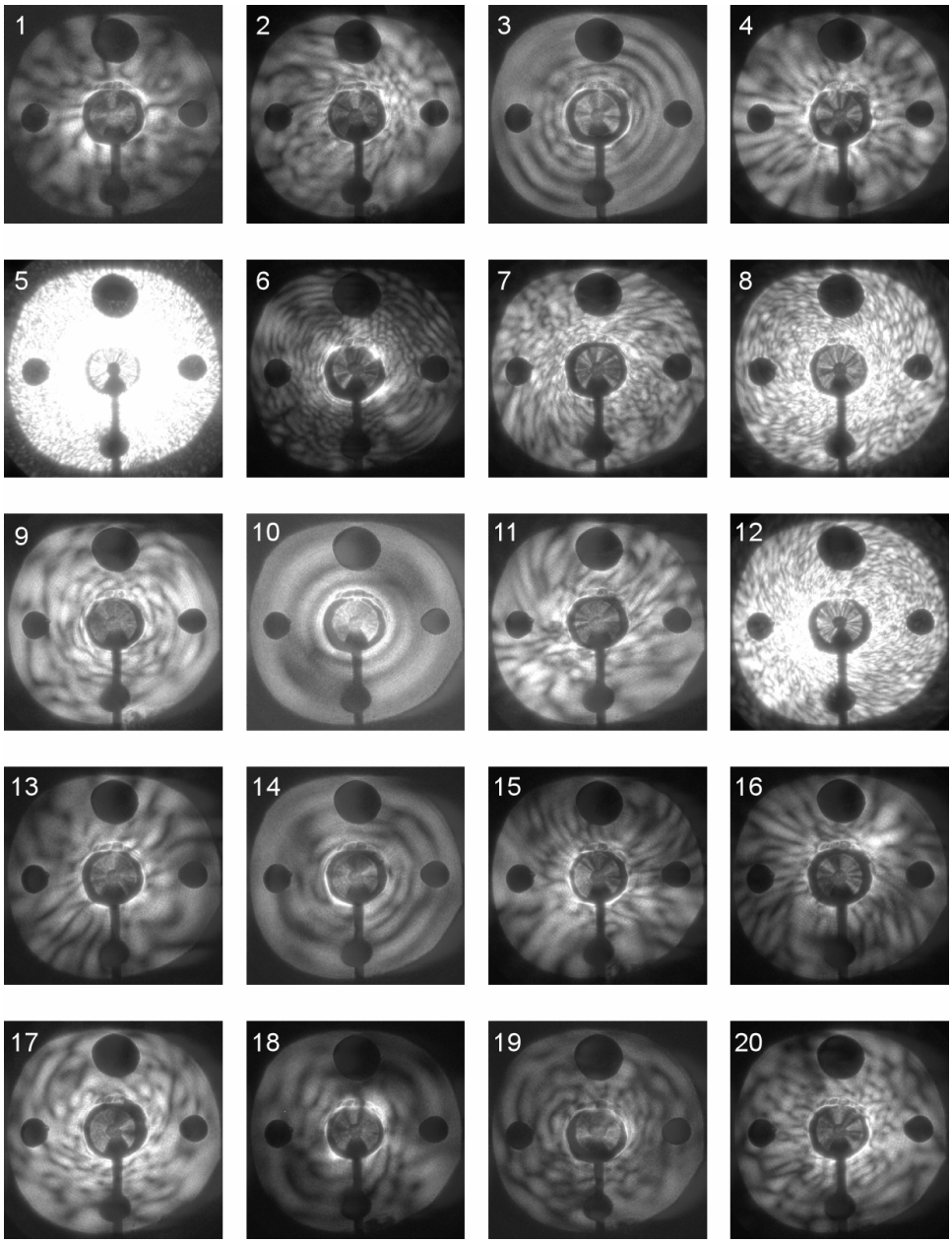

Figure 5-16: The first twenty LA TAOS patterns captured of ambient aerosols.

5.2.3.1 - Degree of Symmetry

One way to characterize the ambient aerosols is by examining the symmetry of the scattering pattern. This approach has been taken by a multitude of groups over the years in one form or another. Gucker *et al.* looked at the mirror symmetry of a one-dimensional slice of data taken in a fixed scattering plane to determine if a spherical particle was well aligned.[28] Kaye *et al.* used three detectors at the same scattering angle (θ) but at three different azimuthal angles (ϕ = 0°, 120°, and 240°) to determine if circularly polarized input light was scattered symmetrically. To quantify the asymmetry of the scattered light, they introduced an *asymmetry factor* (*Af*), based upon the relative magnitudes of the three detector signals. *Af* is determined by

$$Af = \frac{\sqrt{(\overline{E} - E1)^2 + (\overline{E} - E2)^2 + (\overline{E} - E3)^2}}{\overline{E}} \times 40.81, \qquad (5\text{-}2)$$

where *E1, E2,* and *E3* and the magnitudes of the outputs of the detector channels 1, 2, and 3, respectively, and $\overline{E}$ = *(E1+E2+E3)*/3. The factor 40.81 is a scaling multiplier such that the absolute range of *Af* is 100. Thus for spherical particle *E1 = E2 = E3*, then *Af* = 0; and for a long fiber aligned axially with the airflow would give *E1 = E3* = 0 and *E2* = some size dependent positive value, then *Af* = 100.

Dick *et al.* used a commercially available system, the DAWN-A (Wyatt Technology Corp.), to measure a *sphericity index* (SPX) of ambient aerosols.[37,38] This quantity is essentially 1.0 minus a normalized standard deviation of the pulse heights measured at eight evenly spaced azimuthal angles (ϕ) at a fixed scattering angle (θ). Thus, for a given scattering event, the *sphericity index* is

$$SPX = 1 - \frac{\left[\sum_{i-1}^{8} (m_i - \overline{m})^2\right]^{1/2}}{7 \times \overline{m}}, \tag{5-3}$$

where m_i is the response of the i^{th} detector and $\overline{m}$ is the mean of the eight detector values. Sampling ambient particles in the 0.2 – 0.8 μm size range, Dick found that <10% of the particles were non-spherical.

To analyze the symmetry of the LA TAOS patterns, where the incident beam is linearly polarized rather than circularly polarized, we rely on a new gauge. This gauge is called the Degree of Symmetry and is expressed as

$$Dsym = 1 - \sum_{pixel\ subset} abs\left[\frac{I^N(\theta,\phi) - I^N(\theta,\phi+180°)}{2}\right], \tag{5-4}$$

where *abs* stands for absolute value and $I^N(\theta,\phi)$ is the normalized single pixel intensity value at angle (θ,ϕ). For a spherical particle, two pixels that have the same scattering angle θ but have ϕ values that are offset by 180° should have the same intensity resulting in a Dsym value of 1. In addition, if the aerosol has a rotation of symmetry axis that is pointed either parallel or perpendicular to the incident polarization, the scattering pattern will also have a 180° rotational symmetry, again resulting in a Dsym value of 1. In Figure 5-17, the normalization process as well as the matrix manipulation to determine Dsym is demonstrated.

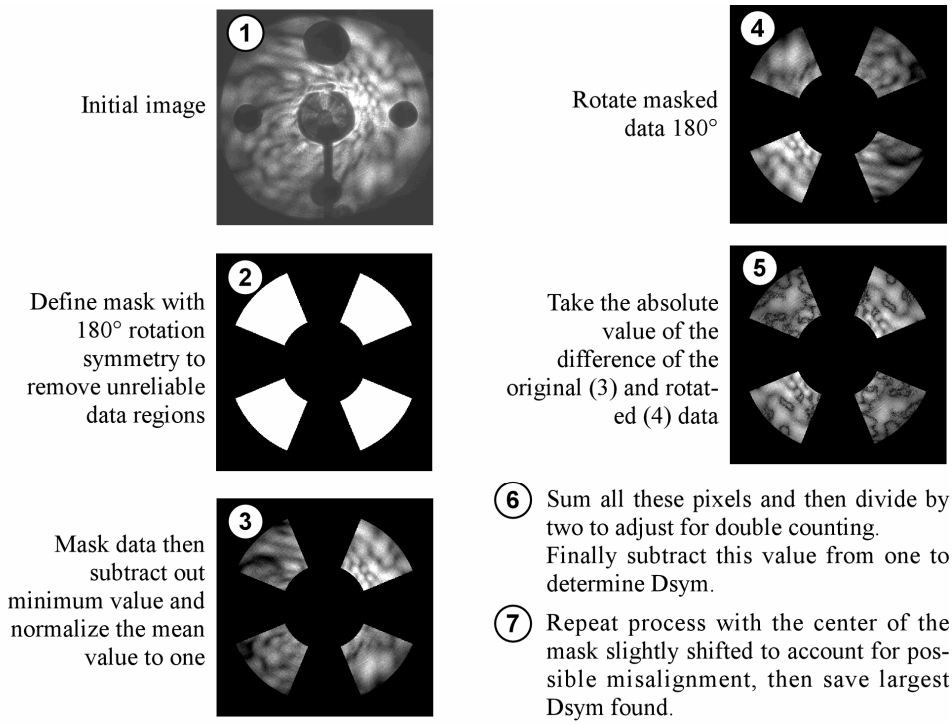

Figure 5-17: Flow-diagram of program to determine Dsym of LA TAOS patterns.

The Dsym calculated for the first twenty LA TAOS patterns are shown in Figure 5-18. As expected, patterns 3 and 10 have high Dsym values. Note that pattern 5 has a high value also, although this is due to the intensity saturation of the picture. The pattern with the lowest Dsym value is number 16 where the upper right corner of the pattern is particularly bright. This asymmetric feature leads to the large Dsym value. Not also that although pattern 14 has rings it does not have a high Dsym factor since the rings are not symmetric.

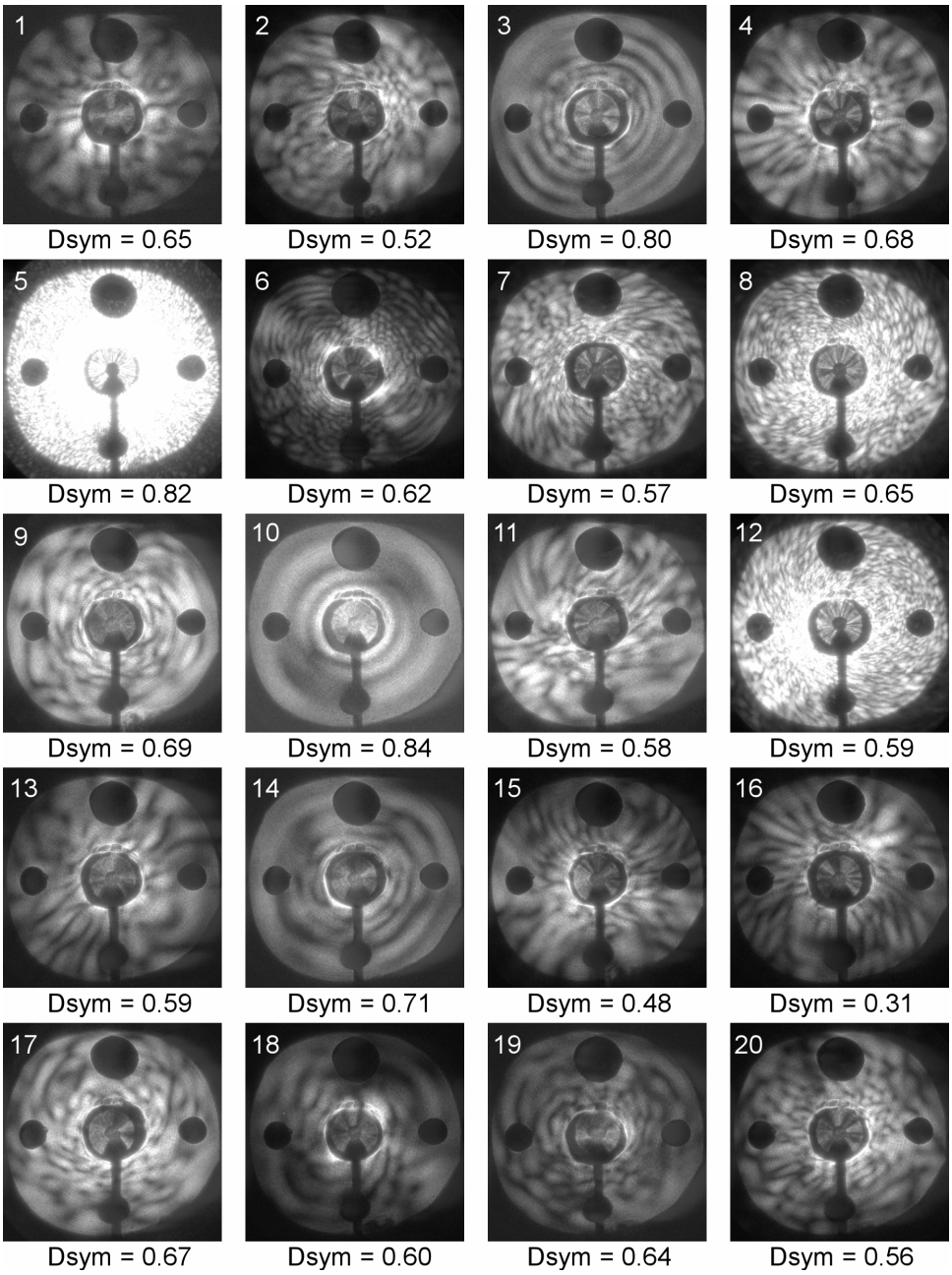

Figure 5-18: Calculated Dsym values for select ambient LA TAOS patterns.

Dsym was calculated for the entire data set of ambient particles (5993 patterns). In addition, using the identical LA TAOS setup but with a Royco aerosol generator (see Subsection 4.3.5), data sets were also collected of single PSL spheres (39 patterns), single or small clusters of *Bacillus subtilis* spores (97 patterns), and droplets of dioctyl phthalate

(200 patterns). Finally, LA TAOS patterns of the particulate matter in diesel exhaust was collected (288 patterns) and Dsym was calculated for each pattern. In addition to Dsym, the mean number of photoelectron events per pixel (MPE) was determined for each LA TAOS pattern. This should roughly correlate to the aerosol's diameter since the scattering cross-section goes as the radius squared. A plot of Dsym versus MPE is shown in Figure 5-19 for the different data sets. Only LA TAOS patterns with a MPE mean of more than 2 and less than 1000 were included in the plot. In addition, different datasets were collected with different gain settings on the ICCD detector, however the data was corrected for these different settings with specification supplied by Andor Technology, the detector's manufacturer.

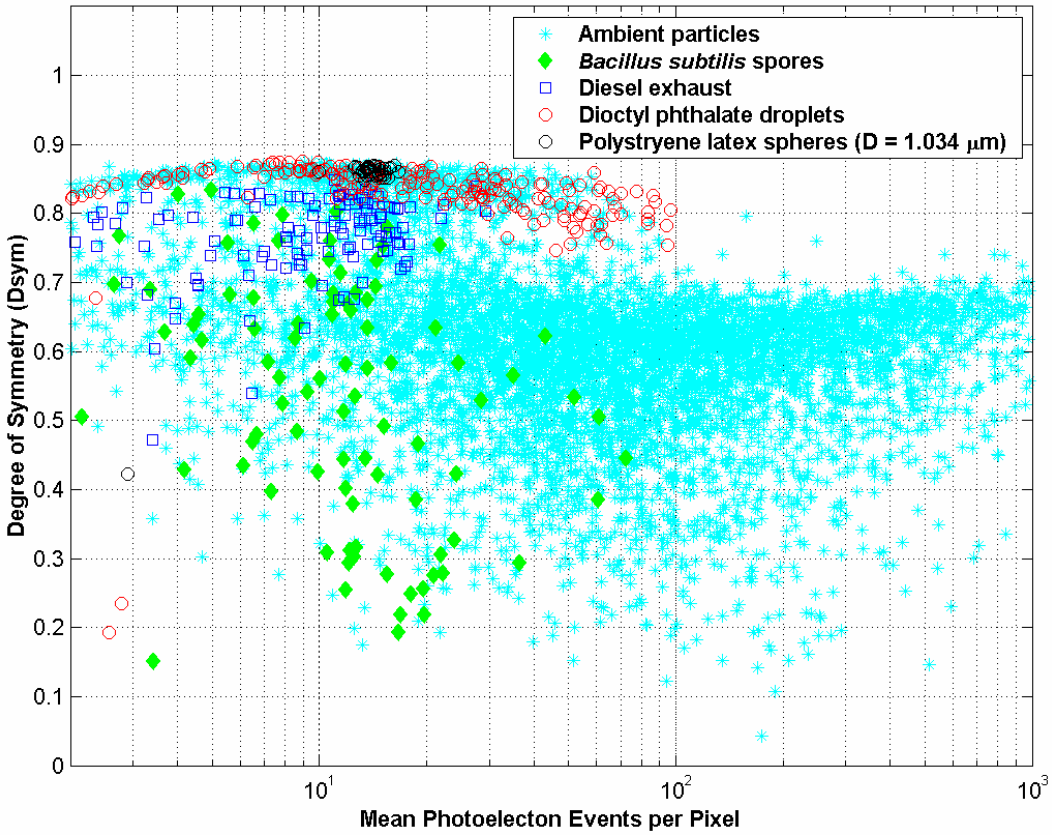

Figure 5-19: Degree of Symmetry (Dsym) versus the mean number of photoelectron events per pixel for various aerosols.

Apparent in the plot is a ceiling at the Dsym value of 0.9. This ceiling is an experimental artifact and is due to slight distortions in the mirror surface (see Subsection 4.1.3). The Dsym of the Polystrene Latex (PSL) spheres are range from 0.85 to 0.87 with one exception, a data point at Dsym = 0.42 and MPE = 2.9. After examining the scattering pattern of this particle, it is believed that the particle was either a piece of dust or residue from the Royco aerosol generator. In addition, the MPE narrowly bound between 9.5 and 15.9 again ignoring the one outlying point. The confinement of the Dsym and MPE values to these narrow bounds is to be expected since the spheres are fairly homogenous having a diameter of 1.034 ± 0.05 μm.

The next particle type to consider is dioctyl phthalate, which are droplets of various diameters but the same refractive index of 1.485. The droplets will be extremely spherical since the surface area to volume ratio is quite large, thus surface tension will drive the droplets shape rather than gravity. Thus, one would expect the LA TAOS patterns to have a high Dsym. This is supported by the experimental findings where the Dsym values are all above 0.75 if some of the low intensity patterns, where the particles are most likely dust or residue from the Royco, are ignored. Note also the roll-off in Dsym for higher MPE values. There are two reasons for this effect. First, larger intensity values correlate to larger spheres that result in LA TAOS patterns with a higher spatial frequency of ring structure. Slight distortion in the LA TAOS patterns will cause some of these rings not to overlap in calculating Dsym. Second, larger droplets lead to a slightly larger focal volume since a larger particle can be farther away from the center of focus of the trigger beams but still scatter enough light to trigger the system. A larger focal volume will of course lead to more distortion in the LA TAOS image reducing the Dsym

value. The slight roll-off in Dsym for lower values of MPE is due to a reduction of the signal-to-noise level as the scattering cross-section is reduced.

The particulate matter in diesel exhaust appears to be slightly spherical with a majority of the Dsym values lying above 0.70 with a maximum value of 0.85. This was somewhat surprising since it is well known that the soot in Diesel exhaust is composed of fractal aggregates made up of tiny ~30 nm carbonaceous spheroids.[62] This topic is revisited in Subsection 5.2.3.2.

The results from single BG spores and small clusters of BG spores are less surprising, where the Dsym values are scattered from 0.15 to 0.83. A single BG spore can be approximated as having pill-shape. Note that the scattering pattern from a pill-shaped particle can still have a fairly high Dsym. This is depicted in Figure 5-20 where an experimentally captured LA TAOS patterns (Dsym = 0.68 and 0.80) is compared with numerical simulations (see Section 2.4) performed by Dr. Jean-Claude Auger. The large variability in both the shapes of single BG spores and their orientations with respect to the incident beam will lead to various LA TAOS patterns, some with more symmetry than others. In addition, some of the particles might be clusters of two or three BG spores that will most certainly lead to LA TAOS patterns with a low Dsym.

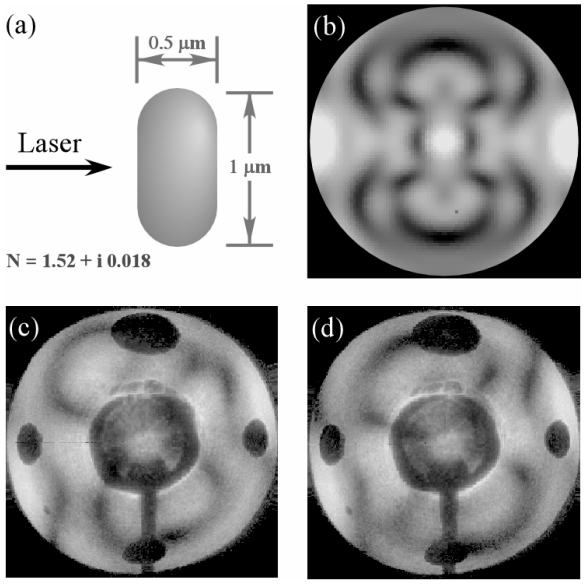

Figure 5-20: Scattering pattern from a single BG spore: (a) estimated spore dimensions, (b) numerical simulation, (c) and (d) experimental results.

Finally, the LA TAOS patterns of ambient aerosols are distributed over Dsym values ranging from 0.4 to 0.88. Bulk of the values are centered around a Dsym value of 0.60, however there appears to be another clustering of LA TAOS patterns in the 0.8 to 0.9 range, which most likely represents spherical particles. To see this clustering, a histogram of the LA TAOS patterns which fall in different Dsym ranges is displayed in Figure 5-21.

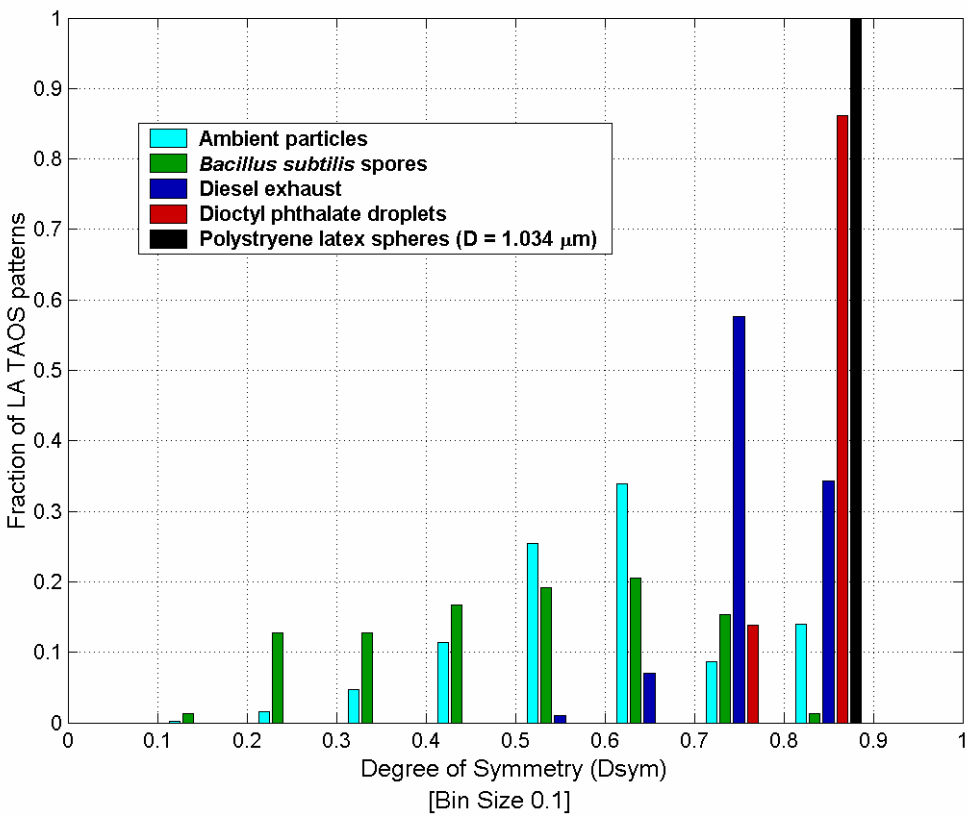

Figure 5-21: Histogram of concentrations of particles in different Dsym ranges for different particle types.

Only patterns with a MPE greater than 5 but less than 100 were included in the histogram. The higher threshold value was selected since the LA TAOS patterns of dioctyl phthalate reached that MPE value and thus the program can reliably pick-out spheres up to that value. The lower threshold was selected for the pattern to have an adequate signal-to-noise ratio. One can estimate the particle diameter range of this intensity span by counting the number of rings in the dioctyl phthalate LA TAOS pattern at the two intensity extremes and using the estimate that the number of rings in the LA TAOS patterns the scattering plane ($\theta = 0°$ to $180°$) is approximately kR, where $k = 2\pi/\lambda$ and R is the sphere radius.[57] Using this approach, the diameters of the particles are in the 0.6 to 5 μm range.

As expected, all of the PSL spheres fell between a Dsym value of 0.8 and 0.9. A majority (~ 86%) of the dioctyl phthalate droplets also fell into this bin, where as all the droplets had a Dsym value above 0.7. The particulate matter in diesel exhaust was concentrated in the 0.7 to 0.8 bin although there were a considerable number of particle with a Dsym in the 0.8 to 0.9 bin. These results suggest that the particles are quite sphere-like. The Dsym values of single BG spores were fairly uniformly spread over the range from 0.2 to 0.8 with a slight peak in the 0.6 to 0.7 bin. Unlike all the other datasets, the ambient data set appears to have two peaks, one in the bin from 0.6 to 0.7 and another in the bin from 0.8 to 0.9. This implies that the ambient particles can be divided into two categories, a non-spherical class and a spherical class. The ambient data is plotted with a much finer bin scale, as shown in Figure 5-22, and a Dsym value of 0.77 is determined to be the threshold level. With this division, 84% of the particles would be classified as non-spherical and 16% of the particles would be classified as spherical.

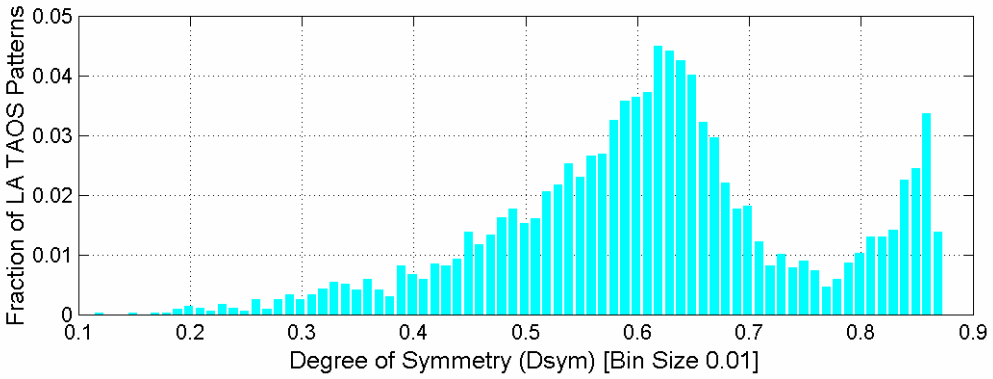

Figure 5-22: Histogram of the Dsym values of ambient particles at a finer resolution.

The LA TAOS images of the ambient particles were time-stamped so that transient effects could be explored. In particular, if there are noticeable difference in the aerosol morphology due to rush hour traffic. To determine if the concentration of

spherical particles changed over time, the hourly number of particles with Dsym values over 0.77 was counted. A plot of the results are shown in Figure 5-23 where, over the 18 hours of collected data, there does not appear to be any sort of trend.

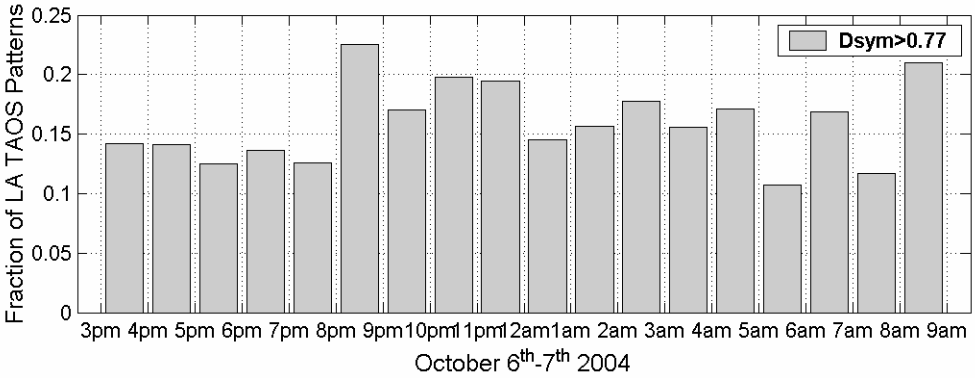

Figure 5-23: Hourly changes in Degree of Symmetry (Dsym) over an 18 hour span.

5.2.3.2 - Extracting the Refractive Index of Spherical Particles

Since a number of the ambient particles are spherical, one could extract information about the refractive index and the radius by comparing these patterns to Lorenz-Mie theory. This is not a new approach, for example a *flow-through* system designed by Gucker (see Figure 3-1) was capable of measuring the refractive index of PSL spheres to within 0.7% and the radius to within 0.5% by comparing the light scattering in a single scattering plane to Lorenz-Mie theory.[34]

A program was written in Matlab where a radius and refractive index were varied and for each case a *goodness-of-fit* or merit function was calculated. The merit function was defined as

$$\chi^2 = \frac{1}{N} \sum_{n\ angles} \left(\frac{I_{\exp}(\theta_n) - I_{theory}(\theta_n)}{\sigma(\theta_n)} \right)^2, \qquad (5\text{-}5)$$

where $I_{exp}(\theta_n)$ is the experimental intensity value and $I_{theory}(\theta_n)$ is the intensity value based on Lorenz-Mie theory at a angle θ_n, $\sigma(\theta_n)$ is the estimated standard deviation at that angle, and N is the total number of angles compared. A smaller value of χ^2 is therefore a better fit to the data. Fifty angles equally distributed between 81° and 128° were selected for comparison. In addition, a slice of data along the perpendicular scattering plane and the parallel scattering plane were analyzed resulting in a total of one hundred angles compared. The experimental data was binned over approximately 4 pixels to filter out the higher noise. Note that 1/N factor that is typically not found in the merit function. This factor is to remove the dependence of χ^2 on the number of data points examined.

Three factors were accounted for to estimate $\sigma(\theta_n)$. The first factor stems from the detection of the scattered photons which follows Poisson statistics. This is approximately the square-root of the number of incident photons. The second component is the shot-noise from the dark current which again goes as the square-root of the dark-current counts. The third source of noise is the fluctuations in intensity due to distortions in the mirror. This was found to be quite large, approximately 35% of the scattered intensity.

Scattering curves in the parallel and perpendicular direction were generated using Lorenz-Mie theory for a sphere of radius 0.52 μm and refractive index 1.60. These two curves were analyzed by the χ^2 program; the output is shown in Figure 5-24. Plot (a) shows the input curves. Plot (b) is a three-dimensional plot of the χ^2 function over the radius and refractive index parameters space. One might expect a delta function, however the binning of intensity data mentioned above smoothes the input data resulting in a slightly distorted curves. A peak is apparent in the plot, but the parameter values are

more easily identified if the data is shown as a contour plot as in (c), which show that the program successfully found the radius and refractive index.

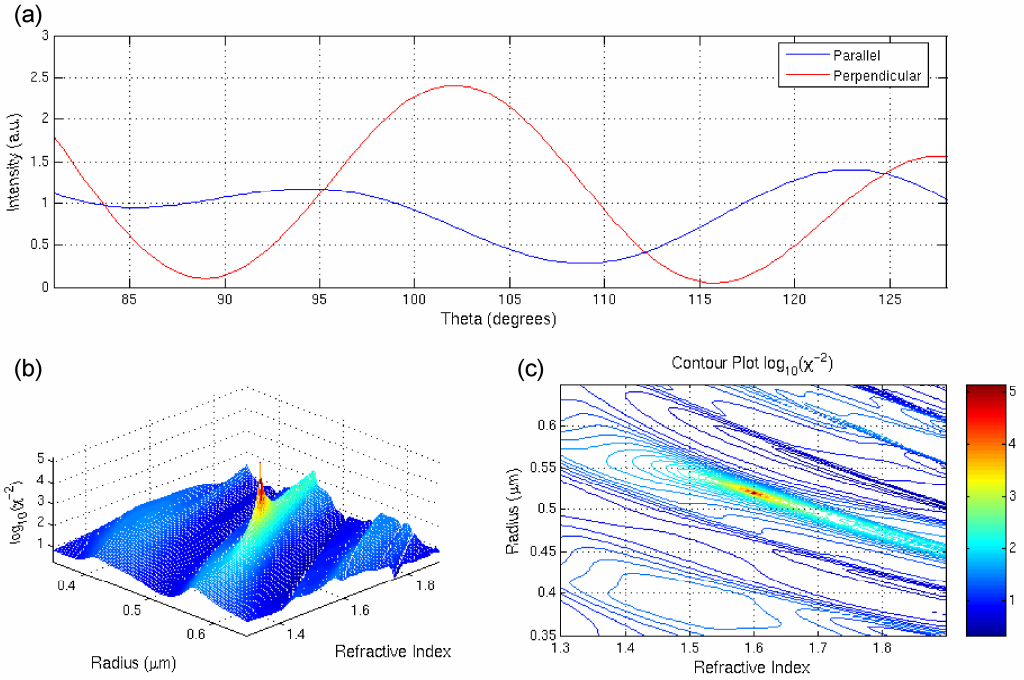

Figure 5-24: Output of curve-matching program with artificial input. Plot (a) is the input curve generated with Lorenz-Mie theory. Plots (b) and (c) show the $\log(1/\chi^2)$ over refractive index and radius.

The approach above was repeated with some Gaussian noise added to the input curve to simulate the noisy experimental data. The results are shown in Figure 5-25, where again the peak occurred at the appropriate radius and refractive index value. Note however that the peak value decreased and broadened. In addition, it is apparent in plot (c) that the radius and the refractive index are well correlated. This does not come as a surprise since Kerker showed that scattering efficiency of a sphere was fairly constant if the phase shift,

$$\rho = 2kR(n-1), \tag{5-6}$$

remained constant, where $k = 2\pi/\lambda$, R is the sphere radius, and n is the refractive index.[6]

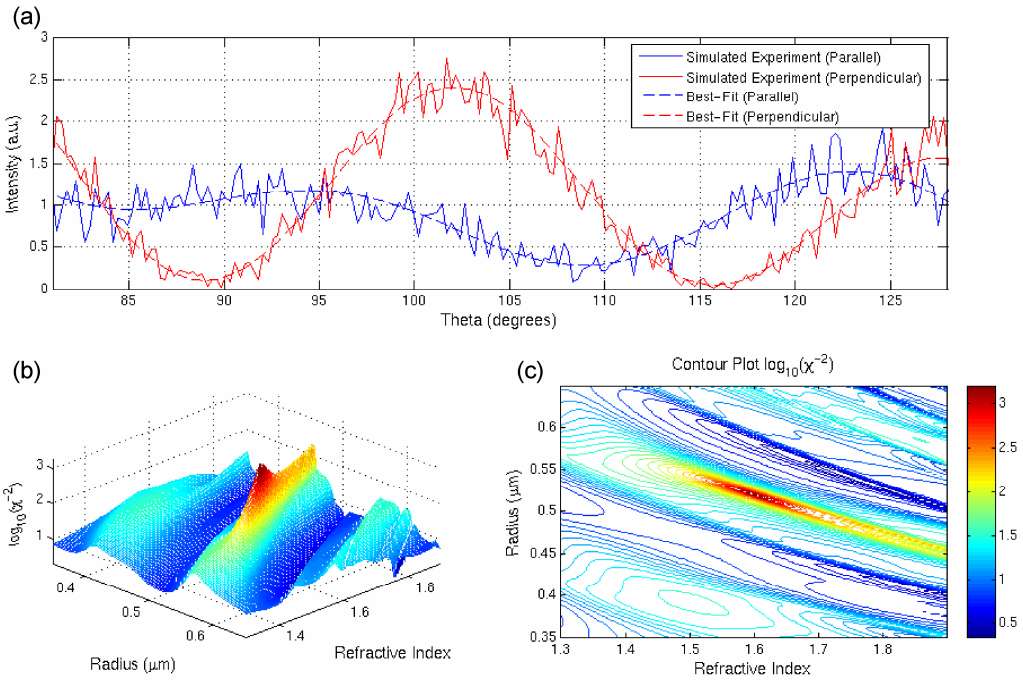

Figure 5-25: Same as Figure 5-24 but with added Gaussian noise on the input curve.

When experimental data was processed by the χ^2 program, errors stemmed from a lack of knowledge of the exact angles values. As discussed in Subsection 4.1.3, the inaccuracy in the identifying the angle θ can be as large as 2.5°. To alleviate this problem, the program was allowed to search over both a θ shift factor and a θ scale factor. The success of this addition is shown in Figure 5-26 where a LA TAOS pattern of a PSL sphere (n = 1.598, radius = 0.517 ± 0.025) is analyzed. The best-fit occurred at n equal to 1.606 and the radius equal to 0.522 μm with a θ shift of -2° (shifted to lower values) and a θ scale of 0.95 (slightly compressed). Note that the peak is quite low where the χ^2 value of approximately 3, which corresponds to the data being on average 3σ away from the best-fit value.[63]

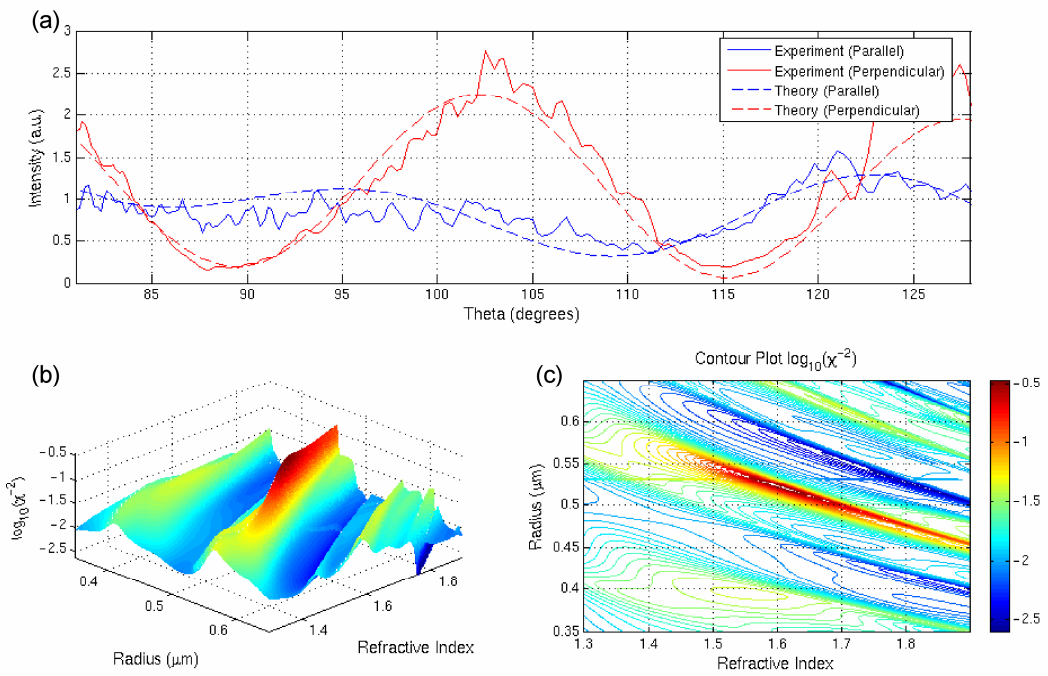

Figure 5-26: Output of curve-matching program for a polystyrene latex sphere (n = 1.598, radius = 0.517 ± 0.025). The best-fit occurred at n = 1.606 and radius = 0.522 μm.

To increase the overall speed of the index-search program, the Levenberg-Marquardt algorithm routine was utilized.[63] The Levenberg-Marquardt algorithm is an efficient search routine for nonlinear least-squares fitting since it is both a gradient search routine as well as an analytical first-order expansion method. Examining the contour space of $1/\chi^2$, it is apparent that there are local minima throughout the parameter space. Thus, for different initial values of the refractive index and the radius, the program could find different best-fit values. To combat this, a multitude of starting point values distributed evenly over the search space were used where the refractive index starting values ranged from 1.2 to 1.9 with a spacing of 0.1 and the radius starting values ranged from 0.3 μm to 2 μm with a spacing of 0.05 μm. In addition, the program searched of the complex part of the refractive index (κ) with three starting values, 0.0, 0.05, and 0.1.

The LA TAOS patterns of polystyrene latex spheres (PSL), dioctyl phthalate droplets (DOP), particulate matter in diesel exhaust, and ambient aerosol were analyzed. The data was filtered with the criteria shown in Table 5-2. The best-fit refractive index and radius for the different subsets are plotted in Figure 5-27. The intersection of the x-gridlines and y-gridlines represent the set of initial values used as the starting point of the search algorithm.

Table 5-2: Criteria for analyzing the LA TAOS patterns of spherical particles.

Property	Lower Limit	Upper Limit
Dsym value	0.77	None
χ^2	None	7.5
Mean Photoelectron Events per Pixel	5	100
Radius	0.31 μm	1.89 μm
Refractive Index	1.25	1.85

The index of refraction of polystyrene and DOP is known and thus can be used to determine the accuracy and the precision of this analysis. The found index of refraction for the PSL spheres was 1.597 ± 0.009 whereas the known refractive index of polystyrene is 1.598. For this case, all the spheres had the same radius ($0.517\ \mu m \pm 0.025\ \mu m$) whereas the measured radius was $0.524\ \mu m \pm 0.002\ \mu m$. These results match well with the precision stated by Marshall *et al.* who tested Gucker's instrument (see Figure 3-1) on PSL spheres.[34]

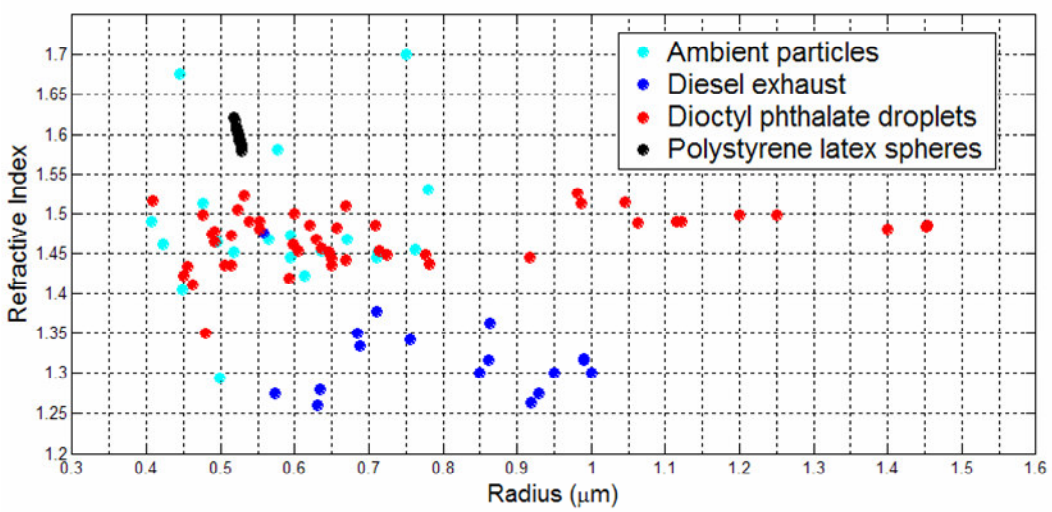

Figure 5-27: Best-fit using least-squares of refractive index and radius for spherical particles from various data sets.

In addition, further analysis of the PSL data set depicts the limiting factor of this technique. As shown in Figure 5-28, the radius (R) and the refractive index (n) are strongly correlated variables. Indeed, for a given scattering pattern there appears to be a range of the n and R values that fit well with the data and lie along line. As shown in the plot, this line appears to be well described by keeping $(n-1) \times R^3$ constant, suggesting that spheres with similar *optical* volumes will have similar scattering patterns over small ranges of n and R. However, further analysis is needed to confirm this finding.

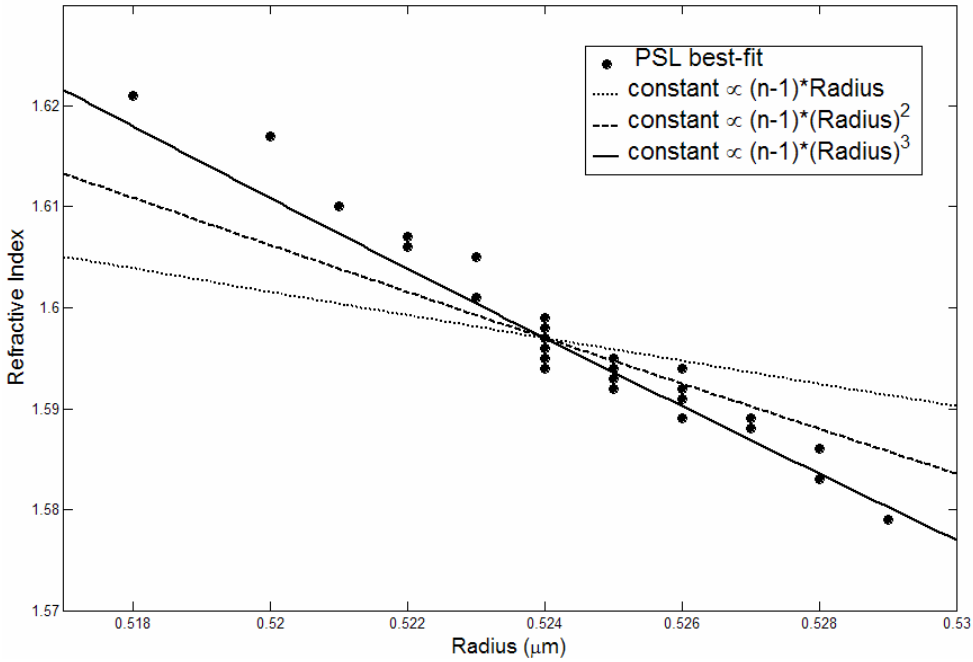

Figure 5-28: Plot of the best-fit refractive index and radius values for thirty-eight polystyrene latex spheres. In addition, three lines are plotted representing three different possible constants.

Although the refractive index of the DOP droplets (n = 1.483) should remain the constant, the radius of the droplets will vary since they were generated using the ROYCO aerosol generator. The LA TAOS patterns of 44 DOP droplets were analyzed resulting in a mean refractive index of 1.47 with standard deviations from the mean of $\sigma = 0.03$, although σ appears to vary with radius. Since we wish to use this σ value to project the precision that we can measure the refractive index of ambient particles, the radius range should be limited to mirror that of the ambient particle, $0.4\ \mu m < R < 0.8\mu m$. Over this range, 32 LA TAOS patterns were analyzed resulting in a mean refractive index of 1.46 with $\sigma = 0.04$.

With this limited level of precision and accuracy, one can still interpret broad trends. For example, analyzing 17 ambient aerosol patterns, the mean index of refraction

is 1.49 with $\sigma = 0.08$ and a single pattern resulted in a refractive index less than 1.4. On the other hand, of the 16 patterns analyzed of particulate matter in diesel exhaust, only one resulted in a refractive index above 1.4, where the mean was 1.32 with $\sigma = 0.05$. The refractive index value of 1.32 for diesel exhaust is suspiciously close to that of water (n = 1.33) suggesting perhaps that water vapor is condensing during the 4 minute transit time and the twenty minute release time to form water droplets. On the other hand, the mean refractive index of the ambient aerosols is 2σ from the refractive index of water.

A summary of the values stated through-out this section is presented in Table 5-3. Little discussion has been given to the imaginary component of the refractive index (κ) that gives rise to absorption. However, this parameter was also searched for using least-squares analysis. The mean value for κ found for each particle type was quite low, less than 0.008. However, the standard deviations around these mean values were large making it difficult to interpret the data.

Table 5-3: Summary of optical properties from spherical aerosols.

Particle Type	Patterns Analyzed	Refractive Index			
		Real Component		Imaginary Component	
		Mean	Standard Deviation	Mean	Standard Deviation
Polystyrene Latex Spheres	38 out of 39	1.597	0.009	0.000	0.000
Dioctyl Phthalate	44 out of 200	1.47	0.03	0.002	0.008
Dioctyl Phthalate (reduced size range)	32 out of 200	1.46	0.04	0.003	0.010
Diesel Exhaust	16 out of 288	1.32	0.05	0.008	0.022
Ambient Aerosols	17 out of 5993	1.49	0.08	0.005	0.012

5.2.4 - Discriminating between *Bacillus Subtilis* Spores and Ambient Particles

One of the main thrusts of this work is to determine whether or not one can distinguish a cluster of *Bacillus subtilis* (BG) spores from a diverse background of particles found in the ambient atmosphere. To this end, LA TAOS patterns of 7000 ambient particles and 2000 powder-dispersed (Collision Generator) BG clusters were collected. The experimental setup to collect these patterns was identical to the one used in the previous section accept the laser was polarized vertically rather than at a 45° angle. These patterns were handed off to Dr. Judith Dayhoff, a pattern recognition expert, who plans to apply feature extraction algorithms to the patterns and use the resulting metrics to train a neural network to discriminate between the LA TAOS pattern of a BG cluster and the LA TAOS pattern of ambient atmospheric particles. Thus far, this has proven to be a formidable task. Dr. Dayhoff has found a single feature extraction algorithm that that can identify 60% of the BG cluster, however feeding the algorithm the ambient data leads to a false-positive rate of 50%. To get a sense of the difficulty in distinguishing these patterns, LA TAOS patterns of powder dispersed BG spores are shown in Row A of Figure 5-29 along with patterns collected from ambient particles, Row B. The LA TAOS patterns of ambient particle were chosen by eye from a collection of 7000 patterns as closely resembling the LA TAOS pattern of a BG spore cluster.

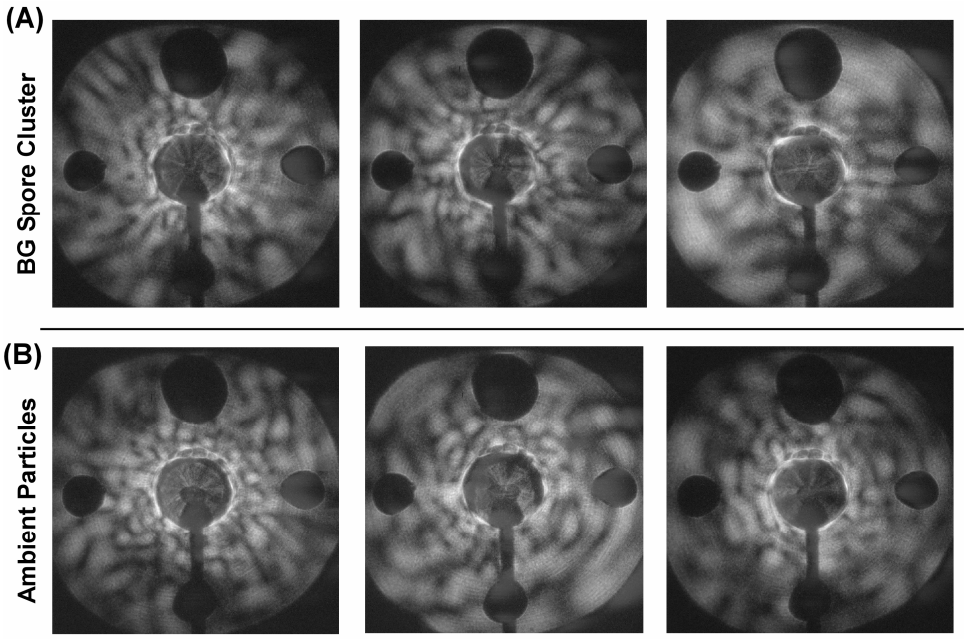

Figure 5-29: In Row A are LA TAOS patterns collected from clusters of BG spores. In Row B are LA TAOS patterns collected from ambient aerosols that could trigger a false alarm.

To quantify the similarities between the LA TAOS patterns of BG spores and those of ambient particles, both data sets analyzed using the island feature program discussed in Subsection 5.2.2 (see Figure 5-14). The one change made to the program was to adjust the "defined usable region" to account for the dark black holes in the image. Recall the previous patterns were over a smaller angle range that stopped short of these holes. The main gist of this program is to outline the islands features in the LA TAOS patterns and calculate some statistics on their average number of islands per pattern as well as the average island area, orientation, and eccentricity. The patterns were pre-filtered based upon their mean photoelectron events per pixel (MPE) to eliminate lower intensity patterns with few island features. In addition, as has been discussed previously, the particle size can lead to major changes in the LA TAOS patterns. Therefore, to investigate the possible fluctuations in the island statistics due to size, the data sets were

further subdivided according to their MPE value which should roughly correlate to size. The output from the program is shown in Table 5-4 where the bold lines are the statistics calculated from particles spanning the largest range of MPE values.

Table 5-4: LA TAOS island metrics from powder dispersed BG spores and ambient atmosphere particles.

Particle Type	MPE Range	Patterns Analyzed	Average Number of Islands	Area (steradians)	Average Island Orientation (with respect to lines of constant ϕ)	Eccentricity
Cluster of BG Spores	20 – 25	131	34 ± 13	0.027 ± 0.009	41° ± 12°	0.74 ± 0.04
Cluster of BG Spores	25 – 30	112	40 ± 15	0.024 ± 0.009	40° ± 15°	0.75 ± 0.04
Cluster of BG Spores	30 – 35	98	43 ± 16	0.022 ± 0.007	41° ± 11°	0.74 ± 0.04
Cluster of BG Spores	35 – 40	50	45 ± 14	0.021 ± 0.006	40° ± 15°	0.75 ± 0.03
Cluster of BG Spores	**20 – 40**	**391**	**39 ± 15**	**0.024 ± 0.008**	**41° ± 11°**	**0.74 ± 0.04**
Ambient Particles	20 – 25	541	37 ± 21	0.024 ± 0.010	52° ± 16°	0.77 ± 0.06
Ambient Particles	25 – 30	295	40 ± 21	0.022 ± 0.010	50° ± 17°	0.77 ± 0.06
Ambient Particles	30 – 35	303	44 ± 23	0.021 ± 0.010	49° ± 15°	0.77 ± 0.06
Ambient Particles	35 – 40	264	50 ± 24	0.018 ± 0.009	48° ± 15°	0.77 ± 0.05
Ambient Particles	**20 – 40**	**1503**	**42 ± 23**	**0.022 ± 0.010**	**50° ± 16°**	**0.77 ± 0.06**

Before comparing the ambient island statistics with those processed from clusters of BG spores, note that certain island feature seem to correlate with MPE, as was found in Subsection 5.2.2. In particular, the island number increased and island area decreased with increasing MPE value suggesting that larger particles lead to LA TAOS patterns with a higher density of smaller islands. Comparing the BG spore cluster data to the ambient particle data, no island feature is separated by more than a standard deviation. The best feature to discriminate between the two particle classes seems to be island orientation. To determine the extent in which this metric can discriminate between ambient particles and clusters of BG spores, a *distinction function* was calculated. As defined by Sachweh *et al.*, the distinction function is

$$D(ANG) = \frac{C_1(ANG)}{C_1(ANG) + (1 - C_2(ANG))}, \tag{5-7}$$

where C_1 and C_2 are the cumulative distribution functions as a function of ANG and ANG is the average island orientation angle (C_1, C_2, and D are shown in Figure 5-30). To balance the rate of false positives with false negatives, D is chosen to have a value of 0.5, which corresponds here to ANG = 42.5°. At this threshold level, for particles that fell into the appropriate MPE range, 64% of the BG clusters would be identified as such and 36% of the ambient particle would be misidentified as BG clusters.

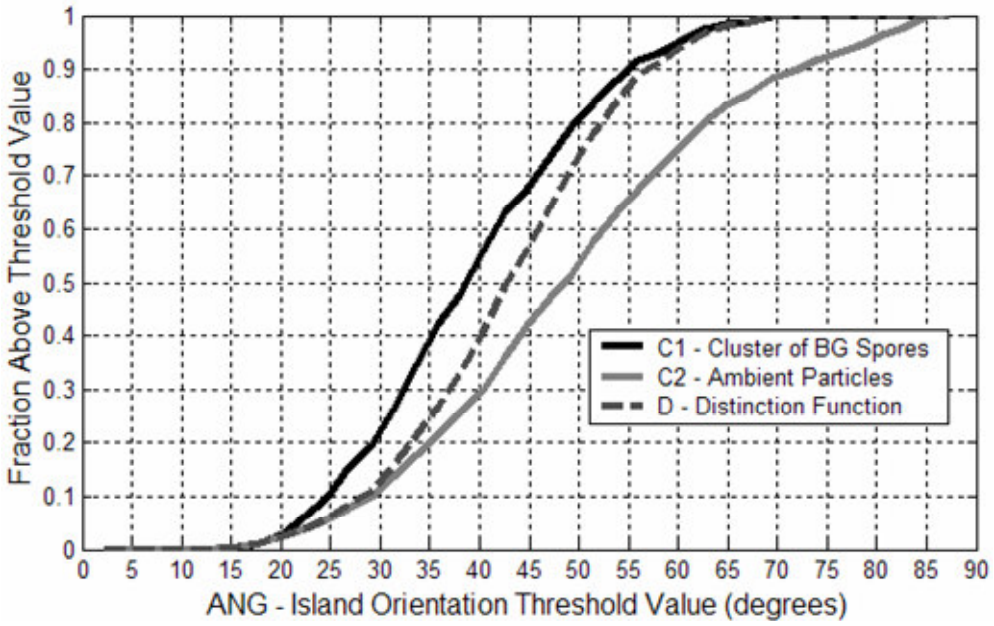

Figure 5-30: Illustration of the *distinction function* used to determine threshold value to discriminate between clusters of BG spores and ambient atmosphere particles.

Chapter 6: Conclusion

The LA TAOS system designed and built for this thesis collects elastic scattering from single particles over a large angle range *in-situ* and in real-time. The configuration of the device utilized a cross-beam trigger system to minimize the effects of the aberration coma stemming from the main collection optic, the ellipsoidal mirror. The defined *trigger volume* of $(25\ \mu m)^3$ still led to distortions in the LA TAOS patterns, where angles could be mislabeled by as much as 2.5° as predicted by an exact ray-trace analysis. However, this level of distortion is a vast improvement over previous designs found in the literature where the scattering volume was only limited by the diameter of the particle-laden airflow through the system.

A series of experiments were run to measure single particle absorption. These experiments were conducted in both visible wavelength regime (532 nm) and in the mid-infrared (3-5 μm). A novel experimental setup for collecting simultaneous LA TAOS patterns at two wavelengths was designed and implemented. With this setup, the LA TAOS patterns of droplets composed of a mixture of H_2O and D_2O were detected. By choosing the two incident wavelengths to be on and off an absorption band of D_2O one could easily identify droplets composed with at least 25% D_2O. This experiment provides a framework in which single-particle absorption spectra could be collected over a multitude of wavelengths.

One of the main thrusts of this work was to determine the viability of the LA TAOS technique to distinguish harmful aerosols, such as anthrax, from the plethora of benign aerosols in the ambient atmosphere. To this end, 21,000 LA TAOS patterns of

ambient aerosols were collected as well as 2,000 patterns of powder dispersed *Bacillus subtilis* spores, a simulant for anthrax. These patterns were turned over to a pattern recognition expert, who thus far has produced inconclusive results. In addition, a feature extraction program was written to generate statistics on the island-like features commonly seen in the LA TAOS patterns. No metric was found that could highly discriminate between the powder dispersed BG spores and the ambient aerosols. However, the island orientation seemed to be loosely correlated to the source of the particle. The average island orientation in the LA TAOS patterns for powder dispersed BG spores was found to be 41° ± 11° with respect to lines of constant ϕ, whereas for ambient aerosols this value was 50° ± 16°. Choosing the angle 42.5° as a threshold level would correctly identify 64% of the BG patterns as suspicious but incorrectly identify 36% of the patterns generated from ambient particles as suspicious. From these results, it seems unlikely that the LA TAOS technique could be developed into a stand-alone bio-warfare sensor. However, it could be utilized as a complementary technique to other sensor technologies.

The Degree of Symmetry (Dsym) metric was presented in this work to characterize the LA TAOS patterns of ambient aerosols. Approximately 15% of the ambient aerosol particles generated a LA TAOS pattern with a Dsym value greater than 0.77. These particles are typically spheres, where a perfect sphere, with an aberration free and noise free collection system, would correlate to a Dsym value of 1.0. Slices along the parallel and perpendicular scattering planes from these patterns were fit to Lorenz-Mie theory using least-squares to define the merit function and a Levenberg-Marquardt optimization program to search the radius refractive index parameter space.

The refractive index values of the patterns analyzed appeared to cluster in the range 1.4 to 1.6. Indeed, the mean value was n = 1.49 with a standard deviation around this mean of σ = 0.08.

The central question of this thesis was whether elastic light scattering can be used to discriminate between bio/chemical warfare agents and the diverse and large concentration of benign ambient particles. The results of this thesis suggest that the specificity of the LA TAOS technique is not high enough to warrant a stand-alone system. However, it is unlikely that any single technique will be able to reduce the false-alarm rate to an acceptable level. Thus, the next question that needs to be answered is whether elastic light scattering can be used as a complimentary technique to laser-induced fluorescence (LIF), the current technology used for early-warning systems, to greatly improve the false-positive rate. In particular, it must be determined what particles lead to false-positives for each technique. If they are distinct subsets, then combining the techniques should greatly minimize the number of false-positives.

In addition to determining what subsets of particles produce false-positives in the LIF and elastic light scattering systems, other issues remain which require further exploration. For example, in this thesis some initial analysis was performed on the scattering patterns that were experimentally collected. However, the physics that explains these scattering patterns was only briefly explored. In particular, the patterns were primarily analyzed in real-space, whereas perhaps k-space would reveal more information. Future experiments should attempt to simplify the problem, perhaps by looking at small clusters of spherical particles, to explore this link. I believe such

experiments will also shed light on what laser wavelength and angle range are most suitable for a particular goal.

Finally, a single application was pursued in this Thesis, detection of bio/chemical warfare agents. However, as we scan the horizon of the future, it is quite conceivable that other technologies will demand a diagnostic tool that can analyze small particles *in-situ* and in real-time. For example, the analysis of airborne particulates helps to provide insight into the atmospheric chemistry that determines the ultimate fate of pollutants. Thus as air pollution continues to grow as a concern for our society, the demand for diagnostic tools to analyze the particulate composition will also grow. In addition, there is currently a push in the field of nanotechnology to develop airborne 'nanorobots'. Undoubtedly, if nanorobots do come into fruition, there will be a demand for a technology to detect these man-made particles and perhaps this is where LA TAOS will find its greatest utility.

References

1. Y. L. Pan, K. B. Aptowicz, R. K. Chang et al., "Characterizing and monitoring respiratory aerosols by light scattering," Opt Lett **28** (8), 589-591 (2003).

2. Y. L. Pan, S. Holler, R. K. Chang et al., "Single-shot fluorescence spectra of individual micrometer-sized bioaerosols illuminated by a 351- or a 266-nm ultraviolet laser," Opt Lett **24** (2), 116-118 (1999).

3. R. Casagrande, "Technology against terror," Sci Am **287** (4), 82-87 (2002).

4. P. H. Kaye, K. AlexanderBuckley, E. Hirst et al., "A real-time monitoring system for airborne particle shape and size analysis," J Geophys Res-Atmos **101** (D14), 19215-19221 (1996).

5. Craig F. Bohren and Donald R. Huffman, *Absorption and scattering of light by small particles*. (Wiley, New York, 1983).

6. Milton Kerker, *The scattering of light and other electromagnetic radiation*. (Academic Press, New York, 1969).

7. H. C. van de Hulst, *Light scattering by small particles*. (Wiley, New York,, 1957).

8. Michael I. Mishchenko, Larry D. Travis, and Andrew A. Lacis, *Scattering, absorption, and emission of light by small particles*. (Cambridge University Press, Cambridge, UK ; New York, 2002).

9. Max Born and Emil Wolf, *Principles of optics : Electromagnetic theory of propagation, interference and diffraction of light*, 7th (expanded) ed. (Cambridge University Press, Cambridge ; New York, 1999).

10. C. M. Sorensen, "Light scattering by fractal aggregates: A review," Aerosol Sci Tech **35** (2), 648-687 (2001).

11. P. H. Kaye, E. Hirst, J. M. Clark et al., "Airborne particle-shape and size classification from spatial light-scattering profiles," J Aerosol Sci **23** (6), 597-611 (1992).

12. Michael I. Mishchenko, Joop W. Hovenier, and Larry D. Travis, *Light scattering by nonspherical particles : Theory, measurements, and applications*. (Academic Press, San Diego, 2000).

13. S. Holler, J. C. Auger, B. Stout et al., "Observations and calculations of light scattering from clusters of spheres," Appl Optics **39** (36), 6873-6887 (2000).

14. S. C. Hill and P. W. Barber, *Light scattering by particles: Computational methods*. (World Scientific Company, Inc., Singapore, 1990).

15. P. J. Wyatt, "Scattering of electromagnetic plane waves from inhomogeneous spherically symmetric objects," Phys Rev **127** (5), 1837-& (1962).

16. C. S. Kim and C. Yeh, "Scattering of an obliquely incident wave by a multilayered elliptic lossy dielectric cylinder," Radio Sci **26** (5), 1165-1176 (1991).

17. T. Oguchi, "Scattering properties of oblate raindrops and cross polarization of radio waves due to rain: Calculations at 19.3 and 34.8 ghz," J. Radiat. Res. Lab. **20**, 79-118 (1973).

18. S. Asano and G. Yamamoto, "Light-scattering by a spheroidal particle," Appl Optics **14** (1), 29-49 (1975).

19. T. Onaka, "Light scattering by spheroidal grains," Ann. Tokyo Astron. Obs. **18**, 962-974 (1980).

20. P. C. Waterman, "Matrix formulation of electromagnetic scattering," Pr Inst Electr Elect **53** (8), 805-812 (1965).

21. P. C. Waterman, "Symmetry, unitarity, and geometry in electromagnetic scattering," Phys Rev D **3** (4), 825-& (1971).

22. F. T. Gucker, C. T. Okonski, H. B. Pickard et al., "A photoelectronic counter for colloidal particles," J Am Chem Soc **69** (10), 2422-2431 (1947).

23. F. T. Gucker, H. B. Pickard, and C. T. Okonski, "A photoelectric instrument for comparing the concentrations of very dilute aerosols, and measuring low light intensities," J Am Chem Soc **69** (2), 429-438 (1947).

24. F. T. Gucker and J. J. Egan, "Measurement of angular variation of light scattered from single aerosol droplets," J Coll Sci Imp U Tok **16** (1), 68-& (1961).

25. F. T. Gucker and R. L. Rowell, "The angular variation of light scattered by single dioctyl phthalate aerosol droplets," Discuss Faraday Soc (30), 185-& (1960).

26. D. T. Phillips, P. J. Wyatt, and R. M. Berkman, "Measurement of lorenz-mie scattering of a single particle - polystyrene latex," J Colloid Interf Sci **34** (1), 159-& (1970).

27. P. J. Wyatt, "Light-scattering in microbial world," J Colloid Interf Sci **39** (3), 479-& (1972).

28. F. T. Gucker, J. Tuma, H. M. Lin et al., "Rapid measurement of light-scattering diagrams from single aerosol particles in an aerosol stream and determination of the latex particle size," Aerosol Science **4**, 389-404 (1973).

29. M. Bartholdi, G. C. Salzman, R. D. Hiebert et al., "Differential light-scattering photometer for rapid analysis of single particles in flow," Appl Optics **19** (10), 1573-1581 (1980).

30. P. J. Wyatt, K. L. Schehrer, S. D. Phillips et al., "Aerosol-particle analyzer," Appl Optics **27** (2), 217-221 (1988).

31. P. Kaye, E. Hirst, and Z. WangThomas, "Neural-network-based spatial light-scattering instrument for hazardous airborne fiber detection," Appl Optics **36** (24), 6149-6156 (1997).

32. P. Chylek, V. Ramaswamy, A. Ashkin et al., "Simultaneous determination of refractive-index and size of spherical dielectric particles from light-scattering data," Appl Optics **22** (15), 2302-2307 (1983).

33. A. K. Ray, A. Souyri, E. J. Davis et al., "Precision of light-scattering techniques for measuring optical-parameters of microspheres," Appl Optics **30** (27), 3974-3983 (1991).

34. T. R. Marshall, C. S. Parmenter, and M. Seaver, "Characterization of polymer latex aerosols by rapid measurement of 360 degree light-scattering patterns from individual particles," J Colloid Interf Sci **55** (3), 624-636 (1976).

35. Z. Ulanowski, Z. N. Wang, P. H. Kaye et al., "Application of neural networks to the inverse light scattering problem for spheres," Appl Optics **37** (18), 4027-4033 (1998).

36. P. H. Kaye, N. A. Eyles, I. K. Ludlow et al., "An instrument for the classification of airborne particles on the basis of size, shape, and count frequency," Atmos Environ a-Gen **25** (3-4), 645-654 (1991).

37. W. D. Dick, P. J. Ziemann, P. F. Huang et al., "Optical shape fraction measurements of submicrometre laboratory and atmospheric aerosols," Meas Sci Technol **9** (2), 183-196 (1998).

38. B. A. Sachweh, W. D. Dick, and P. H. Mcmurry, "Distinguishing between spherical and nonspherical particles by measuring the variability in azimuthal light-scattering," Aerosol Sci Tech **23** (3), 373-391 (1995).

39. S. Holler, Y. L. Pan, R. K. Chang et al., "Two-dimensional angular optical scattering for the characterization of airborne microparticles," Opt Lett **23** (18), 1489-1491 (1998).

40. Joseph W. Goodman, *Introduction to fourier optics*, 2nd ed. (McGraw-Hill, New York, 1996).

41. E. Hirst and P. H. Kaye, "Experimental and theoretical light scattering profiles from spherical and nonspherical particles," J Geophys Res-Atmos **101** (D14), 19231-19235 (1996).

42. R. G. Pinnick, S. C. Hill, Y. L. Pan et al., "Fluorescence spectra of atmospheric aerosol at adelphi, maryland, USA: Measurement and classification of single particles containing organic carbon," Atmos Environ **38** (11), 1657-1672 (2004).

43. J.R. Bottiger, P.J. Deluca, E.W. Stuebing et al., "An ink-jet aerosol generator," J Aerosol Sci **29** (suppl. 1), s965-s966 (1998).

44. E.R. Dufresne, Conversation based on unpublished work performed at Harvard University with D.A. Weitz. (2004).

45. T. T. Mercer, M. I. Tillery, and H. Y. Chow, "Operating characteristics of some compressed-air nebulizers," Am Ind Hyg Assoc J **29** (1), 66-& (1968).

46. R. N. Berglund and B. Y. H. Liu, "Generation of monodisperse aerosol standards," Environ Sci Technol **7** (2), 147-153 (1973).

47. M. J. Fulwyler, R. B. Glascock, R. D. Hiebert et al., "Device which separates minute particles according to electronically sensed volume," Rev Sci Instrum **40** (1), 42-& (1969).

48. K. R. May, "The collision nebulizer: Description, performance, and application," J Aerosol Sci **4** (3), 235-238 (1973).

49. S. Suchalkin, J. Bruno, R. Tober et al., "Experimental study of the optical gain and loss in inas/gainsb interband cascade lasers," Appl Phys Lett **83** (8), 1500-1502 (2003).

50. R. Q. Yang, J. L. Bradshaw, J. D. Bruno et al., "Room temperature type-ii interband cascade laser," Appl Phys Lett **81** (3), 397-399 (2002).

51. R. Kaspi, A. Ongstad, G. C. Dente et al., "High power and high brightness from an optically pumped inas/ingasb type-ii midinfrared laser with low confinement," Appl Phys Lett **81** (3), 406-408 (2002).

52. A.K. Goyal, G.W. Turner, M.J. Manfra et al., Proceedings of the IEEE Conference on Lasers and Electro-Optic Society (LEOS) Annual Meeting, (Piscataway, N.J, 2001).

53. M. Surbek, Masters Thesis, University of Applied Science, 2003.

54. K. B. Aptowicz, Y. L. Pan, R. K. Chang et al., "Two-dimensional angular optical scattering patterns of microdroplets in the mid infrared with strong and weak absorption," Opt Lett **29** (17), 1965-1967 (2004).

55. J. E. Bertie, M. K. Ahmed, and H. H. Eysel, "Infrared intensities of liquids .5. Optical and dielectric-constants, integrated-intensities, and dipole-moment derivatives of h2o and d2o at 22-degrees-c," J Phys Chem-Us **93** (6), 2210-2218 (1989).

56. J. J. Max and C. Chapados, "Isotope effects in liquid water by infrared spectroscopy," J Chem Phys **116** (11), 4626-4642 (2002).

57. C. M. Sorensen and D. Shi, "Patterns in the ripple structure of mie scattering," J Opt Soc Am A **19** (1), 122-125 (2002).

58. A. R. Jones, "Light scattering for particle characterization," Prog Energ Combust **25** (1), 1-53 (1999).

59. Rafael C. Gonzalez, Richard E. Woods, and Steven L. Eddins, *Digital image processing using matlab*. (Pearson Prentice Hall, Upper Saddle River, N. J., 2004).

60. Anil K. Jain, *Fundamentals of digital image processing*. (Prentice Hall, Englewood Cliffs, NJ, 1989).

61. Temperature data from supplied by the weather station as the Baltimore-Washington Internation Airport. Access to the data was provided by NOAA (National Oceanic and Atmospheric Administration) at www.noaa.org.

62. D. B. Kittelson, "Engines and nanoparticles: A review," J Aerosol Sci **29** (5-6), 575-588 (1998).

63. William H. Press, *Numerical recipes in fortran 90 the art of parallel scientific computing*, 2nd ed. (Cambridge University Press, 1996).